Haas et al. *Swiss Journal of Geosciences* (2022) 115:16
https://doi.org/10.1186/s00015-022-00407-y

SGG SGS sc | nat
Swiss Journal of Geosciences

ORIGINAL PAPER Open Access

Integrated stratigraphic, sedimentological and petrographical evaluation for CERN's Future Circular Collider subsurface infrastructure (Geneva Basin, Switzerland-France)

Maximilian Haas[1,2,3*], Davide Carraro[3], Dario Ventra[3], Michael Plötze[4], Antoine De Haller[3] and Andrea Moscariello[3]

Abstract

The European Organization for Nuclear Research (CERN) is currently undertaking a feasibility study to build the next-generation particle accelerator, named the Future Circular Collider (FCC), hosted in a 90–100 km subsurface infrastructure in the Geneva Basin, extending across western Switzerland and adjacent France. This article represents a preliminary, basin-scale stratigraphic and lithotype analysis using state-of-the-art Swiss and French stratigraphic terminology, set in context with the FCC. Existing stratigraphic information, rock cores and well reports, laboratory analyses and geophysical well-logs from 661 wells representative for the construction area have been integrated to pave the way for a multidisciplinary approach across several geoscientific and engineering domains to guide the FCC's upcoming technical design phase. Comparisons with well-log data allowed the identification of rock formations and lithotypes, as well as to formulate a preliminary assessment of potential geological hazards. Regional stratigraphic evaluation revealed the FCC's intersection of 13 geological formations comprising 25 different lithotypes across the Geneva Basin. A lack of data remains for the western to south-western subsurface region of the FCC construction area shown by well-density coverage modelling. The main geological hazards are represented by karstic intervals in the Grand Essert Formation's Neuchâtel Member, Vallorbe and Vuache formations, associated to fractured limestone lithotypes, and Cenozoic formations represented by the pure to clayey sandstone-bearing Transition zone and Siderolithic Formation. Potential swelling hazard is associated to the presence of anhydrite, and claystone lithotypes of the Molasse Rouge and Grès et Marnes Gris à gypse formations, yielding up to 17.2% of smectite in the Molasse Rouge formation. Hydrocarbon indices in both gaseous and bituminous forms are encountered in the majority of investigated wells, and bear a potential environmental hazard associated with the Molasse Rouge deposits and fractured limestones of the Mesozoic Jura formations.

Keywords: Lithotypes, Geophysical well-logs, Laboratory analyses, Field data, Tunnelling, Swelling, Karst, Future Circular Collider (FCC), CERN, Molasse, Siderolithic, Cretaceous, Geneva Basin

1 Introduction

The construction of subsurface infrastructure has gained increasing public attention, as manifested by the Gotthard, Lötschberg and Brenner Base tunnels, following extensive geological investigations prior to construction approval (Burdin et al., 2017; Ehrbar, 2008; Fachgruppe für Untertagebau (FGU), 2016; Haas et al., 2021;

Editorial handling: Wilfried Winkler

*Correspondence: maximilian.mathias.haas@cern.ch
[1] European Organization for Nuclear Research (CERN), Espl. Des Particules 1, 1211 Geneva, Switzerland
Full list of author information is available at the end of the article

Thalmann, 1996; Voit, 2013; Voit et al., 2015; Ziegler & Isler, 2013) and environmental impact assessment studies (e.g. Haas et al. 2020a, b). Despite their purpose being commonly aimed at transport infrastructure, tunnelling constitutes an essential part of construction operations for large underground laboratories. Extensive subsurface tunnel excavations have been part of engineering solutions for the Large Electron Positron (LEP) particle collider built in 1988 for the European Organization of Nuclear Research (CERN) across the Swiss and French border close to the city of Geneva (Switzerland) as well as for its successor, the Large Hadron Collider (LHC). The LHC used LEP's existing subsurface infrastructure and extended it by the construction of *A Toroidal LHC ApparatuS (ATLAS)* and *Compact Muon Solenoid (CMS)* particle detector caverns for first particle collisions in 2008. Simultaneous stipulations agreed on an upgrade of the LHC, named the High-Luminosity Large Hadron Collider (HL-LHC), adding larger caverns and extending tunnel galleries to the existing ca. 27 km LHC subsurface infrastructure, to be scheduled for first physics experiments in 2027 (Voiron et al., 2020).

For high-energy particle collision experiments, CERN initiated a feasibility study in 2013 aiming at a next-generation particle accelerator, the Future Circular Collider (FCC), to be hosted in a new 90–100 km-long, quasi-circular subsurface infrastructure within the Geneva Basin, starting construction after 2030. An essential part of the FCC's current feasibility phase is a thorough understanding of the subsurface conditions for tunnelling construction, usage and disposal of an estimated ca. 10 million m^3 of excavated regolith, rock and soil, and the assessment of geological and environmental hazards (Haas et al., 2020a, b; Haas et al., 2021). In its current construction layout across the Swiss-French geographical area defined herein as the Geneva Basin (GB), about 90% of the FCC's encountered rock is estimated to be represented by interstratified sandstone, marlstone, and conglomerate attributed to the Oligocene Molasse Rouge and Grès et Marnes Gris à gypse formations, 6% by Mesozoic limestone formations of the Jura and marly freshwater limestone as part of the Molasse Rouge formation, and 4% by unconsolidated morainal debris of Quaternary age. In this study the term Geneva Basin is used in a geographical context (Moscariello, 2019), emphasizing the region around the city of Geneva as part of the western Swiss Molasse Basin and its surrounding French departments Ain and Haute-Savoie.

During the past decades, the GB has been the subject of vast geological research with a strong focus on hydrocarbon exploration from the 1970's to the 1990's (Bachmann et al., 1982; Lemcke, 1967), as potentially economic reservoirs were identified in the Austrian and German Molasse basins as part of the Northern Alpine Foreland Basin (NAFB) (Bartenstein, 1978; Berger, 1996; Brink et al., 1992; Doppler, 1989; Gross et al., 2018; Gusterhuber et al., 2014; Sachsenhofer et al., 2010; Schulz et al., 2002; Wehner et al., 1983; Ziegler, 1990). This early phase of applied research was followed by renewed interest for groundwater resources (Keller, 1992) and hydrocarbon distribution (Do Couto et al., 2021). Much predictive and interpretive research on the regional geology and stratigraphy has been guided by concepts linking the evolution of orogenic processes to foreland-basin stratigraphic and depositional evolution (Sinclair & Allen, 1992; Sinclair et al., 1991). During the past decade, research has concentrated on the potential importance of carbonate formations for geothermal exploration and subsurface heat storage (Chelle-Michou et al., 2017; Clerc et al., 2015; Makhloufi et al., 2018; Moscariello, 2018, 2019; Moscariello et al., 2020; Rusillon, 2018). Based on these extensive scientific and industrial explorations, available well-log and rock core datasets from adjacent basins have been accumulated to decipher the stratigraphic evolution, phases of basin uplift and erosion (Amir et al., 2020; Brink et al., 1992; Kaelin et al., 1992).

Despite a recent classification into six geotechnical classes (sandstones and marls) based on rock mechanics tests on Molasse Rouge samples taken during CERN's HL-LHC's construction (Fern et al., 2018), a distinct lack of stratigraphic analyses and lithotype identification remains for depths ranging from 0 to 1′000 m above sea level (m ASL) in the GB's subsurface, compared to the knowledge amassed on corresponding sectors of the NAFB in Austria, Germany, eastern Switzerland and eastern France (e.g. Amir et al., 2020). This lack of high-resolution information on stratigraphy and lithotypes for the GB's formations greatly hampers subsurface prediction for applied purposes, such as the FCC construction.

In particular, geo-engineering hazards such as swelling rocks, karstic intervals, aquifer horizons and presence of hydrocarbons considering environmental impact, and active fault regimes have remained undeciphered for the GB. Swelling depicts a significant hazard when tunnelling in clay-rich sedimentary deposits (Anagnostou, 1993; Anagnostou et al., 2010; Einfalt et al., 1979; Einstein, 1996; Kovári et al., 1987) and has led to severe problems at tunnel construction sites worldwide, e.g. in the Jura of Switzerland and France, southern Germany, Spain, Poland, Italy and the U.S.A. (Alonso & Olivella, 2008; Berdugo et al., 2009; Kovári et al., 2002; Steiner, 1993; Vrakas & Anagnostou, 2016; Yilmaz, 2001). Another type of geological hazard is posed by karstic features that have caused water flooding at several subsurface construction sites (Alija et al., 2013; Li et al., 2020; Lv et al., 2020; Su et al., 2021), while aquifer tables and associated groundwater flow (Butscher et al., 2011; Hasegawa et al., 1993)

have been well integrated in required environmental impact assessment studies (Huang et al., 2015) and contemplate together with seismic activity (Rehbock-Sander & Jesel, 2018) distinct hazards for subsurface construction projects.

This article aims to provide a detailed evaluation of the shallow subsurface across the Geneva Basin (Fig. 1) by reviewing existing stratigraphic and geophysical well-log data from former research and industrial activities preceded by their digitization and associated sedimentological and petrographical descriptions of lithotypes by means of inspected core material. This yet unpublished data are further integrated with performed mineralogical, geochemical and petrophysical laboratory analyses in order to (1) infer potential geological hazards, (2) establish a robust predictive approach addressing engineering uncertainties, and (3) optimize well placement prior to site investigations within the scope of the FCC's transition into the subsequent technical design phase in the upcoming years.

2 Geological setting

The western part of the Northern Alpine Foreland Basin (NAFB) has been thoroughly investigated along country borders, which makes it common to use different geographical terms in the literature, such as the *Bassin Franco-Genevois* or *Savoy Molasse Bassin* (Deville et al., 1994) in French-speaking countries when referring to the westernmost Swiss Molasse Basin (SMB) and to the adjacent French Molasse Basin (FMB). This article uses the term Geneva Basin (GB) (Moscariello, 2019) to emphasise the geographical area as part of both the SMB and FMB, and is bordered by the Jura mountains in the north/northwest, the Prealps in the east, the Salève massif in the south and the Vuache Fault system in the south/southwest. Stratigraphically, the Geneva Basin covers the Molasse and Quaternary deposits of the SMB and FMB, as well as the sediments of the Jura, and is delimited by the latter and by the Helvetic and Penninic units.

The following sections first derive the tectonic evolution of the NAFB and the Mesozoic deposits of the Jura, followed by a stratigraphic description related to the GB marking the essential geological formations intersected by the FCC. A profound understanding of the spatial distribution of Mesozoic, Molasse and Quaternary deposits and of the temporal succession of depositional paleoenvironments are crucial for subsurface geo-engineering prospection in view of the construction of the FCC. This allows a reasonable extrapolation of the lithostratigraphic and lithological/-technical information (lithotypes) from available wells to nearby areas that have not yet been investigated directly in the subsurface.

2.1 Tectonic evolution of the Northern Alpine Foreland Basin (NAFB)

The NAFB is located north of the Alps and extends approximately from Lake Geneva (Lac Léman) in western Switzerland, across Bavaria in southern Germany, to the east towards Vienna in Austria, reaching up to 700 km in lateral extent for its Oligocene–Miocene infill (Kempf & Pross, 2005). The NAFB evolved from a foredeep to a negative-alpha basin controlled by rollback mechanisms of a proposed European slab (Schlunegger & Kissling, 2015) during the Paleogene and Neogene due to flexural bending of the European Plate under increasing orogenic load by the advancing Alpine thrust wedge (Allen et al., 1991; Burkhard & Sommaruga, 1998; Homewood et al., 1986; Karner & Watts, 1983; Pfiffner, 1986, 2021). The term "negative-alpha" describes a basin that formed on top of an orogenic wedge (Fuller et al., 2006; Willett & Schlunegger, 2010). The NAFB's tectonic origin relates to crustal loading in proximity of the uplifting Alpine orogen (Mock & Herwegh, 2017; Schlunegger & Mosar, 2011). The basin and the associated orogenic belt show different tectonic patterns along their east–west extent, distinguishing Swiss, southern German and Austrian sectors (Willett & Schlunegger, 2010). Sommaruga et al. (2012) described a notable decrease in structural complexity expressed in Mesozoic lithologies from west to east along the NAFB, substantiated by different deformation styles. In the western, wedge-top part

(See figure on next page.)

Fig. 1 **A** Overview of tectonic realms in the Geneva Basin for the FCC construction with analysed well and outcrop locations. Geophysical well-logs were digitized and analysed together with available rock core data from these wells. See Table 1 for well numbers and full well-IDs. The overlying Quaternary deposits are neglected for increased readability. The blue line depicts cross section A, the green line refers to cross section B (Figs. 5, 6). Note that the Salève and Mandallaz limestone as commonly referred to in technical reports are part of the Jura. *FTB* fold-and-thrust belt. **B** The white profile X–Y displays a large-scale cross section through the Geneva Basin and is based on chronostratigraphic units representing the vertical and spatial relationships of age-defined packages of lithologies in a geo-historical picture. The FCC's current subsurface tunnel alignment is currently foreseen at a depth interval between 100 to 300 m ASL. The Burdigalian Molasse belongs to the Upper Marine Molasse and is hereby noted Marine Molasse. Data compiled, amended and modified after Bachmann & Müller, 1991; Charollais et al., 2013; Clerc & Moscariello, 2020; Deville et al., 1994; Haq et al., 1987; Kuhlemann & Kempf, 2002; Lemcke, 1988; Mastrangelo & Charollais, 2018; Moscariello, 2019, 2021; Zweigel et al., 1998

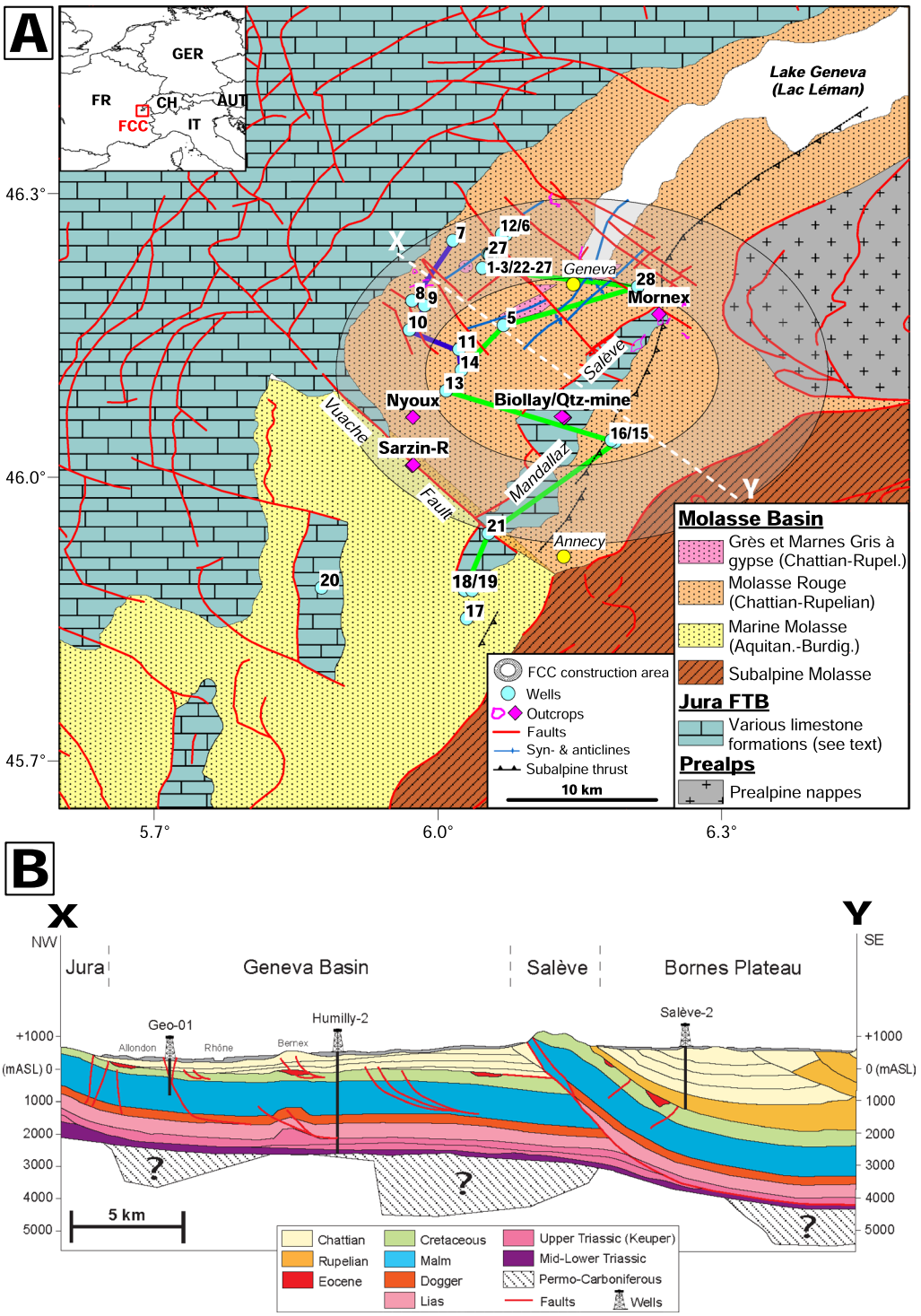

Fig. 1 (See legend on previous page.)

of the basin, thrusting and long-wavelength, evaporite-cored detachment folds relate to thin-skinned detachment tectonics (Sommaruga, 1999, 2011; Sommaruga et al., 2012), whereas the eastern, non-detached part is comprised of normal faults related to Jurassic extension and subsidence of the epicontinental European shelf (Sommaruga et al., 2012; Stauble & Pfiffner, 1991; Wetzel et al., 2003). The *Fernschub* hypothesis,

originally proposed by Buxtorf (1916), confirmed a detachment of foreland sediments along a Triassic evaporite unit (Laubscher, 1961), leaving the SMB as the NAFB's westernmost area relatively undeformed compared with its conjugate eastern German and Austrian equivalents. Predominant conjugate NNE-SSW and NW–SE-trending strike-slip fault zones cut the western SMB and extend into the Jura fold-and-thrust belt (FTB), e.g. Vuache Fault (Fig. 1) (Gorin et al., 2003; Ibele, 2011; Sommaruga, 1999), limited to the sedimentary cover (Courboulex et al., 1999; Thouvenot et al., 1998). Therefore, the Alpine orogen forms a tapered, double-vergent wedge to the NNW and SSE, with both the Jura FTB and SMB being decoupled from the basement over a basal *décollement* (Mosar, 1999). The Vuache and Dent de Vaulion Fault systems extend from the SMB into the Jura and are conjugate with SE-NW-striking dextral faults (Burkhard, 1990; Burkhard & Sommaruga, 1998; Sommaruga, 1997, 1999, 2011; Sommaruga et al., 2017). The Mesozoic deposits of the Jura form the substrate of the Cenozoic NAFB, which lies passively on top (cross-section X–Y in Fig. 1). Today both the Mesozoic and the Cenozoic deposits structurally form a single tectonic unit. From a tectonic point of view, there are two major structural units in the impacted FCC construction area: the Mesozoic of the Jura plus the Cenozoic (Molasse) of the Geneva Basin in the northwest, and the thrusted Mesozoic of the Salève plus the Cenozoic (Molasse) of the Bornes Plateau in the southeast. The geographical GB is tectonically delimited by the Jura and the Mesozoic sedimentary Helvetic and Penninic units, and is internally divided into two tectonic subunits, the Plateau Molasse and the Subalpine Molasse, respectively (Burkhard, 1990; Mock & Herwegh, 2017; Pfiffner, 1986). The slightly deformed Plateau Molasse is up to 50 km wide and is affected by faults and folds (Gorin et al., 2003), with exemptions towards the west suggesting a convergence of Alpine and Jura structures (Burkhard, 1990). This required progressive sedimentation within the basin to guarantee mechanical integrity (Fuller et al., 2006). Thrusting of the Subalpine Molasse started in the Oligocene (Schlunegger et al., 1997) and lasted until approximately 5 Ma (Von Hagke et al., 2012). After an early deformation phase in the Late Oligocene (Kempf & Pross, 2005; Kuhlemann & Kempf, 2002), principal tectonic shortening occurred in the Jura FTB between 12 and 4 Ma (Becker, 2000), followed by progressive minor deformation in Pliocene–Quaternary times (Madritsch et al., 2010).

Two predominant hypotheses persist on the creation of accommodation for Molasse deposits: the first one is the argument of sea-level changes impacting sediment supply, reflected by the two mega-sequences of marine to terrestrial deposits (Bachmann & Müller, 1991, 1992; Lemcke, 1984); the second one attributes the main role to tectonics and Alpine uplift in driving sediment accumulation, whereby the establishment of terrestrial environments would have followed increased sediment supply from the orogen, and marine conditions would have been tied to lesser sediment influx (Kuhlemann, 2000; Oxburgh, 1981; Schlunegger & Hinderer, 2001; Schlunegger et al., 2001). Both hypotheses hinge on sediment supply as proximate control on patterns of deposition (Kuhlemann & Kempf, 2002; Schlunegger & Mosar, 2011). For the Central Alps, a third hypothesis favours a slab-rollback mechanism to explain foreland plate flexure and accommodation space creation (Schlunegger & Kissling, 2015), substantiated by a delayed rebound-type, erosional response to surface uplift, and represented by larger sediment fluxes and shifts to more proximal facies (Schlunegger & Castelltort, 2016). Large sediment influx could have controlled the establishment of (fluvial) fans. These fans further prograded over several tens of kilometres, merging distally with an axial fluvial system, which linked the Tethys to the Black Sea (Kuhlemann & Kempf, 2002; Sinclair et al., 1991).

Early post-collisional Alpine history was characterized by increased sedimentation rates at the Rupelian/Chattian transition, attributed to isostatic readjustment (Kuhlemann et al., 2002). Further increases in sedimentation rate took place later during the Aquitanian (23–21 Ma) and late Burdigalian (ca. 18–16.4 Ma), followed by decreased rates in early to middle Burdigalian (21–19 Ma) and Langhian to Serravalian times (16.4–12 Ma) (Kuhlemann et al., 2002). While the swift increase in sediment discharge in the Eastern Alps is explained by the termination of E-W extension (Dunkl & Demény, 1997) and subsequent minor uplift recorded by a regional regression (Winkler-Hermaden, 1958), the Western Alps record a rather slower reduction (Kuhlemann et al., 2002) due to extensional tectonics (Pfiffner, 1986; Schlunegger, 1999; Schmid et al., 1996). Basin inversion of the SMB between 11 and 10 Ma (Kaelin, 1997) changed the drainage pattern to an easterly direction and was intensified by folding and thrusting of the Swiss Jura Mountains (Kuhlemann et al., 2002). Still ongoing basin uplift started in latest Miocene times in the Swiss and Western Alps (Kuhlemann et al., 2002).

2.2 Stratigraphic framework of the Swiss Molasse Basin

The Jura and the Swiss Molasse Basin (SMB) consist of folded Mesozoic and Cenozoic successions, which are detached from the pre-Triassic basement (Sommaruga,

1997). During the Mesozoic, the Jura and the western SMB were part of the Alpine Tethys passive margin and comprised approximately 2 km of alternating limestone and marl (Sommaruga et al., 2012). Oligocene and Miocene alternating fluvial, lacustrine and marine Molasse sediments onlap the underlying Mesozoic rocks towards the northwest (Sommaruga, 1997, 1999; Sommaruga et al., 2012). For the present study and the GB's geographical realm, the Jura's subdivision into the external and internal Jura domains plays an important role, while the third subdivision as the Tabular Jura is significant for the realms only around the southern Black Forest and Vosges basement. With the external Jura consisting of flat areas and plateaus delimited to the north, the internal Jura, also referred to as folded Jura or *Haute Chaîne*, represents thrust-related folds and sinistral faults, whose orientation gradually changes from a N-S in the eastern Jura to a WNW-ESE direction in the western Jura (Sommaruga, 1997, 1999). The Mesozoic formations describe the general evolution from a shallow, peritidal platform to deep-water shelf environments followed by the evolution of a carbonate platform, and its subsequent drowning in order to prevail in pelagic conditions (Sommaruga, 1997; Strasser et al., 2016). Lower Cretaceous units, formerly termed *Urgonien*, are dominated by carbonate sedimentation, and marked by increasing clastic input associated to Valanginian sea-level fall (Haq, 2014). Variations of relative sea-level of both tectonic and eustatic origin drastically controlled the development of depositional environments. The common lateral and vertical changes in facies and sedimentation rates as well as numerous hiatuses within the formations witness a complex interplay of tectonics, climate, and sea level that controlled the Jura during the Cretaceous (Strasser et al., 2016). One of these hiatuses reflects 72 My separating rocks of Aptian age in the GB (Brentini, 2018; Rusillon, 2018) from the overlying Siderolithic Formation of proposed Late Eocene age (Charollais et al., 2007). This hiatus resulted probably from subaerial exposure and consequent development of an erosive and deep karst system at the top of the Mesozoic series, which play a predominant role in the aquifer drainage systems of the Cretaceous and Jurassic limestone across the GB (Moscariello, 2018), as well as for 6% of the FCC's current subsurface perimeter.

The infill of the SMB comprises two regressive, coarsening-upward sedimentary mega-sequences, each marking a transition from marine to continental conditions (Matter, 1980; Sinclair & Allen, 1992; Sinclair et al., 1991). The two mega-sequences are composed of four predominant lithostratigraphic units (Matter et al., 1980; Lemcke, 1988), namely the Lower Marine Molasse (LMM), the Lower Freshwater Molasse (LFM), the Upper Marine Molasse (UMM) and the Upper Freshwater Molasse (UFM). Informal terms often used in a regional context of the LFM also refer to the *Molasse Rouge* and *Marnes bariolées* as well as the *Grès et Marnes Gris à gypse*, whereas the latter shows an increased content of gypsum (Haas et al., 2020a). For the northern/northeastern SMB, Freshwater-Brackish Molasse (SBM) evolved between the UMM and UFM (Bachmann & Müller, 1992; Lemcke et al., 1953). The eastern German and Austrian Molasse basins were subjected to marine conditions until Burdigalian times (Lemcke, 1984), which makes the LFM terminology for terrestrial deposits only reasonable for the SMB and western Bavaria due to prevailing marine conditions to the east (Kuhlemann & Kempf, 2002). The total sedimentary cover in the western SMB consists of up to 5′000 m of Mesozoic and Cenozoic successions overlying the basin's crystalline basement (Clerc & Moscariello, 2020; Gorin et al., 1993). Molasse deposition started in the Rupelian (34–30 Ma) as LMM and Chattian to Aquitanian (30 – 20 Ma) as LFM, respectively (Strunck & Matter, 2002), marking the transition from an underfilled to an overfilled foreland basin (Erdős et al., 2019; Sinclair & Allen, 1992). A Burdigalian (20 – 17 Ma) transgression that established the "Burdigalian Seaway", was probably caused by reduced sediment discharge (Kuhlemann & Kempf, 2002) and marked the start of the second mega-sequence, with accumulation of the UMM (Keller, 1989, 1992) under marine conditions onto a truncated surface of LFM (Allen et al., 1991; Herb, 1988; Kempf & Pross, 2005; Matter, 1980; Sinclair & Allen, 1992). Molasse deposition in the Langhian to Serravallian (< 17 Ma) accumulated fluvial floodplain and braidplain to lacustrine siliciclastics of the UFM in an overfilled basin, terminating marine conditions (Diem, 1986; Sinclair & Allen, 1992). Fluvial deposits of large alluvial megafans not only in the western SMB, but particularly in the central/eastern SMB were formed during the overfilled stage (Frisch et al., 1998; Kaelin & Kempf, 2009; Ortner et al., 2015; Schlunegger & Castelltort, 2016) despite decreasing sediment discharge until 11 Ma (Kuhlemann & Kempf, 2002). After 11 Ma, sedimentation terminated in the western part of the NAFB due to folding and uplift of the Swiss Jura (Kuhlemann & Kempf, 2002). The Freshwater units (LFM and UFM) were accumulated in terrestrial settings, consisting mainly of alluvial and fluvial-fan deposits along the southern basin margin and fluvio-lacustrine sediments in the central and external parts of the SMB (Kempf & Pross, 2005). Kilometre-thick conglomerate successions were deposited by alluvial fans at the basin margin, while sand- and mud-dominated successions extended farther basinward (Kempf & Matter, 1999; Schlunegger et al., 1997; Spiegel et al., 2001). Marine units are predominantly composed

of shallow-marine siliciclastics deposited in tide- and storm-influenced environments (Kempf & Pross, 2005). To the east, the SMB persisted in an underfilled stage until at least 17 Ma, when sedimentation of sandstone and marlstone occurred under brackish to shallow-marine conditions (Hinsch, 2013; Lemcke et al., 1953; Mock et al., 2020). Alluvial fans were missing in the eastern part of the NAFB due to the paleo-Inn river transporting clastic debris further to the east (Frisch et al., 1998; Kuhlemann & Kempf, 2002). During UFM deposition, sediments originated from the central Alps and from massifs adjoining to the basin (Füchtbauer, 1959). Molasse and Quaternary deposits accumulated on top of 2 km of Lower Triassic to Upper Cretaceous shallow-marine sediments, which are not outcropping in the eastern SMB (Charollais et al., 2007, 2013; Sommaruga, 1997; Sommaruga et al., 2012).

The identification of the four Molasse lithostratigraphic units was based on biostratigraphic, magnetostratigraphic and palynostratigraphic data that constrained the marine to terrestrial transition (LMM to LFM) to about 31 Ma for the Wilhelmine Alpes section in the German Molasse Basin (Kempf & Pross, 2005). Magnetostratigraphically correlated sections from central and eastern Switzerland indicate a diachronous regression of the LMM between 31.5 and 30 Ma during the LMM, associated with enhanced clastic input from the rising Alps (Kempf & Pross, 2005). Biostratigraphic information confirms a Chattian age for the equivalent LMM-LFM transition in the German Molasse Basin (Reichenbacher et al., 2004; Uhlig et al., 2000). Magnetostratigraphic data of the LFM-UFM resulted in a calibration chart for the NAFB within a timeframe of 28–13 Ma (Kempf & Matter, 1999; Kempf et al., 1997; Schlunegger et al., 1996; Strunck & Matter, 2002).

A drastic base-level drop (Brenchley, 1992; Lemcke, 1988) of possible eustatic origin occurred around 28.5 Ma (Abreu & Anderson, 1998; Haq et al., 1987) and caused an LMM regression towards the east (Bachmann & Müller, 1992; Lemcke, 1988; Zweigel et al., 1998). The LMM and lowermost LFM lithostratigraphic successions define a shallowing trend towards the top, indicated by an increase in sediment grain size (Diem, 1986). The LMM-LFM transition in the western SMB is part of the Subalpine Molasse, documenting conditions at the southern basin margin (Kempf & Pross, 2005). The study by Kempf and Pross (2005) emphasised the role of sediment supply for the transition of marine to terrestrial sedimentation in the northern Alpine foreland. In contrast to its eastern continuation, the western SMB lacks UFM units, which suggests complete erosion of this lithostratigraphic unit. Several researchers derived erosion thickness maps for the Late Miocene and post-Miocene times using apatite fission tracks, vitrinite reflectance, shale compaction and porosity measurements (Kaelin et al., 1992; Mazurek et al., 2006; Schegg, 1993); Cederbom et al. (2004) proposed erosion up to 1,500 m for the Swiss Molasse Plateau and 3′000 m for the Subalpine Molasse as part of the SMB. They further mark the onset of erosion at 5 Ma, shortly before tectonic basin inversion.

In the GB, the Cenozoic succession consists explicitly of Oligocene to Early Miocene LFM deposits. The overlying UMM is found in the adjacent Bellegarde and Rumilly basins to the west and southwest of the Vuache Fault (Amir et al., 2020; Charollais et al., 2007; Paolacci, 2012). At the Bornes Plateau, the thrusted Subalpine Molasse is encountered at the front of the Subalpine units (Charollais et al., 2007; Paolacci, 2012) continuing in front of the Prealpine units into the Lake Geneva encountering lacustrine sediments as inferred from seismic data (Dupuis, 2009). Accumulation of Molasse sediments took place during Jura deformation and in Late Miocene as the basin was detached from its basement (Cederbom et al., 2008). This suggests that erosion did not start before Pliocene times (Cederbom et al., 2004), but was associated to the 10–4 Ma Jura FTB shortening phase (Ziegler & Fraefel, 2009). These Molasse deposits are composed of sandstone, marl and intercalations of anhydrite/gypsum and conglomerates (Wildi et al., 2017) tied to erosion of the Western Alps (Oxburgh, 1981), sea-level changes (Bachmann & Müller, 1992) or possibly a combination of both (Schlunegger & Mosar, 2011). They constitute more than 90% of the subsurface domain to be intersected by the FCC's current layout.

Glacial erosion and deposition shaped the central part of the GB during the Middle and Late Pleistocene (Arn, 1984). Associated Quaternary deposits comprise the GB's cover as intersected by about 4% of the current FCC subsurface layout. A recent revision of the old nomenclature for Switzerland's glacial periods (*Günz*, *Mindel*, *Riss*, *Würm*) introduced the terms post-glacial and interglacial deposits with a new stratigraphic classification taking into account not only lithological but also geomorphological features of these deposits (Graf & Burkhalter, 2016). A distinct geomorphological element in the GB depicts the *Petit Lac* at the southwestern termination representing the remains of a subglacial tunnel valley, which formed underneath the Rhone Glacier by subglacial meltwater (Fiore, 2007; Moscariello, 1996; Moscariello et al., 1998; Van der Vegt et al., 2012). Borehole data gave hints that the Rhone Glacier was responsible for incising and removing older Quaternary sediments reaching the underlying Molasse deposits during the Last Glacial Maximum (LGM). In the subsurface, this incision deviates towards the SE. On

the surface, the buried incision is observed by the narrow Aire valley reflecting a branch of the Arve River located SE of the elongated Molasse ridge (*Bernex*). It is assumed that the Rhone Glacier tunnel valley was gradually filled by a thick succession of proglacial lake deposits (Moscariello, 1996) and accumulated in the large lake formed at the front of the melting LGM glacier (Moscariello, 2018). The downstream segment was filled with a mixed succession of subglacial, lacustrine, and proglacial deposits generated by the Arve Glacier (Moscariello, 2018). Low-relief ridges, perpendicular to the main valley axis represent the subaqueous frontal moraines formed during temporary re-advances of the glacier during the glacial withdrawal phase. Large, flat-bottomed incision bordering the Soral–Laconnex subaqueous moraine resulted from meltwater discharge generated by the Arve Glacier, which carved a narrow spillway between the glacier and the northern slope, and merged with the proglacial/lacustrine deposits that formed the flat morphology of the SW part of the Geneva area. The natural separation between the buried tunnel valley and its partly filled portion (*Petit Lac*) depicts a narrow ridge today. To the SE, this ridge forms an apron dipping to the SW, interpreted as a frontal moraine related to the Rhone Glacier, most likely formed in subaqueous(?) and subglacial(?) conditions (Moscariello, 1996, 2018). The proglacial and paraglacial lake caused by the melting of the Rhone, Arve, and Jura glaciers gradually reduced its volume, which is represented in the terraced surfaces on both sides of the Lake Geneva (Burri, 1981). These kame terraces formed in ephemeral lakes related to the LGM glacier at the ice front (Donzeau et al., 1997) in correspondence with probably lateral tributaries or supraglacial stream mouths (Moscariello et al., 1998). Lacustrine terraces formed during the evolution of syn- and postglacial lake levels after the disappearance of the Rhone Glacier, ultimately charging the sinuous Rhone River that incised cemented gravel deposits, which are locally known as the *Alluvion Ancienne*. Progressive incision of both the Rhone and Arve rivers shaped the central GB by various slopes of glacial origin towards the main axial drainage system represented by the *Petit Lac*. The Allondon River is likely associated with karst and fractured networks, whereby its associated deposits are the subject of current research.

3 Materials and methods

3.1 Review of existing boreholes and database setup

Boreholes were reviewed across the Geneva Basin and selected within a 2 km range outside the FCC's planned quasi-circular perimeter (Abada et al., 2019; Benedikt et al., 2020). Geology not covered by the FCC's current footprint but likely to be encountered inside the FCC construction ring was accounted in case available reported wells contained useful stratigraphic or geophysical well-log data. Over 2′000 boreholes were drilled in the Geneva Basin by Swiss (e.g. *Services Industriels de Genève, SIG*) and French (e.g. *Bureau de Recherches Géologiques et Minières, BRGM*) state surveys, as well as various oil and gas companies for geothermal, hydrocarbon and hydrogeological exploration. Among all well reports and datasets available from BRGM's online Infoterre database, Swisstopo's subsurface database, the literature, industrial exploration, and drilling campaigns (Brentini, 2018; Chablais & Rusillon, 2018; Chablais & Savoy, 2019; Clerc et al., 2015; Doumer and British Petrol (France), 1983f; Doumer and (France), 1983; Doumer and British Petrol (France), 1983b, 1983d, 1983a, 1983e, 1983c; Etat de Genève, 1994; Gervaise, 1972; Géotechnique Appliquée Dériaz & SA (GADZ), 1981a, 1981b, 1982b, 1982a, 1992, 1993a, 1993b, 1996a, 1996b, 1997, 2015a, 2015b, 2015c, 2015d, 2016a, 2016b, 2016c; Jenny et al., 1995; Lanterno et al., 1981; Pierdona, 2018; Rusillon, 2018; Schegg, 1993; Services Industriels de Genève (SIG), 2019; Wegmüller et al., 1995), 661 wells have been presently considered useful for the FCC's subsurface layout. Digitisation of ca. 37 km of cumulative geophysical well-log curves was performed on 28 selected boreholes (Fig. 1, Table 1), which comprised geophysical well-log data, rock core samples and both sedimentological and petrographical descriptions from well reports. Well-log data was further correlated to available core material by analyses on cuttings and plugs, the latter drilled from full-cores, half-cores and samples collected from outcrops. Core sample measurements were extrapolated from nearby wells to the Geo-01 well at similar depth levels for consecutive petrophysical well-log calculations.

The full datasets of reviewed and digitised well reports as well as laboratory results were stored in a dedicated database created in Microsoft ACCESS referencing each sample and well geospatially (longitude, latitude, elevation, depth) in non-projected coordinate system (World Geodetic System 1984). The database contains metadata of well-ID, drilling purpose, measured and true vertical depth, available third-party samples and samples taken within the scope of this study, as well as performed laboratory analyses. Furthermore, associated digitized stratigraphic data such as chronostratigraphic range (era, period, series/epoch, stage/age), top and bottom depth of encountered geological formations, lithostratigraphy, geological hazards (karstic intervals, hydrocarbon indices, swelling rocks), rock type and rock type description from logs as well as an appositely devised unified terminology to homogenize different (old) stratigraphic terms spanning over the past 70 years were added into the database.

Table 1 List of boreholes containing digitized and analysed geophysical well-logs used for petrophysical calculations and lithotype correlations

Map-ID (Fig. 1)	Well-ID	Measured depth (m)	Longitude (WGS 1984)	Latitude (WGS 1984)	Digitized well-logs	Cumulative length of digitized logs (m)	Year of drilling	Drilling purpose	Sample type
1	C1	90.70	6.05307890	46.23646280	CALI, GR, Vp, Vs	336.00	2015	SI	Plugs
2	C2	81.50	6.05455910	46.23617420	CALI, GR, Vp, Vs	167.00	2015	SI	Plugs
3	C3	81.70	6.05745850	46.23575360	CALI, GR, Vp, Vs	156.00	2015	SI	Plugs
4	Geo-01*	744.06	6.04687090	46.22162423	CALI, GR, URAN, THOR, POTA, SP, DT, RHOB, RHOMAA, DRHO, NPHI, RS, RD, PEF	-	2018	GX	Cuttings****
5	Geo-02*	1130.00	6.06917612	46.16099600	CALI, GR, URAN, THOR, POTA, SP, RHOB, DRHO, NPHI, RS, RD, PEF	-	2020	GX	Cuttings****
6	Gex-CD-01	290.5	6.07202053	46.25699268	CALI, GR, SP, DT, RHOB, ILD, NPHI	1358.00	1983	E&P	Cuttings, plugs
7	Gex-CD-02	403.20	6.01576270	46.25072090	DT	341.00	1983	E&P	Cuttings, plugs
8	Gex-CD-03	294.00	5.97257804	46.18706358	CALI, GR, SP, DT, SFL	1465.00	1982	E&P	Cuttings, plugs
9	Gex-CD-04	291.70	5.98583792	46.18190859	CALI, GR, SP, DT, SFL	1458.00	1982	E&P	Cuttings, plugs
10	Gex-CD-05	560.00	5.96985080	46.15607813	no logs	-		E&P	Cuttings, plugs
11	Gex-CD-06	422.00	6.02225030	46.13546971	CALI, GR, SP, SN, LN, NPHI	892.00	1983	E&P	Cuttings, plugs
12	Gex-CD-07	256.00	6.06751781	46.25758598	CALI, GR, SP, MSFL, LLS, LLD	1412.04	1983	E&P	Cuttings, plugs
13	Humilly-1	905.00	6.00864530	46.09165386	CALI, SP, Vp, SN	3481.00	1960	E&P	–
14	Humilly-2*,**	3051.00	6.02487400	46.11363102	CALI, GR, DT, RHOB, DRHO, LLD, NPHI	-	1969	E&P	Cuttings****
15	Salève-1	1175.60	6.18749460	46.03768763	SP	970.00	1959	E&P	–
16	Savève-2	1985.80	6.18334960	46.03921755	SP	815.00	1959	E&P	–
17	Savoie-101	2064.00	6.03042100	45.85043460	GR, SP, SN, LN, LAT, LIM	6000.00	1952	E&P	–
18	Savoie-104	1903.00	6.02818960	45.88050040	CALI, SP, SN, LN	4405.00	1953	E&P	–
19	Savoie-105	690.70	6.03605080	45.88042220	SP, SN, LN, INV	2280.00	1953	E&P	–
20	Savoie-107	2116.00	5.87683480	45.88302440	GR, SP, SN, LN	6000.00	1954	E&P	–
21	Savoie-109	1260.90	6.05337210	45.94061902	SP, SN, LN	3252.00	1959	E&P	–
22	SLHC20	120.20	6.05507350	46.23585973	GR, DT, RHOB, FORE	445.00	1995	SI	–
23	SLHC21	120.00	6.05551840	46.23579456	GR, DT, RHOB, FORE	406.00	1995	SI	–
24	SLHC22	120.00	6.05552590	46.23549085	RHOB	118.87			–
25	SLHC23	110.18	6.05494650	46.23530551	GR, Vp, RHOB, FORE	400.00	1995	SI	–
26	SLHC24	110.30	6.05526740	46.23526275	GR, Vp, RHOB, FORE	419.00	1995	SI	–
27	SLHC25	109.40	6.05502810	46.23494617	GR, Vp, RHOB, FORE	401.00	1995	SI	–
28	Thônex-1*, ***	2580.00	6.21131960	46.20183865	CALI, GR, SP, DT, RHOB, ILD, ILM, LLD, LLS, NPHI	-	1993	GX	Cuttings****

Well-logs: *GR* gamma-ray, *URAN/THOR/POTA* spectral GR as uranium, thorium and potassium concentration curves, *SP* spontaneous potential, *DT* sonic travel-time, *RHOB* bulk density, *RHOMAA* apparent matrix density, *DRHO* corrected bulk density, *PEF* photoelectric factor, *NPHI* neutron porosity, *SN/RS* short normal resistivity, *LN/RD* long normal resistivity, *SFL* spherically focused, *MSFL* micro-spherically focused resistivity, *LLS* shallow latero-log, *LLD* deep latero-log, *FORE* focused resistivity, *LAT* medium lateral resistivity, *LIM* micro-inverse resistivity, *INV* inverse lateral resistivity, *ILD* deep induction, *ILM* medium induction, *Vp* compressional wave velocity, *Vs* shear wave velocity. Drilling purposes: *E&P* hydrocarbon exploration, *SI* site investigations within the scope of regional civil engineering projects, *GX* geothermal exploration. *No well-log digitisation required. ***Vp* & *DT* performed on rock core samples (Hefny, et al., 2020). ***Deviated well. ****Samples taken as part of geothermal studies

3.2 Modelling of the FCC's well density coverage

Besides the digitized geophysical logs from 28 selected wells, the 661 boreholes relevant to the FCC were gridded and modelled to account for its well density coverage supporting future site investigations in favour of optimal well placement. The SURFER software package by GoldenSoftware was used to grid and model the data using Kriging and Nearest-Neighbour algorithms. A grid size of 41 × 100 m was created with 4′100 nodes. X-spacing was chosen to 0.014° ranging from 5.5°E to 6.9°E, while Y-spacing was set to 0.018° from 45.77°N to 46.5°N in World Geodetic System (WGS 1984) coordinate system.

3.3 Digitisation of geophysical well-logs and petrophysical calculations

Digitisation of well-logging intervals between 0 and ca. 1′000 m ASL, depending on elevation and corresponding intersection with the FCC depth interval, was performed on 28 selected wells (Table 1) to address the FCC's construction depth interval currently ranging from 100 to 300 m ASL. Sedimentological and geological core descriptions were carried out on analysed samples to establish a reference lithotype scheme assisting in the interpretation of geophysical well-log information. These lithotypes were defined based on macroscopical features such as texture, colour, consistency, composition, and sedimentary structures, cross-checked with well report documentation and further linked to geophysical well-logs to identify associated well-log patterns.

Geophysical well-logs such as gamma-ray (GR), sonic transit-time (DT), compressional (Vp) and shear-wave (Vs) velocity, caliper (CALI), spontaneous potential (SP), bulk and matrix densities (RHOB, RHOMMA), photoelectric factor (PEF) and corrected density (DRHO), neutron porosity (NPHI) as well as different types of resistivity logs, i.e. short normal (SN), long normal (LN), latero-log shallow (LLS), latero-log deep (LLD) and micro-spherically focused (MSFL) were digitized and quality-checked using the NeuraLog software. Data was outputted in LAS file format for further processing and interpretation in Schlumberger's Techlog software. Boreholes Gex-CD-01 to -07 were drilled by British Petrol France between 1982 and 1983 to constrain the depth domains and properties of the LFM formation (Chattian/Oligocene) and calcareous basement bedrock (Lower Cretaceous, formerly also known as *Urgonien*) for hydrocarbon exploration. The wells extend across the two French departments Ain and Haute-Savoie at the western edge of the GB along the Jura. The cumulative length of well data amounts to 2′517.32 m, of which 749.04 m were exposed as available rock cores. Encountered stratigraphic units belong chronologically to the Quaternary, Oligocene (Chattian), Eocene, and Early Cretaceous (Hauterivian and Barremian). Note that the Barremian stage (Cohen et al., 2013) is commonly named "Urgonian" in traditional western European stratigraphy referring to the Early Cretaceous. Hence, the occasional adoption of the term in this article is to refer to regional geological features. In the northern part of the GB close to the city of Geneva, wells Geo-01, Geo-02 and Thônex-1 were drilled for geothermal exploration and were used as reference datasets for gamma-ray log calibration. SPL-, SLHC- and C-wells were drilled for site investigations in the framework of the LEP, LHC and HL-LHC civil engineering projects on behalf of CERN, whereas the latter wells allowed sampling of rock cores.

During digitisation, some mis-fit and log-shift was compensated via stretching and squeezing of log curves but could not be completely solved due to bad original paper quality, often loosely glued, or poorly scanned. Furthermore, NPHI, Vp and Vs well-logs were limited to specific intervals ranging between 5 to 100 m, especially for wells addressing hydrocarbon exploration (E&P). Each well-log type and its associated digitisation, data processing and analyses are described in the following sub-sections.

3.3.1 Lithology logs: Gamma ray (GR) and spontaneous potential (SP)

Despite different well-logging campaigns tailored for different exploration purposes, either a GR or SP logging tool, mostly deployed by companies Schlumberger, Hydrolog or Hydro-Geo Environnement, were run in most of the wells, excluding well Gex-CD-02 (only DT log). This allowed a first distinction of sand- and shale-dominated depth intervals. Respective SP log measurements were run and displayed in increments of 20, 10 or 5 mV.

Due to the variability of GR log measurements within a timeframe of 70 years, different log units hampered the process of homogenizing the data set. Some of the GR logs were formerly measured in microgram Radon per ton (µgR/t), which required re-calculation to common log units (Eq. 1) adopted by the American Petroleum Institute (gAPI). Hence, unit conversion between µgR/t and gAPI was applied according to (Crain, 2021):

$$GR_{log} = GR_{\mu gR/t} \cdot 10 \tag{1}$$

with GR_{log} being the conversed gamma ray log value in gAPI and $GR_{\mu gR/t}$ being the original gamma ray log value in µgR/t. Different GR tool calibrations among older (mostly E&P) wells required normalization based on newer (GX) wells. While the new wells offered higher tool sensitivity, the old wells were adapted accordingly

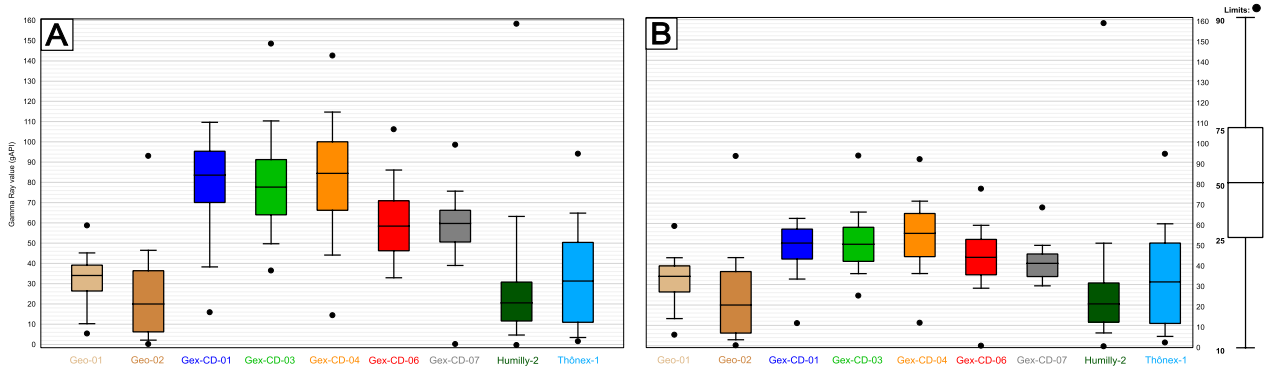

Fig. 2 Box plots of GR values before (**A**) and after (**B**) normalization. Middle line in box plots depicts mean values, circles denote extreme values (outliers). The latest geothermal exploration wells (Geo-01, Geo-02, Thônex-1) were used as calibration for older, hydrocarbon exploration wells (Gex-CD-01, -03, -04, -06, -07 and Humilly-2) to homogenize the datasets

despite removing potential shale- and sand-influenced (geological) trends (Fig. 2).

The gamma ray index (I_{GR}, Eq. 2) was calculated based on GR logs applying different models depending on geological formations for the derivation of the shale volume (V_{sh}): the Stieber Miocene/Pliocene Model (Eq. 3) for the Quaternary deposits, the Tertiary Larionov Model (Eq. 4) for the Molasse Rouge, Grès et Marnes Gris à gypse, and Siderolithic formations, and the Larionov Model (Eq. 5) for the underlying Mesozoic rocks according to (Schön, 2015):

$$I_{GR} = \frac{GR - GR_{min}}{GR_{max} - GR_{min}} \tag{2}$$

$$V_{sh} = \frac{I_{GR}}{3 - 2 \cdot I_{GR}} \tag{3}$$

$$V_{sh} = 0.083 \cdot \left(2^{\{3.7 \cdot I_{GR}\}} - 1\right) \tag{4}$$

$$V_{sh} = 0.33 \cdot \left(2^{\{2 \cdot I_{GR}\}} - 1\right) \tag{5}$$

where the GR_{min}-value of 10 gAPI was defined as the maximum sand-dominated zone, and the GR_{max}-value of 100 gAPI as the maximum shale-dominated zone, respectively. Due to the heterogeneity of the Molasse Rouge and Grès et Marnes Gris à gypse formations, X-Ray diffraction (XRD) and/or automated mineralogy and petrography scanning (QEMSCAN) laboratory analyses were performed to identify and support decisions for respective GR_{min} and GR_{max} values. High quartz value intervals were chosen as clean (sand) zones, respectively in the same manner for high fractions of clay minerals in shaly zones. A $GR_{cut\text{-}off}$ sand/shale cut-off value of 57 gAPI was chosen for all normalized GR logs.

3.3.2 Porosity & lithology cross-over logs: bulk density (RHOB), apparent matrix density (RHOMMA), corrected density (DRHO), photoelectric factor (P_e), neutron (NPHI) and sonic travel-time (DT)

Bulk density logs were run in a vast number of boreholes, while apparent matrix density was run explicitly in the geothermal well Geo-01. For the GX well-logs, corrected density logs (DRHO) were used to verify the original bulk density log run, whereas a value above 0.2 g/cm^3 was considered erroneous (Asquith et al., 2004) and the RHOB log was discarded in such intervals. RHOB and NPHI logs run in wells Thônex-1, Humilly-2, Geo-01 and Geo-02 allowed the identification of porous and likely more permeable zones. An overlap of these two curves indicated permeable, i.e. possible sand(stone)-dominated depth intervals, whereas a clear separation denoted low porosity and permeable, i.e. possible shale-dominated intervals. In addition, neutron porosity versus bulk density enabled the derivation of clay types, i.e. occurrences of laminated, dispersed or structural shale. This was further used for the calculation of the sand-silt-clay model and the identification of clay type distribution.

Based on low-energy gamma ray interaction measurements, the photoelectric index (P_e, Eq. 6) was derived from the PEF log in well Geo-01. This allowed for an advanced lithology distinction based on atomic numbers (Z) according to (Ellis & Singer, 2007):

$$P_e = \left(\frac{Z}{10}\right)^{3.6} \tag{6}$$

Total (PHIT) and effective (PHIE) porosities were calculated using the sonic log and were calibrated to laboratory measurements in the Molasse Rouge formation. While RHOB and NPHI logs offer additional methods of porosity calculations, in most wells full log intervals were

restricted to the sonic log, while NPHI logs were run only in short depth intervals. Therefore, the sonic log was used as the main indicator for all porosity calculations using the Wyllie time-average equation (Wyllie et al., 1956, Eq. 7):

$$\Delta t = \Delta t_{solid}(1-\phi) + \Delta t_{fluid}\phi \quad (7)$$

with an average Δt_{solid} of 47.5 µs/ft and Δt_{fluid} of 189 µs/ft. For effective porosity, the shale volume was subtracted from total porosity. No porosity calculations were performed in the Mesozoic limestone formations. Fig. 3 exemplarily depicts the full workflow output for petrophysical calculations and incorporation of all laboratory analyses including an updated, re-drawn stratigraphic log for well Gex-CD-01.

3.3.3 Resistivity logs: induction (ILD, ILS) and latero-log (LLD, LLS)

These logs were obtained by company Schlumberger deploying the 6FF40 induction log deep (ILD) tool, a short normal (SN) 16-inch, a long normal (LN) 64-inch log as well as shallow (15′ 0) and medium (18′ 8″) laterologs. The logs were run along specific intervals (E&P wells) for hydrocarbon detection and used for water resistivity calculation and quality control across logged formations. Unless provided (GX wells) or stated in well reports, the gradient method (Crain, 2021) was used to calculate the formation temperature FTEMP, assuming a surface temperature of 15 °C with a gradient of 3 °C per 100 m. This seemed reasonable since in-situ temperature for the exploitation of geothermal energy significantly increases at ca. 1′000 m below surface in the GB's Mesozoic limestone formations (Chelle-Michou et al., 2017), which is not intersecting the FCC's depth intervals in its current subsurface layout. Water resistivity was calculated for the derivation of the sand-silt–clay model in the Molasse Rouge formation considering FTEMP, and element concentrations of Na, K and Ca measured in the laboratory via inductively coupled plasma optical emission spectroscopy (ICP-OES). Analyses yielded average values of 0.5 Na, 0.2 K and 1.6 mg/g Ca, respectively, whereas chloride (Cl) concentration was assumed for 0.16 mg/g (Kafkafi et al., 2001). True, uninvaded resistivity (R_t) was taken from deep resistivity curves (LN, LLD, ILD), while invaded resistivity (R_i) was derived from shallow resistivity logs (SN, LLS). Flushed zone resistivity (R_{xo}) is commonly taken from a micro-spherically focused (MSFL) log, which was only available in well Gex-CD-07. Due to data limitations, the flushed zone was assumed for the invaded zone in all other wells, hence $R_{xo} = R_i$.

3.4 Sampling and laboratory analyses

A total of 930 samples across all geological formations in the Geneva Basin were analysed. Out of 930 samples, 785 were taken explicitly as part of the present study, and 145 samples during other geothermal studies (Brentini, 2018; Pierdona, 2018; Rusillon, 2018). QEMSCAN measurements included 418 samples in total, and 79 for XRD. A particular focus was hereby set on the Quaternary, Molasse Rouge and Grès et Marnes Gris à gypse formations restricted by the FCC construction depth.

Plugs with 2.5 cm in diameter and 2 to 8 cm in length were drilled from full-, half-cores and outcrops, and were prepared using abrasive tables to polish the top and bottom of each plug into planar surfaces, and subsequently split into different fractions for lithotype analysis. For well Geo-02, cuttings were consecutively taken during drilling progress. These were washed, sieved under water, and dried at 45 °C for ca. 60 h to prevent clay degradation. The dried samples were crushed in an agate mortar and sieved through a < 400 µm sieve. Consequently, these cuttings were used to create thin sections that were analysed via QEMSCAN, and produced under vacuum impregnation with epoxy resin. The brick was cut and flattened on one side before mounting on a glass plate with epoxy resin. After cutting the sample down to a thickness of a few 100 µm, it was further abraded before fine polishing down to 30 µm using silicon carbide abrasives. The final step included polishing with alumina by hand and a polishing machine.

3.4.1 Automated mineralogy and petrography scanning (QEMSCAN)

An FEI QEMSCAN Quanta 650F instrument was used to identify the modal mineralogy, texture, and lithotype of 273 thin sections, 26 samples from Thônex-1, 87 from Geo-01 (Pierdona, 2018) and 32 from Humilly-2 (Brentini, 2018; Rusillon, 2018) along the current FCC layout. Measurements were based on a scanning electron microscope (SEM) equipped with two energy-dispersive X-Ray (EDX) spectroscopy detectors, and used for correlations with well-logs. This non-destructive analytical technique enabled in-situ high-resolution (analytical point of < 2 µm) mapping (Pirrie et al., 2004). Mineral phase identification stemmed from the combination of back-scattered electron (BSE) contrast and EDS spectra providing information about the elemental composition (Gottlieb et al., 2000). Individual X-Ray spectra were compared to a library of known spectra comprising a specific mineral name and assigned to each individual acquisition point. The X-Ray EDS spectra library was initially provided by the manufacturer and has been further developed in-house using a variety of natural standards.

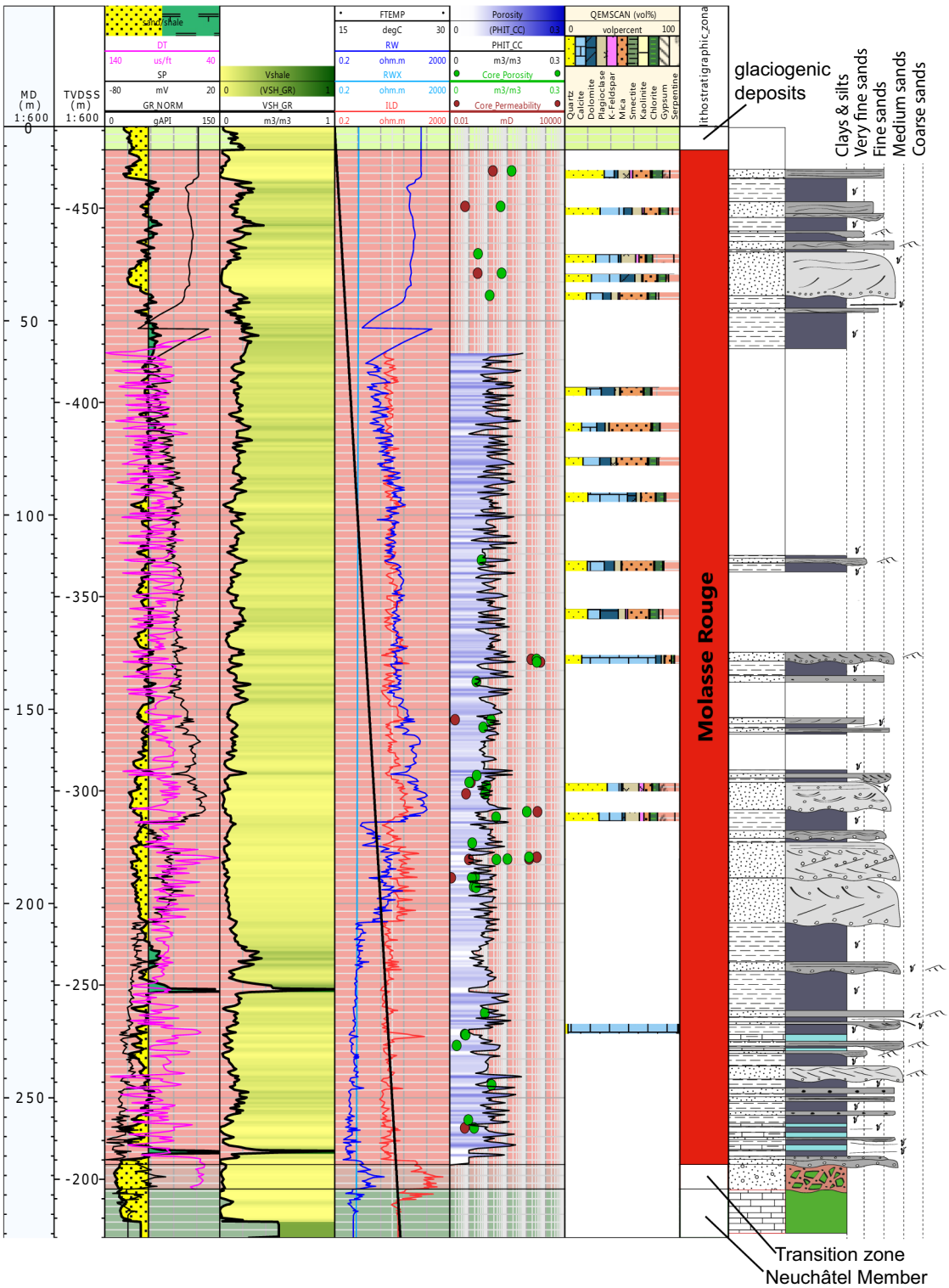

Fig. 3 Methodological approach depicting petrophysical calculations with revised stratigraphic log, associated geophysical well-logs and mineralogical laboratory results for well Gex-CD-01. White areas in QEMSCAN column represent no measurements. Note that the minerals illite, biotite and muscovite are summarized under the term "mica". Remaining space in QEMSCAN column refers to other minerals. *MD* measured depth (m), *TVDSS* true vertical depth subsea (m)

Measurements were performed at an acceleration voltage of 15 kV with a 10 nA probe current on polished thin sections, which were carbon-coated before scanning using a Quorum Q150T S/E/ES graphite coating device. X-Ray acquisition time was 10 ms per pixel using a point-spacing of 2.5 and 5 µm. Each section was scanned on a 1.5 × 1.5 cm area at 10 µm resolution to define textural parameters, mineralogical composition, and rock petrographic classification. Up to 122 individual view fields were measured in each sample, depicting 1.5 mm per single field. Data processing and analysis were performed using the FEI iDiscover software. Due to interstratified clay minerals and grain boundaries, which were not necessarily in compliance with the compared QEMSCAN mineral database, results contained a certain portion of unclassified minerals and limitations for clay minerals and interstratified clay minerals.

3.4.2 X-Ray diffraction (XRD)

A jaw crusher was used to crush the plug samples down to a fraction of < 400 µm, followed by a vibrating McCrone mill with agate balls to receive a < 20 µm fraction for subsequent XRD analysis. Samples were analysed according to standard DIN EN 13,925–1/-2 (European Norm (EN), 2003) using two different types of samples measured with a Bragg–Brentano X-ray diffractometer (D8 Advance, Bruker AXS/D). For quantitative XRD analyses, randomly oriented (Zhang et al., 2003), Ca-exchanged samples were scanned from 4 to 80° 2θ with steps of 0.02° 2θ at 2 s intervals. Oriented specimens were used for enhancement of the basal reflexes of layer silicates thereby facilitating their identification. The changes in the reflex positions in the XRD pattern by intercalations of organic compounds (e.g. ethylene glycol) and after heating were used for the identification of smectite (Brindley & Brown, 1980). The XRD instrument used CoKα-radiation generated at 35 kV and 40 mA and operated with dynamic beam optimisation using an automatic theta compensating divergence slit and a motorised anti-scatter screen. The diffractometer was equipped with primary and secondary soller slits, and an energy-dispersive LynxEye XE-T line detector. Qualitative phase analysis was conducted with the DIFFRAC. EVA v4.3 (Bruker AXS) software. The minerals were identified by peak positions and relative intensities in the X-Ray diffraction pattern compared with the PDF2 database. Mineral quantification was performed via Rietveld analysis of the XRD patterns using the Profex/BGMN V4.2.4 software (Doebelin & Kleeberg, 2015). This full pattern-fitting method calculates X-Ray diffraction patterns based on crystallographic data of each mineral phase and its iterative adjustment (least-square fit) to the measured diffractogram. For final refinement, phase specific parameters and the phase content were adapted to minimize the difference between the calculated and the measured X-Ray diffractogram. XRD results in wt.% of the n-th mineral were converted into percentage by volume (%, Eq. 8) using respective averaged and normalized mineral grain densities ρ, according to:

$$\mathrm{vol\%_{mineral}} = \frac{\frac{wt\%_{mineral}}{\rho_{grain}}}{\sum_{\mathrm{n}} \frac{wt\%_{n}}{\rho_{n}}} \tag{8}$$

Depending on available well-logs, either XRD, QEMSCAN or both analyses were used for correlations of sandy and shaly intervals. Shale volume derived from GR logs was compared with results of XRD analyses, which provided a more robust result for fine-grained clay particles (< 2 µm) compared to QEMSCAN measurements. Mineral abbreviations in respective figures were used after Whitney and Evans (2010).

3.4.3 Effective cation exchange capacity (CEC)

With the Cutrien complex method at pH 7-8 according to Meier and Kahr (1999), the effective cation exchange capacity (CEC) of Molasse Rouge samples was analysed. No measurements were conducted for samples from the Quaternary or Mesozoic deposits. The extinction at 578.0 nm was analysed in the Spectral-Photometer DR6000 (Hach Lange) and compared with the extinction value of the blind solution without added sample material. Effective CEC in meq/100 g was then calculated according to (Eq. 9):

$$\mathrm{CEC} = \frac{\left(Ext._{blind} - Ext._{sample}\right) \cdot 200 \cdot 100}{m_{sample}} \tag{9}$$

whereas $\mathrm{Ext._{blind}}$ and $\mathrm{Ext._{sample}}$ depicted respective extinction values in nm of the blind and real sample, and $\mathrm{m_{sample}}$ gave the sample mass in grams. Calculations were corrected by the water content of each < 63 µm sample. The exchange cations per unit pore volume, $\mathrm{Q_V}$, was calculated (Eq. 10) from selected plug samples based on laboratory CEC values, core porosity ($\phi_{\mathrm{eff,core}}$) and core grain density ($\rho_{\mathrm{grain,core}}$) measurements for wells C1, C2, C3, Gex-CD-02 and Gex-CD-04 to Gex-CD-07 (see below), and were extrapolated to Geo-01 for the Molasse Rouge formation. $\mathrm{Q_V}$ calculations were conducted according to (Darling, 2005):

$$\mathrm{Q_V} = \frac{\mathrm{CEC} \cdot \rho_{\mathrm{grain,core}}}{100 \cdot \phi_{\mathrm{eff,core}}} \tag{10}$$

3.4.4 Exchangeable cations via Inductively Coupled Plasma Optical Emission Spectrometry (ICP-OES)

Sample preparation continued with the centrifuged supernatant of the previous CEC measurement. The solution was filtered with < 0.45 µm PES vaccine filters and acidified with 2% HNO_3. Exchanged Na, K, Mg, Ca and further leachable elements (e.g. Ni, Cr) were quantified via ICP-OES using an Agilent 5110 ICP-OES device. Condition settings were adapted to 10 s of reading and 15 s stabilization time. Viewing mode was radial with a viewing height of 15 mm. For each sample run, a blank sample and 3 standards were used for calibration, followed by a quality control spike blank sample and a copper blank sample.

3.4.5 Water uptake capacity via Enslin-Neff

The Enslin-Neff analysis was performed to measure the water uptake capacity under free swelling conditions (Neff, 2005) and its associated time evolution of rock-water interaction following standard DIN 18,132 (Deutsches Institut für Normung (DIN), 2012). About 1 g of a < 400 µm sample was placed in an Enslin-Neff apparatus and its free water uptake over time until maximum was recorded (up to 1′440 min). The maximum water absorption reading (w_{max}) served for the calculation of the water absorption capacity, w_a in wt.% (Eq. 11) corrected by the dry mass, m_{dry}, according to:

$$w_a(\%) = \frac{w_{max}}{m_{dry} \cdot 100wt\%} \tag{11}$$

3.5 Core porosity, core permeability, and core grain density

The unsteady state pressure-decay technique after the modified Darcy's law was applied to measure effective porosity and absolute (single fluid) permeability with an AP-608 Automated Permeameter & Porosimeter (Chablais & Moscariello, 2012; Coretest Systems Inc., 2008, 2011) on a total of 170 Siderolithic, Molasse Rouge and Quaternary plug samples, and were further used for respective well-log calibration. The device measured porosity (percentage) and permeability (milli-Darcy, mD) in respective gas atmospheres. Plugs were analysed with nitrogen, and for selected samples with helium gas. The latter served as an ideal gas optimized for medium to high permeability values, whereas nitrogen was used for fine-grained Molasse Rouge samples expecting permeability values below 0.05 mD. The measurement analysed the equivalent liquid permeability, slip and turbulence factors. Pore volume measurements were retrieved using the gas expansion model based on Boyle's law. Grain densities were measured using the device's grain volume chamber. Before a set of measurements, a reference volume inside the grain volume chamber, which was filled with calibrated metal cylinders, was calculated yielding an average value of 10.99 cm^3. During each measurement, temperature was maintained constant at 58.3 °C. Nitrogen and helium viscosities were used for appropriate calculations. Results were corrected for the Forchheimer (Forchheimer, 1901) and Klinkenberg (Klinkenberg, 1941, Eq. 12) effects, with the latter providing a robust approximation of liquid permeability based on measured gas permeability, following Tanikawa and Shimamoto (2006):

$$k_g = k_l\left(1 + \frac{4cl}{r}\right) = k_l\left(1 + \frac{c\kappa}{\pi\sqrt{2r^3}}\frac{T}{p}\right) = k_l\left(1 + \frac{b}{p}\right) \tag{12}$$

with:

$b = \frac{c\kappa}{\pi\sqrt{2r^3}}$, whereas k_g is the permeability of gas (m^2), k_l depicts the permeability of liquid (m^2), l is the mean free path of gas molecules (m), r is the pore radius (m), κ the Boltzmann's constant (JK^{-1}), T the temperature (K), c is a constant, p is the pore pressure (Pa) and b is the Klinkenberg slip factor (Pa). In contrast to flowing liquids, the velocity of gas flowing through a porous medium is not zero at the wall but shows a slight increase. This correction factor compensates for gas slippage within pores when gas flows along pore walls.

4 Results

The FCC's ongoing feasibility phase requires the identification of encountered geological formations and the investigation of rock characteristics at its currently planned construction depth intervals between 100 and 300 m ASL for its main tunnel and experimental caverns. While subsurface designs are still subject to changes as additional information is collected from a wide range of well-log data and laboratory analyses, the current results impact admission into the subsequent technical design phase, associated environmental impact assessments, and ultimately, optimal well placement for upcoming site investigations.

Each data type is presented separately in the following sub-sections from local to regional scales. Visual geological rock core inspections show the highest resolution in the order of millimetres. Consecutive decrease in resolution is given by the geophysical well-logs with an average point density of 15.24 cm. A lithostratigraphic overview is depicted at outcrops within a few tens of meters (Fig. 4), followed by two distinct well correlation panels among the northern Gex well series (Fig. 5) and selected deeper wells along a NE-SW trend (Fig. 6), both within a few hundreds of meters in vertical and a few tens of kilometres in lateral extent.

4.1 Stratigraphy across the Geneva Basin

In the Geneva Basin, 22 geological formations and subunits featuring 31 lithotypes are encountered across 661 wells distributed within the FCC's construction area. These are described in the following sub-sections in order of decreasing geological age, and the FCC's intersected 13 geological formations and associated 25 lithotypes (Table 2), of which some are exposed in the field and analysed on rock samples. Fig. 4 shows the encountered lithotypes: A1 represents Quaternary unconsolidated deposits at a depth between 4 to 5 m in C5 well (close to CERN's HL-HLC Point 1), while A2 is comprised of gravelly Quaternary deposits at a depth from 32.25 to 39.25 m in well Montfleury-2. M1-M5 lithotypes depict different marl- and siltstones that vary in colour and grain size from very fine to fine-grained (M1-M2) in well Peissy-I at depth levels from 125.12 and 126.12 m and between 42.30 and 42.90 m, respectively. A brownish-violet, often referred to as *lieu de vin* (M3), marl lithotype is encountered e.g. in well Gex-CD-01 at a depth from 40.96–41.90 m, and beige (M4) coloured lithotype is encountered in Peissy-I at a depth between 82.50 and 83.46 m. Conglomeratic, low sphericity grains in a clayey matrix of siltstone (M5) are located at a depth between 124.12 and 125.12 m in well Peissy-I. S1-S4 show partly hydrocarbon-impregnated sandstone (S1) at a depth between 100.69 and 101.51 m, fine-laminated silty sandstone (S2), massive, compact sandstone (S3) at a depth between 58.95 and 59.90 m, and porous, fine-grained sandstone (S4), all cored in well Peissy-I. HC depicts a hydrocarbon saturated sandstone lithotype in Gex-CD-01 at a depth of 188.10 m, and very fine-grained, laminated sandstone (S5) is encountered in well Gex-CD-04 at 120.22 m. C1 and C2 represent conglomeratic lithotypes differentiated by colour and grain size at depth levels 233.20 m and 188.70 m in Gex-CD-01, respectively. G1 depicts the Siderolithic Formation, often referred to as *Gompholite*, drilled from an outcrop close to Mornex in the northern part of the GB (Fig. 1). The L lithotype depicts Molasse Rouge freshwater limestone encountered in Gex-CD-07 at a depth of 234.7 m. The AG lithotype depicts a fine layer of gypsum in an outcrop close to Nyoux, while S6 represents the Siderolithic Formation outcropping near Sarzin close to an abandoned quartzite

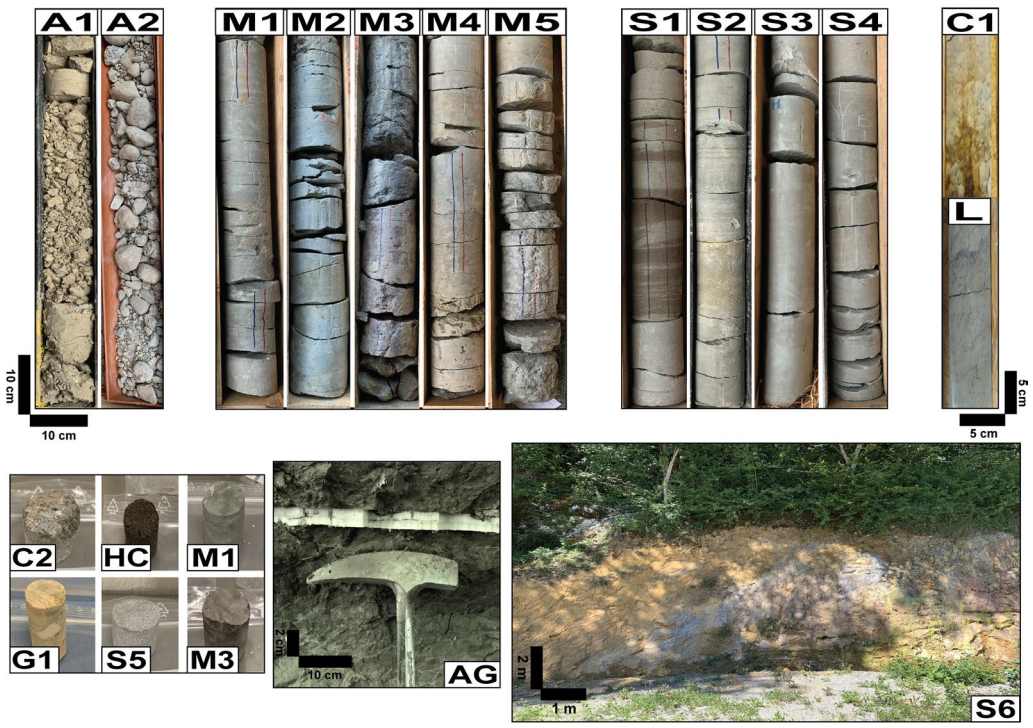

Fig. 4 Lithotypes analysed and encountered along the FCC's current tunnel alignment from small-scale drilled plugs to rock cores and large-scale outcrops. *A1–A2* Quaternary glaciogenic deposits, *M1–M5* different marls as part of the Molasse Rouge formation, *S1–S5* different sandstones as part of the Molasse Rouge formation, *S6* sandstone as part of the Siderolithic formation, often referred to as *Gompholite*, *HC* hydrocarbon-bearing sandstone in the Molasse Rouge formation, *C1-C2* different conglomerates as part of the Molasse Rouge formation, *L* freshwater limestone as part of the Molasse Rouge formation, *G1* sandstone as part of the Siderolithic Formation, *AG* gypsum layer in the Molasse Rouge formation. See text for detailed descriptions

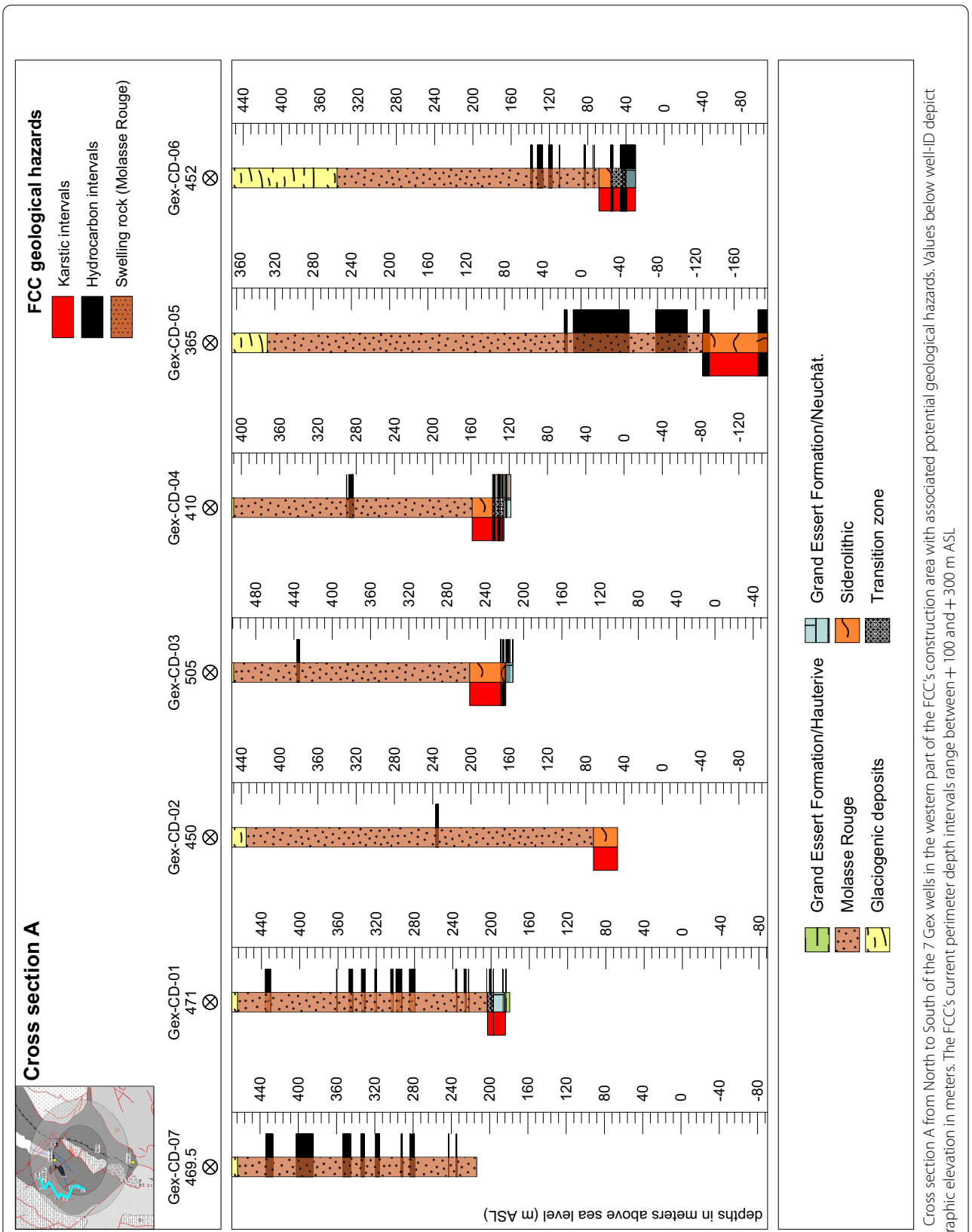

Fig. 5 Cross section A from North to South of the 7 Gex wells in the western part of the FCC's construction area with associated potential geological hazards. Values below well-ID depict topographic elevation in meters. The FCC's current perimeter depth intervals range between + 100 and + 300 m ASL

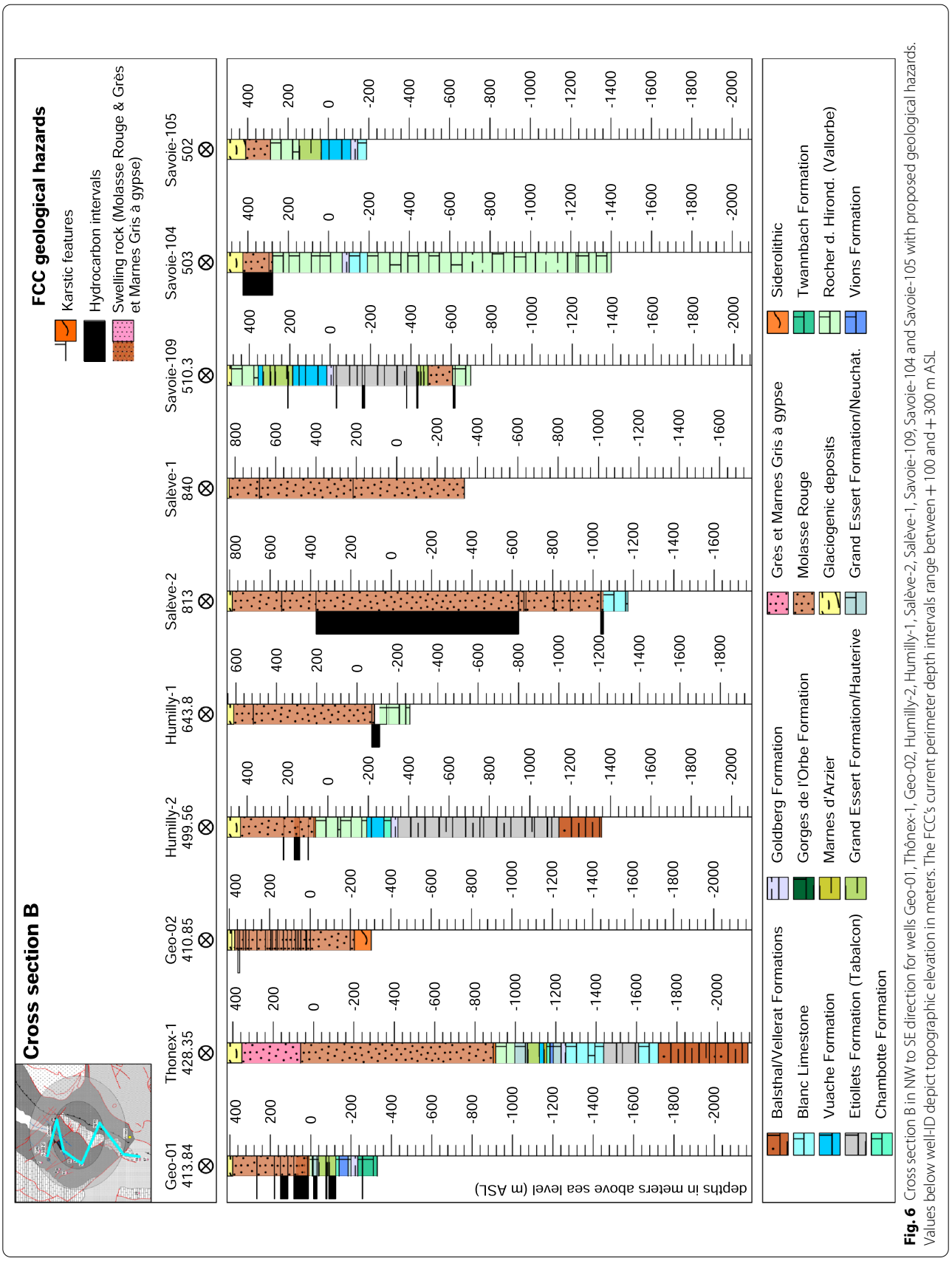

Fig. 6 Cross section B in NW to SE direction for wells Geo-01, Thônex-1, Geo-02, Humilly-1, Salève-2, Salève-1, Savoie-109, Savoie-104 and Savoie-105 with proposed geological hazards. Values below well-ID depict topographic elevation in meters. The FCC's current perimeter depth intervals range between + 100 and + 300 m ASL

Table 2 Lithostratigraphic column for the Geneva Basin and geological tunnelling hazards linked to different lithotypes potentially relevant for FCC construction

Period	Epoch	Stage	Rock types	Lithostratigraphic notations	lithostratigraphy (this study)	lithotypes (this study)	abbreviation of lithotypes (see Fig. 4)	FCC's geological hazards (this study)
Quaternary		Holocene	Absent	Absent	**Topsoil**	**Topsoil**	**Topsoil**	
	Pleistocene	Late	Silty-Clayey Gravel, Conglomerate	Glaciogenic deposits, LGM moraines	**Post-glacial sediments, LGM moraines**	**Clayey to (sometimes) sandy gravel mixtures, clast with grey-beige plastic consistency**	**A3**	Active faults
					Cemented & unconsolidated, interglacial sediments	**dark grey, clayey mud- and wackestone with pollen traces**	**A2**	Water-bearing aquifers
		Middle			**Pre-glacial sediments**	**Mixture of fine sand and sandstone embedded in clayey matrix**	**A1**	Water-bearing aquifers
Paleogene	Oligocene	Serravalian	Conglomerate	Upper Freshwater Molasse (UFM)	**Absent**	**Absent**	**Absent**	Absent
		Langhian	Sandstone, marl	Upper Marine Molasse (UMM)	**Absent**	**Absent**	**Absent**	Absent
		Burdigalian	Sandstone		**Absent**	**Absent**	**Absent**	Swelling clays, anhydrite (AG), hydrocarbons (HC), active faults
		Aquitanian	Molasse Grise	Lower Freshwater Molasse (LFM), (Molasse Rouge*, Grès et Marnes Gris à gypse*)	**Absent**	**Absent**	**Absent**	Swelling clays, anhydrite (AG), hydrocarbons (HC), active faults
		Chattian	Grès et Marnes Gris à gypse, Molasse Rouge (upper and lower succession)		**Grès et Marnes Gris à gypse, Molasse Rouge as part of LFM**	**Upper succession: sandstone with intercalations of marly siltstone lower succession: clayey limestone, breccia, sandstone, alternating thin beds of very fine to fine sandstone, laminated clayey siltstone Anhydrite/gypsum layers Hydrocarbon-bearing sandstone. Limestone**	**S1, S2, S3, S4, S5; M1, M2, M3, M4, M5; AG; HC; L**	Swelling clays, anhydrite (AG), hydrocarbons (HC), active faults
		Rupelian	Sandstone, conglomerate	Lower Marine Molasse (LMM)		**Conglomerate(?), part of Siderolithic(?)**	**C1, C2**	Swelling clays, anhydrite (AG), hydrocarbons (HC), active faults
	Eocene		Sandstone	Siderolithic	**Siderolithic**	**Conglomerate with quartz and limestone in clayey cement**	**C1, C2, S6, G1**	Karst, hydrocarbons, active faults
Transition zone (Perte-du-Rhône Formation?)**					**Transition zone**	**Not stratified, karstic sandstone alternations(?)**	**KS**	Karst, hydrocarbons, active faults

Table 2 (continued)

Period	Epoch	Stage	Rock types	Lithostratigraphic notations	lithostratigraphy (this study)	lithotypes (this study)	abbreviation of lithotypes (see Fig. 4)	FCC's geological hazards (this study)
Cretaceous	Early	Barremian	Limestone, often marly	Vallorbe Member of the Rocher des Hirondelles Formation and Gorges de l'Orbe Formation (both formerly represented by the Urgonien)	**Vallorbe Member of the Rocher des Hirondelles Formation**	**Massive limestone**	**ML**	Karst, hydrocarbons, active faults
		Hauterivian	Marly to silty limestone	Vallorbe Member of the Rocher des Hirondelles Formation and Gorges de l'Orbe Formation (both formerly represented by the Urgonien), Grand Essert Formation (Hauterive Member and Neuchâtel Member)	**Vallorbe Member of the Rocher des Hirondelles Formation, Grand Essert Formation (Hauterive Member and Neuchâtel Member)**	**Marly-sandy limestone, sometimes dolomitic, mud- /wackestone; limestone with siltstone**	**MSLd, MLs**	Karst, hydrocarbons, active faults
		Valanginian	Marl and sandstone alternations with intercalations of limestone	Grand Essert Formation (Hauterive Member), Vuache Formation	**Grand Essert Formation (Hauterive Member), Vuache Formation**	**Marly-sandy limestone, sometimes dolomitic**	**MSLd**	Karst, hydrocarbons, active faults
		Berriasian	Limestone	Goldberg Formation, Chambotte Formation, Pierre-Châtel Formation, Vions Formation, Neuchâtel Member	Goldberg Formation, Chambotte Formation, Pierre-Châtel Formation, Vions Formation, Neuchâtel Member	Massive limestone; marly-sandy limestone, biomicrite and wacke-/packestone	ML, MSL	Karst, hydrocarbons, active faults
Jurassic	Late	Tithonian		Twannbach Formation	Twannbach Formation	Massive, dolomitic, partly fine-grained limestone; dolomitic limestone, massive dolomite	L, Ld, MD	Karst, hydrocarbons, active faults
		Kimmeridgian		Twannbach Formation, Etiollets Formation (Tabalcon sub-unit), Blanc Limestone	Twannbach Formation, Etiollets Formation (Tabalcon sub-unit), Blanc Limestone	Dolomitic, clayey limestone, sometimes massive limestone	DCL, ML	Karst, hydrocarbons, active faults
		Oxfordian		Balsthal Formation, Vellerat Formation***	Balsthal Formation, Vellerat Formation***	Clayey to marly limestone and marlstone	CML, M1	

Bold area refers to the geology encountered by the FCC in its current subsurface layout. Rock types and lithostratigraphic notations after Blondel, 1984; Brentini, 2018; Burkhard & Sommaruga, 1998; Charollais et al., 2007; Deville et al., 1994; Graf & Burkhalter, 2016; Jaquet, 1966; Kissling, 1974; Moscariello, 2019; Strasser et al., 2016

*Molasse Rouge and Grès et Marnes Gris à gypse are commonly referred to informal but valid names as part of the LFM. **Currently under discussion but might imply new insights on the Mesozoic-Cenozoic boundary(?) as part of imminent research results for the GB. ***Currently under discussion, not yet fully defined. *LGM* Last Glacial Maximum

mine (Fig. 1). They substantially vary in vertical and lateral extent (Fig. 5, Fig. 6) and bear critical geological hazards and environmental contaminations as discussed and summarized in Table 2.

4.1.1 Balsthal Formation and Vellerat Formation

This Oxfordian interval is encountered by wells Brizon-1, Chaleyriat-1, Charmont-1 and Chatillon-1D close to the Jura in the western part of the GB, and by Humilly-2, La-Chandelière-1, La-Tailla, Musiège-1 and Thônex-1 comprising limestone, clayey to marly limestone and marl lithotype alternations. Except for well Chaleyriat-1 and La-Chandelière-1 with a starting depth at 18 m and 330 m extending down to 933 m and 726 m, respectively, average top depths among these wells range between 500 and 600 m. The exact stratigraphic terminology of these formations is currently debated.

4.1.2 Blanc Limestone Formation

This Kimmeridgian (Portlandian) formation is encountered in wells Faucigny, La-Chandelière-1, La-Tailla, Mont-de-Boisy-1, Musiège-1, Salève-2, Savoie-104 and Savoie-105 and Thônex-1, as dolomitic, often clayey limestone lithotype. While wells close to the Jura encounter this formation at shallow depths of about 67 m, wells distributed towards the South of the FCC perimeter intersect it between 600 and 800 m and extend down to about 1′986 m. Savoie-104 contains dolomitic limestone, whereas in its neighbour, Savoie-105, the lithotype becomes more massive and less dolomitic, starting at a depth of 605 m and 647 m, respectively. In Thônex-1, the formation is encountered as marly limestone of supposedly Portlandian age at a depth of 1′678.60 m and extends down into the Oxfordian from 2′038.60 to 2′136 m as massive limestone.

4.1.3 Etiollets Formation with Tabalcon Limestone sub-unit

Massive, often dolomitic limestone banks of Kimmeridgian age in the Etiollets Formation comprise the Tabalcon Limestone sub-unit encountered in wells Chapery-1, Humilly-2, La-Balme-1, La-Chandelière-1, Musiège-1, Savoie-106, -107, -109 and Thônex-1. The formation makes up a substantial portion of wells Savoie-106 and Savoie-107 starting from the top of the well down to 860 and 950 m depth, respectively, while for the other wells starting depths range between 846 and 1′100 m extending down to depths between 860 and up to 1′800 m in the Savoie wells, Humilly-2, Musiège-1, Chapery-1, Thônex-1 and La-Balme-1. The Etiollets Formation without the Tabalcon Limestone sub-unit differs due to the absence of dolomitic composition, making it a pure, massive limestone.

4.1.4 Twannbach Formation and Goldberg Formation

The Late Kimmeridgian to Tithonian Twannbach Formation is comprised of dolomitic limestone and massive dolomite. The Goldberg Formation is of Early to Middle Berriasian age and bears massive, dolomitic, partly fine-grained limestone. Wells encountering these formations are Chapery-1, Geo-01, Humilly-2, La-Tailla, Musiège-1, Savoie-105, -107, -108, -109 and Thônex-1, restricted to the FCC's western region, terminated by the Salève and Mandallaz lineaments to the east and south-east. Average depths start at about 420 m and extend down to 1′680 m in Thônex-1.

4.1.5 Pierre-Châtel Formation

This Middle Berriasian formation consists of oolithic, often bioclastic, white to reddish limestone and marly interstratifications, and tends to become more massive towards the top yet impregnated by oolitic and bioclastic intercalations. This formation is encountered in the wells closer to the Jura.

4.1.6 Chambotte Formation and Vions Formation

These two formations of Berriasian age are mainly encountered by the northern wells close to the Jura. The Chambotte Formation intersects wells Faucigny, Geo-01, Humilly-2 and Thônex-1 comprising massive limestone, while Brizon-1, Chapery-1, Geo-01, La-Balme-1 and Thônex-1 account for the Vions Formation, comprised of marly to sandy limestone. Top depths of the Chambotte Formation start between 530 and 812 m, and extend down to 600 to 800 m, with an exception in Thônex-1 ranging between 1′583 and 1′600 m. Adjacent thereto, the Vions Formation extends down to 1′000 to 1′300 m, with exceptions in Geo-01 to 600 m and Thônex-1 to 1′615 m.

4.1.7 Vuache Formation

This Valanginian formation, formerly referred to as the *Calcaire Roux* (Limestone Formation) (Charollais et al., 2007; Strasser et al., 2016), includes predominantly sandy to marly limestone, sometimes dolomitic, and is encountered in Brizon-1, Chapery-1, Humilly-2 and La-Balme-1 at depths between 700 and 1′000 m, while in the SPM and L135 wells, top strata are exposed at shallower depths between 72 and 160 m in the northern part of the FCC's construction area. The Savoie, La-Tailla and Musiège-1 wells encounter these formations at depths

varying between 342 and 470 m. In Thônex-1, the formation is restricted to the interval between 1′546.90 and 1′568.10 m.

4.1.8 Grand Essert Formation with Hauterive Member and Neuchâtel Member

This formation consists of two members: the Late Valanginian to Early Hauterivian Hauterive Member, formerly referred to as the *Marnes d'Hauterivian* facies (Brentini, 2018; Charollais et al., 2007) and the Early to Late Hauterivian Neuchâtel Member, formerly referred to as the *Pierre Jaune de Neuchâtel* facies (Charollais et al., 2007). The former is comprised of marly to sandy limestone, sometimes dolomitic, and predominantly ochre, bioclastic mudstone (Potter et al., 2005) and highly recrystallized wackestone. The formation is encountered at 370 m in Brizon-1, 864 m in Chapery-1, 453 m in Geo-01, 286 m in Gex-CD-01, at 0 m in La-Chandeliére-1, at 1′647 m in La-Tailla, 263 m in Musiège-1, at 356 m in Savoie-105, at 45 m in Savoie-108, 177 m in Savoie-109, at 107 m and 76.5 m in SPM1 and SPM15, and at 1′488 m in Thônex-1, respectively, becoming richer in clay before the overlying Neuchâtel Member. The Neuchâtel Member consists of limestone with minor associated marl, and ochre-coloured, glauconite-bearing, bioclastic wackestone/packstone, encountered in wells Chapery-1, Geo-01, Gex-CD-01 and -06, L130, La-Balme-1, La-Tailla, Musiège-1, SPM2, SPM11, SPM15 and Thônex-1. Typical for this formation is its richness in bivalve shell fragments. Top depths range in the GB's northern wells between 120 and 430 m, whereas Thônex-1 marks an exception starting at 1′425 m. Top depths of about 800 m are common due to the adjacent Jura mountains (Chapery-1) and associated elevated topography.

4.1.9 Rocher des Hirondelles Formation with Vallorbe Member

This Late Hauterivian to Late Barremian formation is encountered in wells Brizon-1, Chapery-1, Faucigny, Geo-01, Gex-CD-03, -04, -06, Grilly, Humilly-1, Humilly-2, L112, La-Balme-1, La-Tailla, Messery-1, Mont-de-Boisy-1, Musiège-1, Savoie-104, -105, -108, -109, SPM1-3, SPM5 and Thônex-1. In some well reports the differentiation between the Vallorbe Member and the Neuchâtel Member is not clear and refers to Barremian age. The main lithotype of this formation is massive limestone, often associated with sandstone and calcareous marlstone. Sandy-marly limestone is associated to the Vallorbe Member as well, when combined with the Neuchâtel Member. Together with the Late Hauterivian to Late Barremian *Gorges de l'Orbe* Formation, these two formations today represent the former *Urgonien*, as referred to in older well reports.

4.1.10 Transition zone and Siderolithic Formation

The Mesozoic-Cenozoic(?) Transition zone has been extensively researched in the past years. Its temporal relationship is not yet scientifically proven—as is its informal name used here—but the sandstone-bearing unit comprises an Eocene(?) siliciclastic formation including karstic alterations, which have been erroneously combined with the Siderolithic Formation in older well reports. Latest considerations suggest that these lithologies could be part of the *Perte-du-Rhône* Formation, also referred to as *Gault*.

The Siderolithic Formation consists of continental sandstone likely deposited in a fluvial environment with the sedimentary source derived from the detrital Triassic of the eastern edge of the Central Massif (Conrad & Ducloz, 1977). This zone has yet not been fully investigated, and ongoing, unpublished studies in conjunction with the Transition zone characterize it as an assembly of centimetric blocks of beige, glauconitic, bioclastic limestone of the Mesozoic basement, cemented by marly, glauconitic sandstone, with angular quartz on a multi-decimetre-scale, primarily encountered in all Gex wells at depths between 230 to 290 and 395 to 412 m, respectively, in well Geo-02 between 630 and 714 m. Very fine cemented sandstone is associated with this limestone lithotype. Certain core samples in Gex-CD-02 show the presence of polygenic conglomerates with quartz and limestone, embedded or perforated in a ferruginous, ochre clay cement. The Siderolithic Formation has been formerly referred to as the *Gompholite* facies (Charollais et al., 2007, 2013) and is encountered in wells Charmont-1, Chatillon-1D, Faucigny, Geo-02, Gex-CD-02 to -06, Humilly-2, La-Chandelière-1, Musiège-1, Savoie-106 and 107 as well as Thônex-1. Figure 4 (S6) shows an outcrop of the Siderolithic Formation in the northern part of the FCC construction area, yielding a high content of quartz (appr. 99%).

The GR log indicates a distinct offset to lower values in the respectively logged well-logs, while the SP log increase up to 10 mV across all wells for the Transition zone. The LN resistivity log shows a high offset from 20 to 2000 Ohm*m, similar to the SN although in the order of 2 to 20 Ohm*m. Both logs, along the SP log, associate increased values to a higher clay content. The DT log depicts a decrease of travel-time, making the Siderolithic Formation a slow formation in terms of compressional wave velocity, substantiating its potentially karstic,

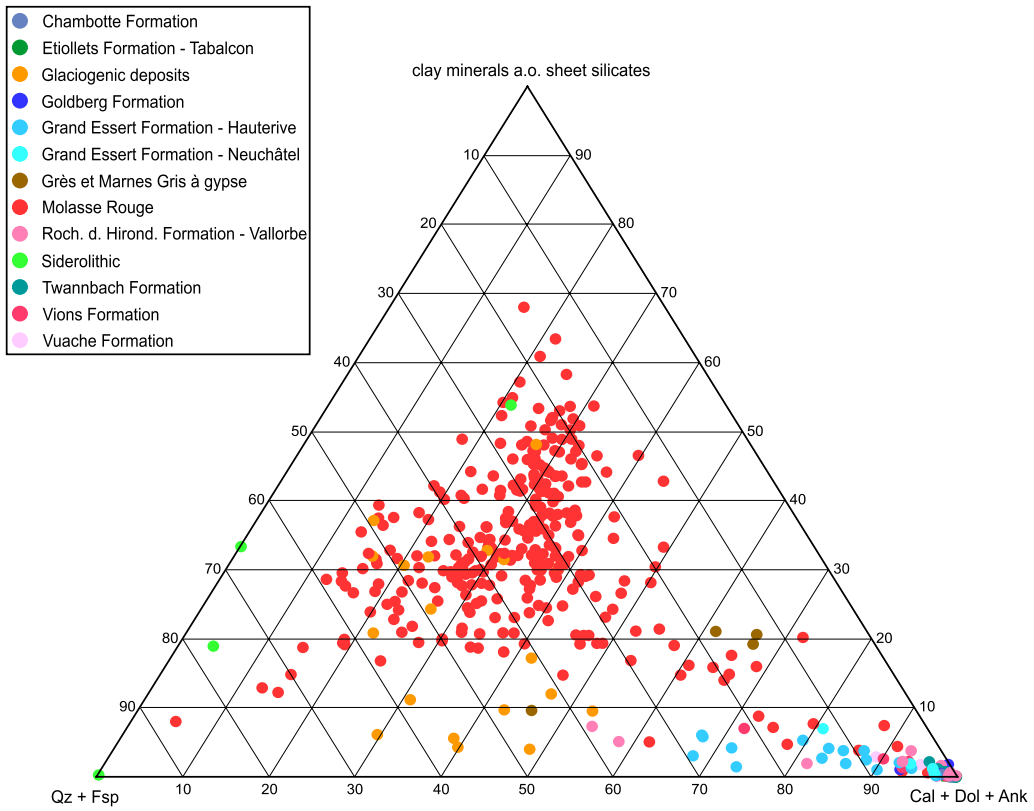

Fig. 7 Lithotypes for wells Montfleury-2 and L112 as well as outcrops Mornex, Biollay, Nyoux and Sarzin-R for various geological formations encountered in the Geneva Basin based on QEMSCAN measurements. Mineral abbreviations: *Qz* quartz, *Fsp* feldspar, *Cal* calcite, *Dol* dolomite, *Ank* ankerite

porous characteristics. GR values (< 57 gAPI) indicate sand-dominated intervals, which partly increase for a few meters when cemented with higher amounts of shale. This is also reflected by high resistivity values across all wells.

Mineralogical analyses (QEMSCAN) of related outcrops (Fig. 7) reveal an associated limestone lithotype. The Sarzin and Biollay outcrops (Siderolithic Formation) show a sandstone lithotype exceeding 90% in quartz by volume, with varying claystone content from 0 up to 34%. In contrast, the Mornex and Nyoux outcrops show a tendency towards a limestone lithotype. A characteristic feature compared to the overlying Molasse Rouge sandstone lithotypes, is the fact that Siderolithic sandstones do not appear stratified on both a micro- and macroscopic scale. This facilitates their identification in the field.

4.1.11 Molasse Rouge

The Molasse Rouge, often informally referred to as *Marnes bariolées*, comprising a subset of the LFM (Charollais et al., 2007, 2013; Kissling, 1974), is dated to Chattian age (Early Oligocene) and split into an Upper and Lower unit. The lower succession is dominated by clayey to partly silty limestone, making the Lower unit rich in clayey limestone from ca. 240 m down to the Transition zone in the Gex wells. Alternating thin beds of very fine to fine sandstone occur, rarely with medium and laminated, clayey siltstone or green, marly claystone. Nodular, highly bioturbated limestone with mollusc fragments were formerly correlated to the *Grilly* Formation (well Grilly) and interpreted as deposits of a palustrine environment (Charollais et al., 2007). The upper succession is comprised predominantly of sandstone with intercalations of marlstone across all wells, excluding those closer to the Jura. Freshwater limestone intermingled with palustrine breccias is associated with the lower succession. The sandstone of constant thickness is fine to medium-grained, showing a gradual decrease in grain size from top to bottom, with rather subangular grains and weak strength. This green-grey sandstone is comprised of quartz, feldspar, muscovite, and biotite,

sometimes occurring with soft, clayey pebbles dispersed in a clayey matrix in layers.

Encountered along the measured depth, the Savoie-109 well does exceptionally not transition into the Molasse Rouge, but directly into the limestone-bearing Rocher des Hirondelles' Vallorbe Member, equivalent to those encountered in the adjacent Rumilly and Valserine basins further to the south of the Geneva Basin. This well only shows Molasse Rouge at its base, which is also reflected by its higher drilling altitude compared to that of adjacent wells in this cross section.

The Molasse Rouge formation shows 13 lithotypes across all sampled wells (Figs. 5, 6, Table 2). This implies the necessity to define ranges for each mineral as measured by QEMSCAN and XRD analyses. Quartz, calcite and dolomite (ankerite) make up most of the formation with average values up to 80%, 50% and 25% by volume, respectively, but vary laterally across all wells from North to South. Calcite values reach up to 100% in Gex-CD-04 and -07 at about 200 m, representing the freshwater limestone lithotype (Fig. 8) associated to the Molasse Rouge. Total clay mineral volumes are quantified up to 60% (Fig. 9), constituting swelling potential in the Molasse Rouge.

GR log values vary between 5 to 100 gAPI across all wells with heterogeneous log patterns. The DT log remains at averaged constant values of 50 µs/ft, decreasing up to 20 µs/ft before entering the underlying Siderolithic Formation and Transition zone in e.g. the Geo-01 well. Resistivity logs remain at average values between 20 and 200 Ohm*m, except for thin depth intervals of a few meters bearing hydrocarbons, hence showing increased values above 200 Ohm*m. NPHI and RHOB logs show separated log curves, making the Molasse Rouge appear impermeable due to its shale content (Fig. 10). Permeable zones are only detected below the Molasse Rouge in the Transition zone and Siderolithic Formation, suggesting compacted, sandstone-bearing intervals (Figs. 9, 10).

4.1.12 Grès et Marnes Gris à gypse

The Grès et Marnes Gris à gypse is part of the LFM Molasse formation in the Geneva Basin, and an equivalent to the Molasse Grise towards the northern area of the western SMB around Lausanne preserved in the foredeep of the GB. According to various well reports, the Grès et Marnes Gris à gypse is encountered only in the Thônex-1 well (Fig. 10), making the northern part of the FCC construction area more likely exposed to the Grès et Marnes Gris à gypse, and suggesting complete erosion towards the south. The formation is dated to Late Oligocene (Middle/Upper Chattian) and is characterized by an increased amount of anhydrite/gypsum, intercalated in sandstone and marlstone of various grain sizes. While the northern boreholes (e.g. Geo-01 and Salève-1) directly transition into Molasse Rouge, the Thônex-1 marks an exception with Grès et Marnes Gris à gypse being encountered between 73 and 364 m. This complies with the fact that Grès et Marnes Gris à gypse lenses have been geologically mapped in FCC's northern construction area and are delimited by the syn- and anticline structures (Fig. 1). Further wells encountering the Grès et Marnes Gris à gypse are Messery-1 and Mont-de-Boisy-1, ranging from 18 to 560.50 m and 748 to 1′774 m, respectively. On the contrary, the C1-C3 wells do not show any traces of gypsum in the north-northwestern part of the basin.

In the Thônex-1 well, QEMSCAN measurements yield up to 30% of gypsum by volume, occurring as anhydrite in the subsurface, and decreasing towards the underlying Molasse Rouge. This is a decisive characteristic, as the FCC entirely crosses this formation in its currently planned subsurface alignment, raising concerns for operations and maintenance due to anhydrite swelling potential in this formation (Fig. 9).

Log differences between the Molasse Rouge and Grès et Marnes Gris à gypse are difficult to establish, and only slightly visible in lower averaged SP values ranging around − 20 mV in the Grès et Marnes Gris à gypse formation, compared to the Molasse Rouge of − 10 to + 20 mV. The distinctive characteristic remains the increased anhydrite/gypsum content in the Grès et Marnes Gris à gypse formation.

4.1.13 Glaciogenic deposits

Glaciogenic sediments of Quaternary age, often mistakenly grouped as the "Moraine Formation" in technical reports, summarise terminologically deposits that were influenced by glaciers, glacial erosion/deposition or subsequent geomorphological processes, and formed during last pre-glacial, post-glacial, glacial and interglacial periods. They consist of compacted till made of sandy to clayey gravel mixtures, often with 0.5 to 2 cm-sized clasts of grey-beige plastic consistency and a mixture of fine-grained sand, embedded in a beige, clayey matrix. These sediments are encountered by all wells and range from about 2 m to up to 110 m depth, overlying the Molasse Rouge or Grès et Marnes Gris à gypse in e.g. wells Thônex-1, Messery-1 and Mont-de-Boisy-1. The greatest thicknesses are encountered in wells Gex-CD-05 and Gex-CD-06 with 37 and 110 m, respectively. However, these glacial deposits are typically irregular in thickness and lateral changes

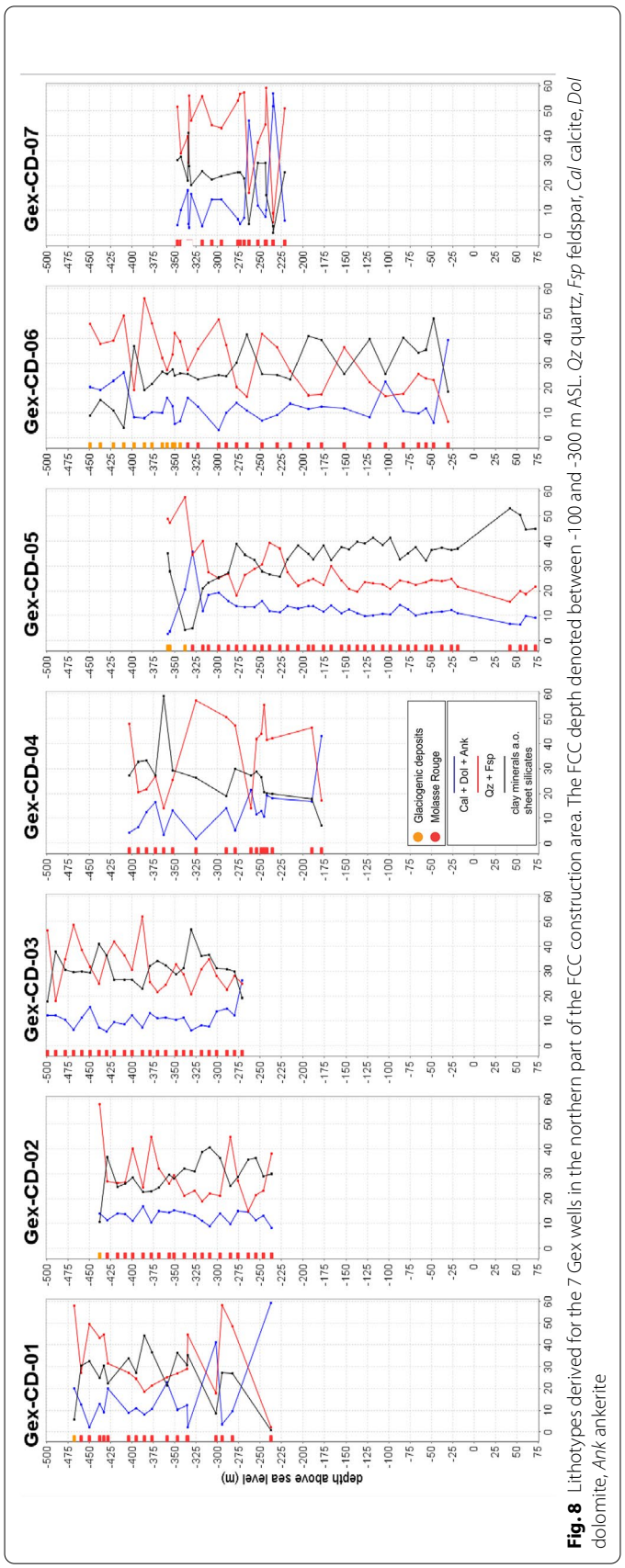

Fig. 8 Lithotypes derived for the 7 Gex wells in the northern part of the FCC construction area. The FCC depth denoted between -100 and -300 m ASL. *Qz* quartz, *Fsp* feldspar, *Cal* calcite, *Dol* dolomite, *Ank* ankerite

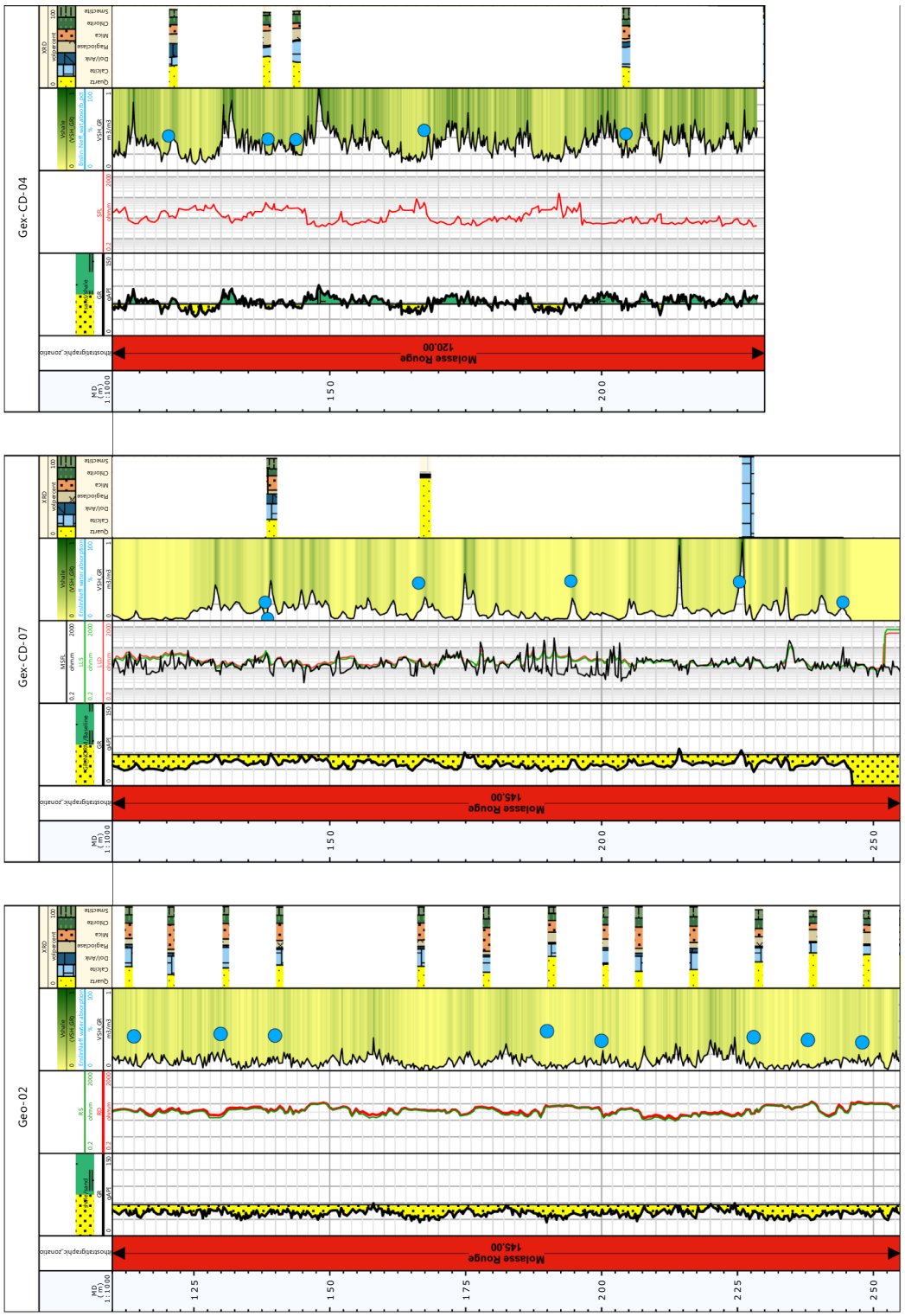

Fig. 9 Wells Geo-02, Gex-CD-07 and Gex-CD-04 wells showing mineralogical measurements in comparison to calculated shale volume from GR log

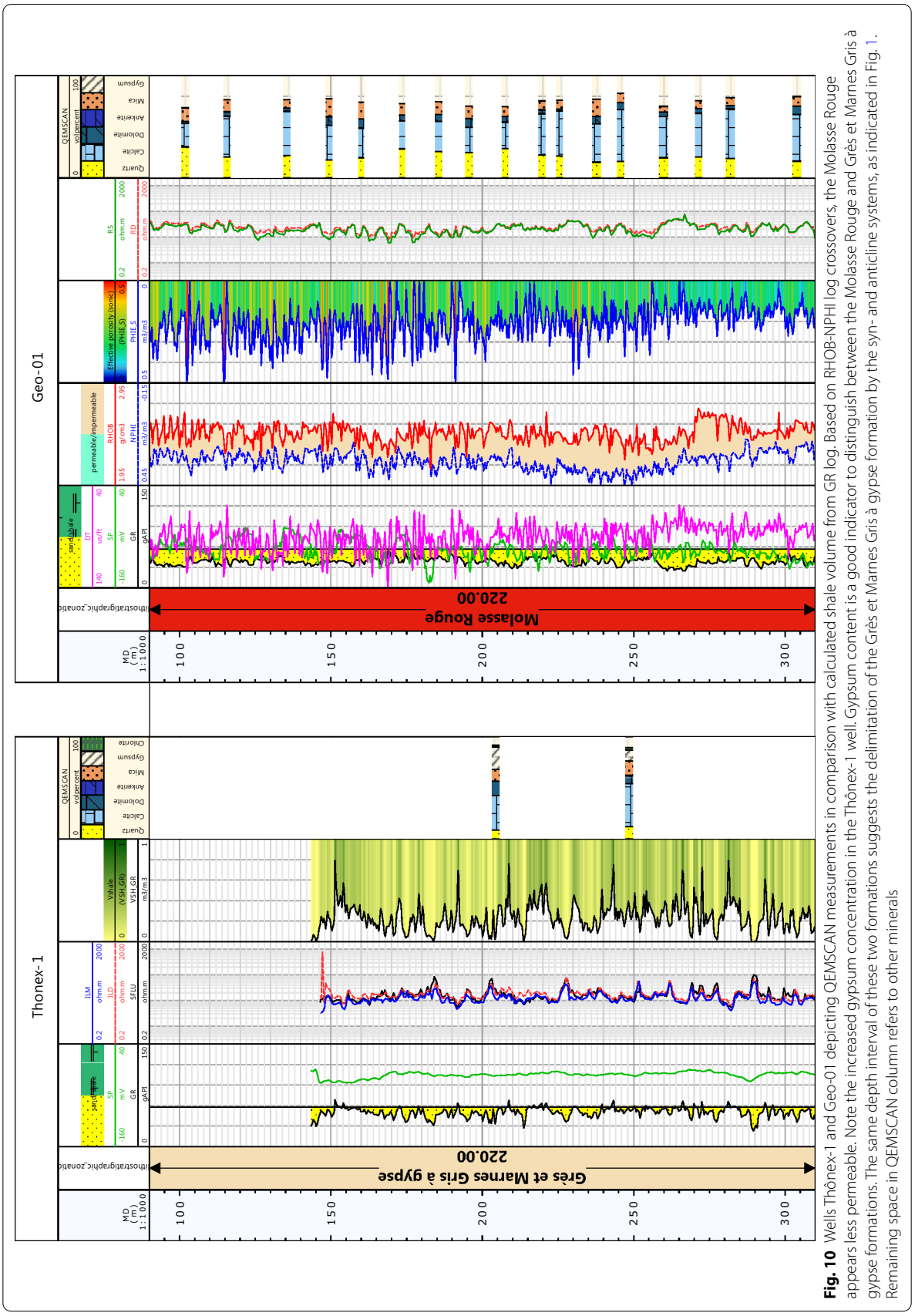

Fig. 10 Wells Thônex-1 and Geo-01 depicting QEMSCAN measurements in comparison with calculated shale volume from GR log. Based on RHOB-NPHI log crossovers, the Molasse Rouge appears less permeable. Note the increased gypsum concentration in the Thônex-1 well. Gypsum content is a good indicator to distinguish between the Molasse Rouge and Grès et Marnes Gris à gypse formations. The same depth interval of these two formations suggests the delimitation of the Grès et Marnes Gris à gypse formation by the syn- and anticline systems, as indicated in Fig. 1. Remaining space in QEMSCAN column refers to other minerals

Fig. 11 Matrix density versus volumetric photoelectric factor for the derivation of lithotypes based on well-log calculations from Geo-01's density logs. Formation depths in meters are stated in square brackets

are caused by depositional or erosional processes. The post-glacial sediments are mostly fluvial and lacustrine and show a harder consistency, while the LGM moraines depict till and show a more loose but sticky consistency.

Interglacial deposits were formed between the glacial periods in the Late/Middle Pleistocene and occur either in cemented or unconsolidated form, while post-glacial deposits overlay these interglacial deposits. The latter consist of coarser gravel and sand, also commonly referred to as *Alluvion Ancienne*, which overlay fine-grained sediments in e.g. the Montfleury-2 well (Wegmüller et al., 1995). The post-glacial deposits consist of thick packages of variably cemented coarse gravel and sand, most likely deposited in a pro-glacial fluvial environment. These deposits are in-situ intercalated with dark-grey, clayey mudstones with traces of pollen.

GR logs show a tendency towards sandy intervals (low values) compared to the underlying Molasse Rouge, similar to the unconsolidated glacial sediments. Related DT logs show high values of 120 µs/ft, indicating loose, unconsolidated characteristics of these deposits. However, most logs show erroneous values since their data processing and theoretical analyses are based on consolidated rather than loose and unconsolidated rock.

4.1.14 Topsoil

Holocene (recent) topsoil commonly marks the first 2 m of wells, represented by gravelly to sandy, unconsolidated material. Among the well reports depicting topsoil descriptions over a period of 70 years, two terms are interchangeably used: the term "colluvium" referred to a mixture of eroded, unconsolidated slope deposits, while the obsolete term "alluvium" was used to indicate fluvial deposits. These intervals are not logged.

4.2 Petrophysical lithotyping

Based on gamma-ray interaction logs (RHOB, PEF) and preceding calculated petrophysical parameters, lithotypes from logging curves are derived (Fig. 11) for well Geo-01 in the northern part of the basin, with a focus on the FCC's encountered Quaternary, Molasse Rouge, Grand Essert Formation's Neuchâtel and Hauterive members. A three-mineral model is assumed depicting quartz, calcite, and dolomite. The log lithotype model shows a quartz-dominated interval in the Hauterive

Member and Neuchâtel Member, with a matrix density between 2.70 and 2.75 g/cm^3 and a volumetric photoelectric factor between 4 to 8 b/cm^3, influenced by silty to clayey components. The Molasse Rouge formation shows a heterogeneous matrix density distribution between 2.55 and 3.13 g/cm^3 with volumetric photoelectric factors of 4 up to 16 b/cm^3. Occurrences of muscovite are observed in log lithotypes, and the mineral variations are well represented in the mineralogical analyses. The calcareous formation contains dolomite and calcite, which are both well captured by the PEF log. The glaciogenic deposits reflect a similar behaviour, with less variations for the matrix density ranging up to 2.95 g/cm^3, and showing lesser abundance in muscovite.

5 Discussion

5.1 Geological formations encountered by the FCC

The number of geological formations possibly encountered by excavation and engineering operations for the FCC construction depends on its final tunnel alignment but is hereby established and discussed on the current layout (Abada et al., 2019) and available information. Understanding the basin's geological history is important for the FCC as it enables making reasonable assumptions and stratigraphic concept extrapolations to regions which might have not yet been investigated but would be targeted in future investigations.

The latest feasibility phase layout ranges at depth intervals between the highest topographic level (shaft construction) and 100 to 300 m ASL (main tunnel and experimental cavern construction), and intersects 13 geological units comprising 25 lithotypes. With respect to the basin's architecture, the LFM Molasse Rouge sediments seem to onlap the Cretaceous formations in the Salève wells, while the Vuache Fault might have acted as a separation of continental and marine lithostratigraphic Molasse formations, separating the Chattian and Rupelian successions in the western part of the Geneva Basin. This suggests that the region to the west of the Salève may have been uplifted relative to the adjacent eastern Bornes Plateau (Fig. 1), potentially having caused less exposure to humid climate at the Bornes Plateau and complying with proposed influences of Molasse Rouge erosion in the literature. As depicted in Fig. 1, the Rupelian formations were deposited next to the Subalpine chain in the eastern part, substantiating the view of uplift and causing erosion in the western part. However, the encountered Siderolithic Formation, which is likely to have been eroded to the east of the Salève, indicates thickening towards the Jura in the north-west. This would infer a (shallow) marine environment during its deposition in the hinterland of the Geneva Basin and a continental environment in its foreland, likely to be part of karstic intervals and following an extension of the model proposed by Kaelin and Kempf (2009). Considerations on geological climate conditions could be significant at this point since hydrocarbon occurrences are predominantly linked to marine conditions. The Salève wells being positioned close to the Vuache Fault, encounter reduced thicknesses of Molasse Rouge sediments compared to the northern wells. This could infer two different settings across the Geneva Basin: a predominant continental environment in the north-east and a marine one in the south-west of Burdigalian(?) age, which might have been likely connected during the Chattian leading to thick accumulations of Molasse Rouge deposits in the north-eastern part of the Geneva Basin (Moscariello et al., 2014). This might hamper the FCC construction by increased hydrocarbon accumulations in the realm of the GB towards the south-southwest, where the proposed marine environment conditions prevailed during accumulation. Furthermore, these hydrocarbon indices might follow migration paths created along fault systems such as the Vuache Fault as well as the northern syn- and anticline structures that also seem to delimit the Grès et Marnes Gris à gypse formation in the northern part of the basin.

The identified hiatus of about 72 Ma (Allen et al., 1991; Sinclair & Allen, 1992; Sinclair et al., 1991; Trümpy, 1973) separates rocks of Aptian age in the Geneva Basin (Brentini, 2018; Rusillon, 2018) from the overlying Siderolithic Formation of estimated Eocene(?) age (Charollais et al., 2007). This hiatus resulted probably from subaerial exposure and consequent development of an erosive and deep karst system at the top of the Mesozoic series, which played a predominant role in the establishment of an aquifer drainage system within Cretaceous and Jurassic limestones across the GB, and implies karstic hazards for the FCC construction at these depth intervals.

5.2 Modelling of well density

The FCC's current feasibility phase requires the evaluation of existing wells, which allow the interpolation and extrapolation (modelling) of geophysical well-log data, stratigraphic information, and laboratory analyses to deduce subsurface information on regions with low or no data coverage. The modelling result aims for optimal well placement as part of upcoming site investigations. Consecutive site investigations are planned to narrow down final shaft placement and surface installations. Well density coverage modelling is based on wells located within a 2 km radius of the

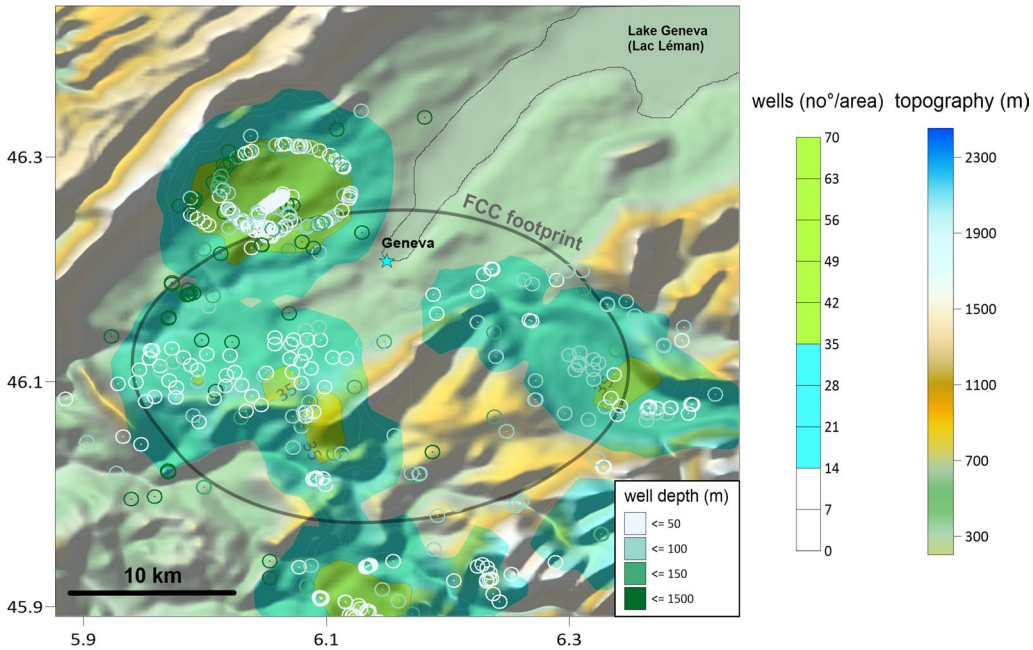

Fig. 12 FCC well-data density coverage map based on its current tunnel alignment based on 661 wells. The model will be updated following the results of future site investigations

FCC's current layout. Therefore, for this model wells located within the FCC ring perimeter and along a lateral extension of up to 2 km outside of the ring have been accounted for, filtered for a minimum depth of 10 m from topographic level to 300 m ASL (Fig. 12). There is a distinct lack of wells between the southernmost point (Jura, "Mandallaz limestone") and the easternmost point at the Bornes Plateau (Fig. 1), as well as to the east of Lake Geneva along the FCC footprint. It is suggested that future site investigations, e.g. seismic surveys and drilling campaigns, should first aim for these areas. Relevant correlation and laboratory data from this study should then be integrated with the gathered measurements. Assuming the encountered stratigraphy and similar rock behaviour, no additional laboratory analyses would have to be conducted, as the information compiled for this study is abundant.

5.3 Lithotype analysis

Based on rock core samples and well reports, the topsoil, post- and interglacial unconsolidated deposits comprise a mixture of conglomerate and sandy-gravelly clay of fluvio-glacial origin. The lithotypes associated to the Molasse Rouge formation consist of irregular alternations of sandstone, often bearing hydrocarbons (Figs. 7, 8), siltstone and claystone (Figs. 8, 13), divided into an upper sandstone succession (Upper Chattian) and a lower clay-limestone succession (Lower Chattian), as well as layers of anhydrite/gypsum, then transitioning into pure limestone lithotypes in the underlying Mesozoic units of the Jura. The Grès et Marnes Gris à gypse comprises higher amounts of anhydrite/gypsum and shows higher volumes of limestone lithotypes (Fig. 13) in the northern part of the FCC construction area compared to the Molasse Rouge. The Siderolithic Formation and Transition zone consist of beige sandstones and karstic breccias with carbonate elements of the substratum embedded in clayey sands. The Cenozoic Neuchâtel and Hauterivian members of the Grand Essert Formation feature massive limestones and ochre, bioclastic, glauconitic marls. Karstic limestones are encountered in the Cretaceous Vallorbe Member of the Rocher des Hirondelles Formation towards the FCC's southern construction area. The goal of the sand-silt–clay model (Fig. 14) was to derive estimate volumes of sand, silt and dry clay, as well as respective clay bound water and formation water solely based on well-logs to set them into context with lithotypes derived from cores. This also includes qualification of the clay type, i.e. dispersed, laminated, or structural, to correlate and associate the quantified volume with swelling clays in both the Molasse Rouge and Grès et Marnes Gris à gypse formations.

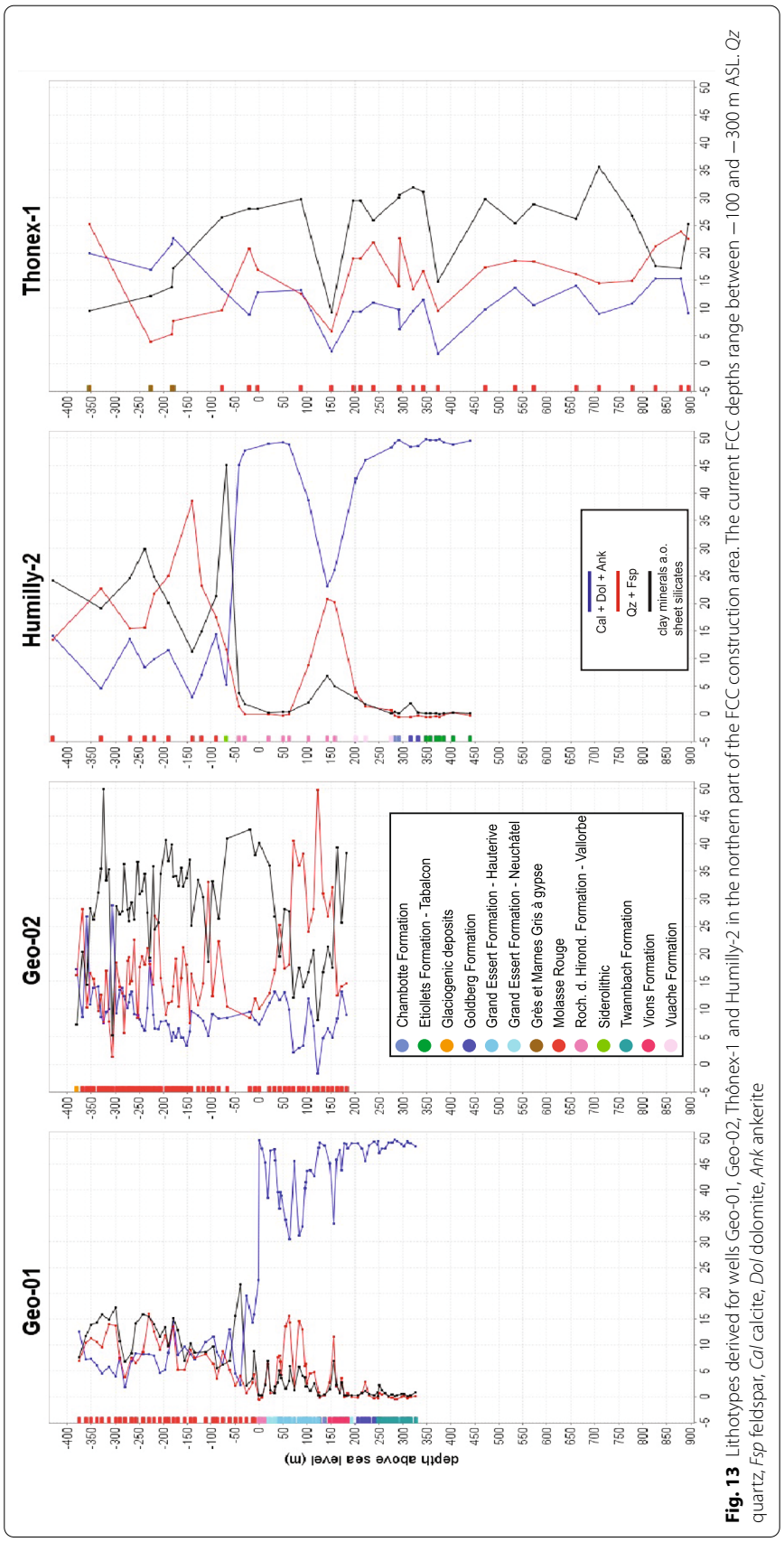

Fig. 13 Lithotypes derived for wells Geo-01, Geo-02, Thônex-1 and Humilly-2 in the northern part of the FCC construction area. The current FCC depths range between −100 and −300 m ASL. *Qz* quartz, *Fsp* feldspar, *Cal* calcite, *Dol* dolomite, *Ank* ankerite

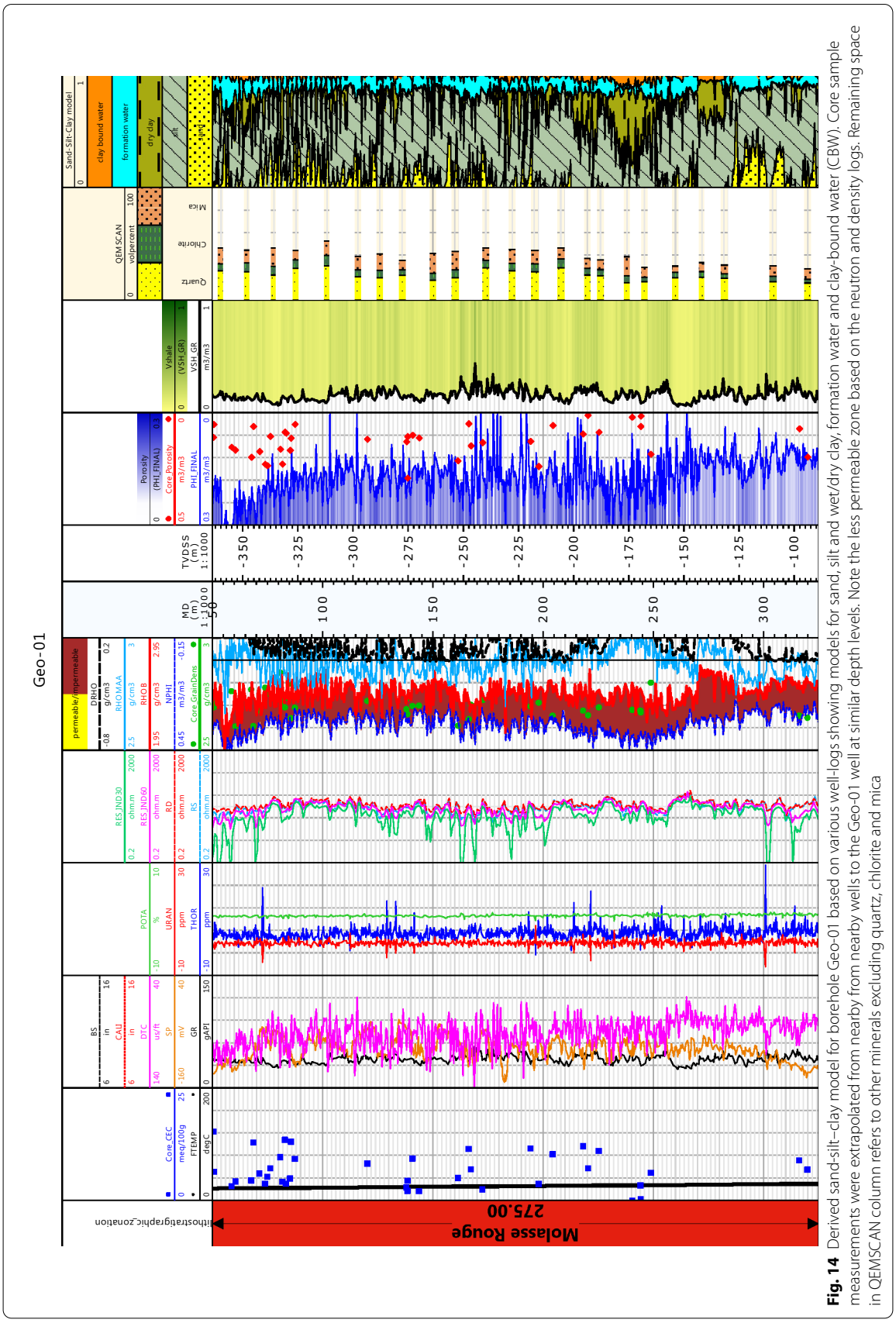

Fig. 14 Derived sand-silt–clay model for borehole Geo-01 based on various well-logs showing models for sand, silt and wet/dry clay, formation water and clay-bound water (CBW). Core sample measurements were extrapolated from nearby wells to the Geo-01 well at similar depth levels. Note the less permeable zone based on the neutron and density logs. Remaining space in QEMSCAN column refers to other minerals excluding quartz, chlorite and mica

Required inputs are neutron porosity, bulk density, true formation resistivity, flushed zone resistivity, formation temperature and water resistivity. The model is calculated based on available well-logs, petrophysical and geochemical laboratory data for well Geo-01 located in the northern part of the FCC construction area and shows high amounts of clay-bound water at depth intervals from 130 to 140 m ASL and 150 to 200 m ASL, together with a moderate amount of sand. Clay-bound-water decreases upwards towards ground level. Water content (formation water) remains constant from 375 to 80 m ASL but shows increased values between 70 and 20 m ASL, together with higher sand and reduced silt and clay content. The log solid rock volumes seem to correlate well with mineralogical analyses, also with respect to their volumes. This might suggest financial savings for upcoming FCC site investigations, as a first estimate of such a sand-silt–clay model and respective excavation volume estimates could be based on robust and proven well-logging analysis during site investigations prior to any laboratory analyses. QEMSCAN and sand-silt–clay model results follow similar trends in the Molasse Rouge: while QEMSCAN shows higher amounts of quartz, the model includes all (clean) minerals making up sandstone, i.e. quartz. The high amount of silt could be associated to the indication of impermeable intervals in the NPHI-RHOB plot, as well as V_{sh} log calculations depicting a similar trend. Based on the derivation of clay type (Fig. 15) for subsequent logging analysis, this confirms the applicability of a solid predictive approach based purely on well-logs, neglecting mineralogical analyses, and requiring CEC, core porosity and core grain density measurements, which have already successfully been measured and could be taken as proxies for future investigations. CEC measurements proved to be useful for the calculations of exchange cations per unit pore volume (Q_V). At present, lithotyping solely based on petrophysical analyses would suggest successful log calibration applied to compensate for the Molasse Rouge's heterogeneity and adequately define sandstone- and shale-bearing intervals. A clear distinction between the Molasse Rouge and Grès et Marnes Gris à gypse could not be established without explicit laboratory data since the difference of SP values by -20 mV reflects the error to be overcome by mineralogical analyses. The Molasse Rouge tends between dispersed and structural shale,

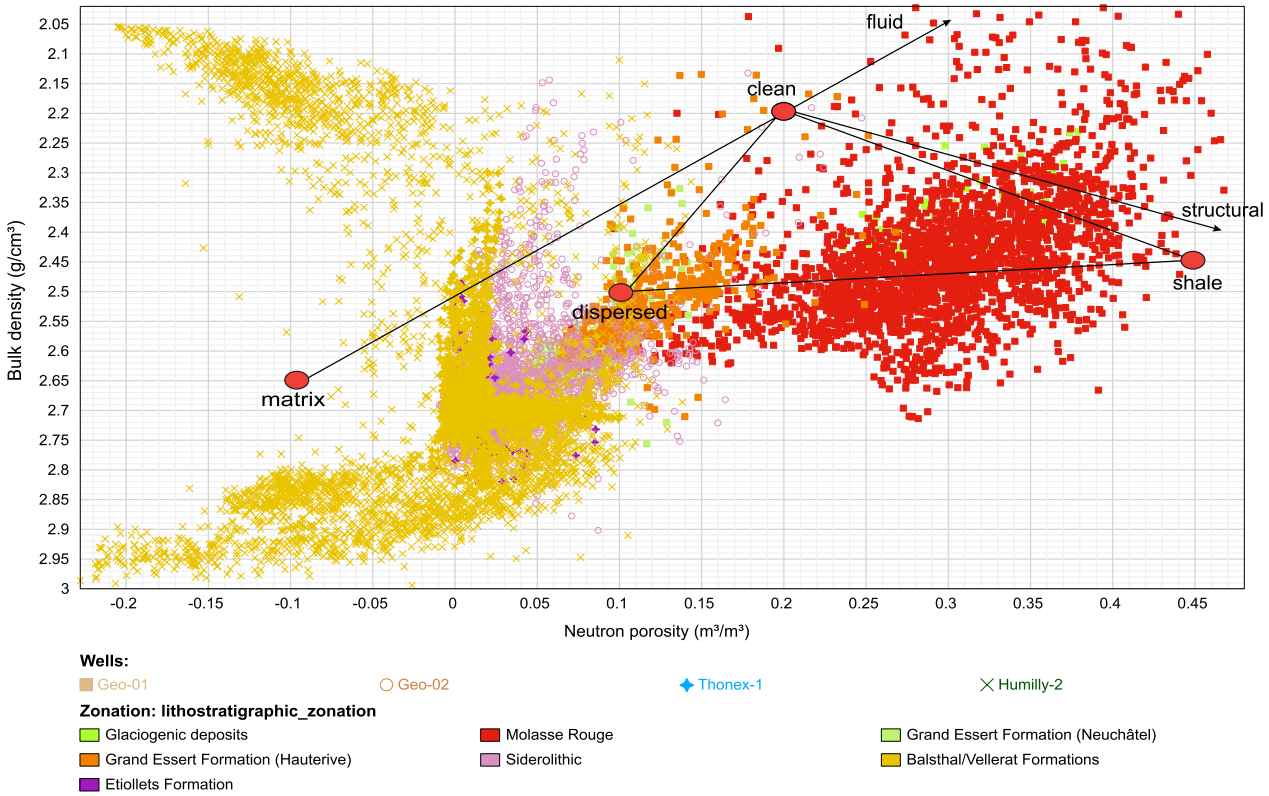

Fig. 15 Clay-type derivation using a Thomas-Stieber plot for 7 formations. A clear tendency towards dispersed shale is distinguished for the Hauterive Member of the Grand Essert Formation. Clay distribution for the Molasse Rouge ranges between the structural and dispersed types

with single samples showing clean zones. The Mesozoic clayey limestones show lesser content in clay.

5.4 Geological hazards

The FCC's geological hazards are stated in Table 2, which provides a list of ascertained occurrences of swelling rocks, hydrocarbon-bearing and karstified intervals, active faults, and water aquifers based on a lithostratigraphic subdivision of the subsurface. The identification of geological hazards is discussed below and would impact all subsequent project phases spanning over a period of over roughly ten years. As such, these factors would affect environmental impact assessment in the current feasibility phase, optimal well placement prior to site investigations in the technical design phase, and excavation progress during the construction phase.

5.4.1 Swelling rocks

When dry clay is subjected to water, swelling occurs in two phases based on a layer structure, charge and exchangeable cations of clay minerals, i.e. smectite (montmorillonite). The first phase describes intracrystalline swelling due to hydration of exchangeable cations, while the second phase, osmotic swelling, stems from the difference of ion concentrations at the clay mineral surface compared to a lower concentration in the pore water solution. These two types of clay swelling are reversible, whereas the irreversible third type refers to anhydrite swelling incorporating water by the formation of gypsum. Intra-crystalline and osmotic swelling cause a volume increase of up to 200% (Jasmund & Lagaly, 1993), while anhydrite swelling depicts volume increases up to 61% (Anagnostou, 2007; Steiner, 1993). In tunnelling, swelling is mostly associated with osmotic swelling, caused by the deconsolidation of clay minerals and their subsequent incorporation of water molecules.

The Grès et Marnes Gris à gypse contains a high amount of anhydrite/gypsum (Fig. 10), potentially leading to crystalline swelling. Note that QEMSCAN analyses chemical compositions, which do not allow a differentiation between anhydrite and gypsum. This fact favours XRD analysis, which allows to distinguish anhydrite and gypsum, and furthermore allows a quantitative approach and improved identification of fine-grained particles and clay mineral analysis. Based on clay minerals' chemical behaviour, gypsum occurs on

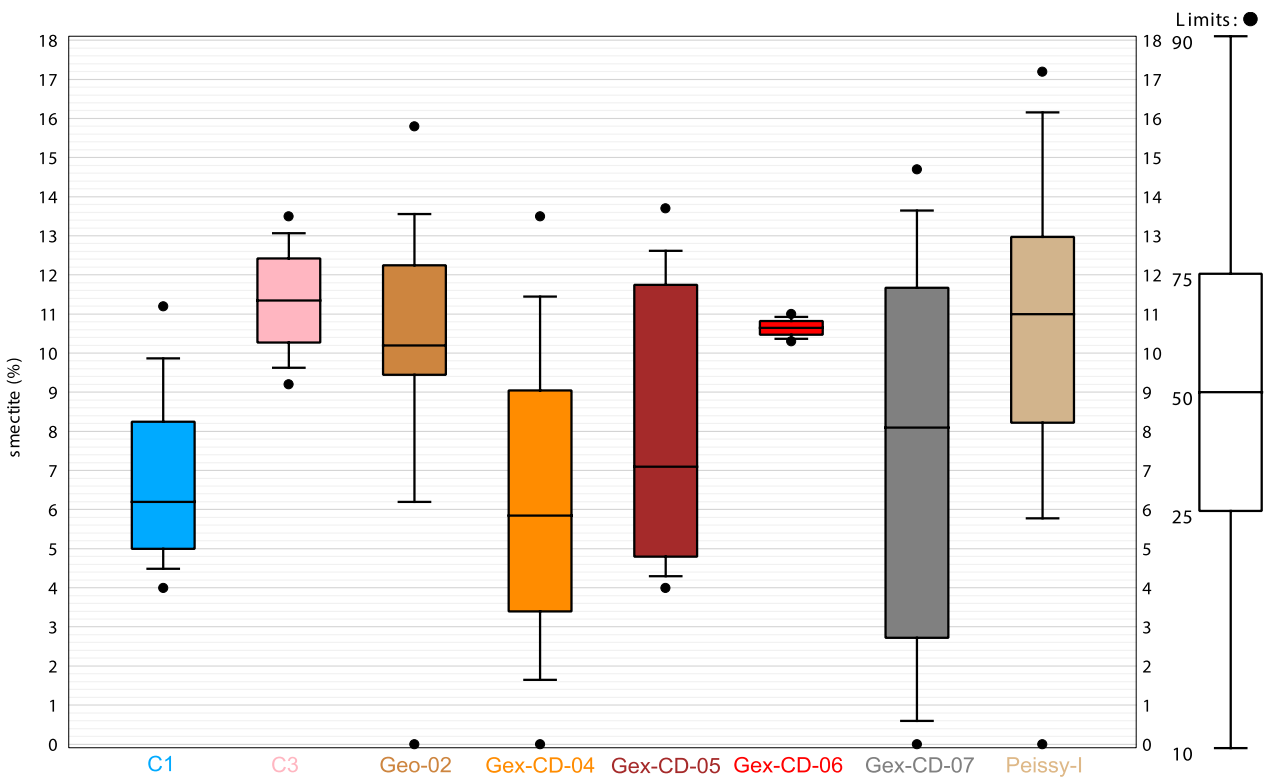

Fig. 16 Overview of swellable clay (smectite) from XRD measurements for 8 wells. The northern wells (Gex-CD-07 and Peissy-I) show a high variability, depicting maximum smectite values of 17.2%

surface while anhydrite is encountered in the subsurface (Wanninger-Huber, 2019). Anhydrite is encountered in the Savoie-104 well, and the Savoie wells as well as SPM2, SPM3 and SPM5 representing an anhydrite swelling hazard. The Balsthal/Vellerat formations might show a similar chemical composition as the Molasse Rouge for associated marl lithotypes, which bear swelling potential due to smectites, also encountered in the clayey limestone of the Etiollets Formation's Tabalcon Limestone sub-unit. The Molasse Rouge contains less anhydrite/gypsum but higher concentrations of smectite in clay, silty clay and clayey silt (Fig. 9) of up to 17.2% by volume (Fig. 16). With respect to anhydrite swelling, dedicated laboratory swelling tests are required for geotechnical design calculations of the FCC's tunnel infrastructure. Former research successfully used such swelling test results to numerically retrieve design value estimates of swelling pressures for final tunnel lining optimizations (Kovári & Vogelhuber, 2014).

Sandstone (S1–S6), mud- and siltstones (M1-M5) lithotypes show maximum Enslin-Neff water absorption of up to 58.9 wt.% (in Geo-02, Fig. 9) leading to swelling during construction. However, minimum Enslin-Neff water absorption values of 2.8 wt.% are represented by hydrophobic, hydrocarbon-bearing sandstone (HC). Detecting water absorption phenomena in geophysical well-logs is difficult, and only feasible in a qualitative manner via resistivity or neutron/density logs, potentially indicative of water/hydrocarbon-bearing rocks.

Log responses to detect swelling potential are related to (swellable) clay content in the SP log, which indicates slightly lower values in the Grès et Marnes Gris à gypse formation compared to the Molasse Rouge. This is most likely related to higher contents of anhydrite/gypsum in the Grès et Marnes Gris à gypse formation, as also measured by QEMSCAN, subjecting the type of voltage difference to the SP's membrane potential in the Molasse Rouge due to higher occurrences of clay, rather than the liquid junction potential. However, while logs might indicate qualitatively the hazard of swelling, mineralogical analyses remain crucial for its quantification. Both the Molasse Rouge and Grès et Marnes Gris à gypse formations bear a hazard for all three types of swelling.

5.4.2 Bituminous and gaseous hydrocarbons

An extensive overview of environmental thresholds for heavy-metal ions and hydrocarbons for usage and disposal of excavated rock has been reported in Haas et al. (2020a) and (b)). While these results are to be presented in a future study, the lateral and vertical distribution of hydrocarbons are discussed from a stratigraphic point of view along the two cross sections (Figs. 5, 6).

Substantial amounts of hydrocarbons are detected in the massive dolostones in the Goldberg and Twannbach formations and are encountered in all wells featuring these two formations. The Vions Formation shows indices of hydrocarbons, as shared with the Grand Essert Formation's Neuchâtel Member. Although hydrocarbons occur predominantly as bitumen, well Geo-01-DAS located about 300 m next to the deeper Geo-01 well, shows the presence of gaseous hydrocarbons in the Molasse Rouge. This suggests that gas-bearing (hydrocarbon) horizons are likely to be encountered in the northern part of the construction area and should be addressed during site investigations. Cretaceous carbonates show indications of heavier oil and asphalt if they are fractured. With respect to their total well depths, the Gex-CD-01 and its neighbouring Gex-CD-07 well show the highest hydrocarbon indices in medium to coarse-grained sandstones in the Molasse Rouge (HC lithotype, Fig. 4) and in Mesozoic limestone formations (Fig. 5). For cross section B, all wells show indices of hydrocarbons (bitumen) with larger amounts in the Geo-01, Geo-02, and Salève-2 wells (Fig. 6). No traces of gas were observed in the cored intervals of the Gex wells. This suggests local gas accumulations rather than laterally extensive gas horizons and complies with minor industrial hydrocarbon exploration success across the basin in the past. In some rare occurrences (e.g. well L134B), the Quaternary deposits also contain bituminous hydrocarbons.

An increasing trend of large amounts of accumulated hydrocarbons is interpreted from south to north across the basin since the northern wells (Gex-CD-01, Gex-CD-07, Peissy-I, SLHC-wells, C-wells) contain most of the hydrocarbons within the studied area. An exception is marked by the Thônex-1 well, which, in the same area, crosses large amounts of the Grès et Marnes Gris à gypse formation. However, the Grès et Marnes Gris à gypse does not explicitly exclude hydrocarbon occurrences. Apart from the Molasse Rouge, deeper carbonate formations in the former *Urgonien* facies (Lower Cretaceous), Muschelkalk (Middle Triassic) and Buntsandstein sandstone (Lower Triassic) also show hydrocarbon indices in wells Chatillon-1 and Charmont-1, close to the Jura in the northwestern sector of the FCC's construction area. While these units are not primarily ranging within the projected FCC construction depths, adjacent faults might represent potential migration pathways for hydrocarbons toward the FCC depth intervals.

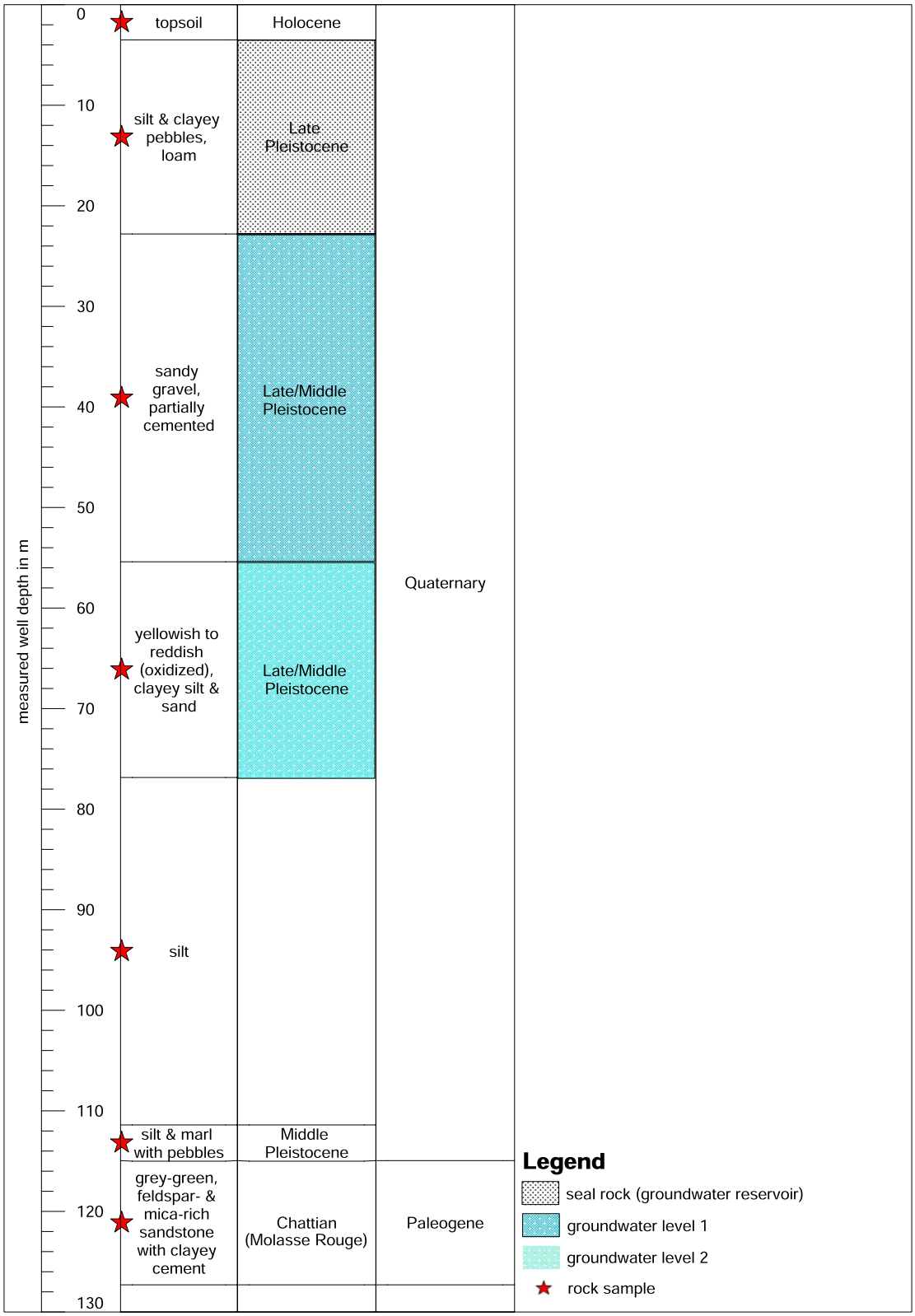

Fig. 17 Well Montfleury-2 located in an anticline structure, showing Pleistocene deposits confined within a topographic valley. Respective rock samples are shown in Fig. 7

5.4.3 Karstified intervals

Karst created a significant litho-technical hazard during LEP subsurface construction in the 1970's, substantiated in documentation from SPM wells. Reports of Salève wells document rapid loss of mud circulation into fractured limestones, which finally caused a forced well closure (Conrad & Ducloz, 1977; Géotechnique Appliquée Dériaz & SA (GADZ), 1981b, 1982b). This leads to the assumption that karst formations are not restricted to the northern FCC construction area but could be encountered also in fractured limestone formations in the south. Both the Chambotte Formation and Transition zone imply karstic occurrences, not necessarily excluding characteristics like those encountered in the porous Siderolithic Formation (Fig. 8). The Twannbach Formation, the Roches des Hirondelles Formation's Vallorbe Member, the Vions Formation and the Grand Essert Formation's Neuchâtel Member represent a substantial hazard for karst, extending across several tens of meters vertically. Since the FCC's current layout runs at several depth intervals through the Transition zone, geophysical seismic surveys should be conducted targeting these formation.

5.4.4 Fault structures and water aquifers

The FCC's current footprint crosses several active faults, synclines and anticlines, which bear a certain geological hazard of inducing an active stress regime around the tunnel perimeter during construction. This goes along with hydrocarbon migration paths along fault and fracture networks, which could lead to environmental contamination. The identification of faults and associated hydrocarbon migration paths should be investigated by future (3D) seismic surveys. One of the main active faults is represented by the sinistral strike-slip Vuache Fault in the southwestern corner of the FCC's planned construction area (Fig. 1). Another offset in geological formations is shown by the Subalpine Thrust, which per se is not active but indicates a displacement in the spatial arrangement of encountered formations. The syn- and anticline structures observed in the northern part of the proposed FCC perimeter do not reflect an active fault scenario. However, their geological trend is suggested to be studied with more accuracy, since it would allow better prediction of the Grès et Marnes Gris à gypse lateral and vertical distribution, a formation prone to swelling, as well as the distribution of unconsolidated glaciogenic deposits that are captured in between syn- and anticlines and that presently host important groundwater reservoirs. The large erosional valleys located at the Valley of Aire and at Petit Lac in the northern part of the FCC area are filled with unconsolidated, clayey sediments, usually referred to as mudstone of postglacial origin (Fiore et al., 2002; Moscariello et al., 1998), and would pose a substantial hazard for the FCC shaft construction due to affected groundwater aquifers (Fig. 17). The Quaternary deposits represent one of the main water reservoirs in the Geneva Basin towards the northern part of the FCC construction, in close vicinity to syncline and anticline structures. Above these deposits, impermeable Late Pleistocene sediments seal the water reservoirs.

6 Conclusions

This study aims to provide the basis for a vast set of engineering and environmental undertakings as part of the Future Circular Collider project commissioned by the European Organization for Nuclear Research (CERN) in the Geneva Basin across the Swiss-French border. The objectives were to identify the geological formations in the subsurface of the Geneva Basin and link them to the geo-engineering construction of the FCC to address geological hazards and encountered lithotypes. A multidisciplinary approach was chosen by carrying out petrophysical, mineralogical and geochemical laboratory analyses from available rock cores in conjunction with digitized geophysical well-log analyses.

The geographically defined Geneva Basin consists in chronostratigraphic order of Holocene topsoil, Quaternary post-glacial deposits and LGM moraines, inter-gacial and pre-glacial sediments, which overlie the Oligocene Molasse Rouge and Grés et Marnes Gris à gypse (LFM) followed by the Eocene(?) Siderolithic Formation. The Transition zone (Perte-du-Rhône Formation?) marks the currently researched Cenozoic-Mesozoic stratigraphic boundary, before encountering the Jura units represented by the Cretaceous Vallorbe Formation, the Hauterive and Neuchâtel Members of the Grand Essert Formation and the Gorges de l'Orbe Formation (former *Urgonien*, Early Cretaceous) as well as the Vuache, Chambotte, Vions, Pierre-Châtel and Goldberg formations. The Twannbach, Etiollets and currently debated Balsthal and Vellerat formations complete the Jurassic units of the Jura. The FCC' stratigraphic evaluation revealed 13 geological formations excluding the Goldberg, Chambotte, Pierre-Châtel and Twannbach formations as well as the Etiollet Formation's Tabalcon Limestone sub-unit, the Blanc Limestone, Balsthal and Vellerat formations, and comprises 25 different lithotypes. A distinct lack of data remains in the western to south-western subsurface portions of the FCC's proposed construction area.

Associated geological hazards include karstic intervals in the Grand Essert Formation's Neuchâtel Member, Roches des Hirondelles Vallorbe Member and Vuache Formation associated to fractured limestone lithotypes, and Cenozoic formations represented by

the clayey sandstone-bearing Transition zone and Siderolithic Formation. The Molasse Rouge and Grès et Marnes Gris à gypse formations show presence of hydrocarbons and swelling potential due to smectite and anhydrite/gypsum occurrences, making these formations the most crucial ones for prevention of possible tunnelling issues. Hydrocarbon occurrences bear an environmental hazard encountered across all wells, mostly in the Molasse Rouge and Mesozoic formations, predominantly associated with fractured limestone. The Molasse Rouge was described and identified in north–south cross sections and divided into an upper sandstone-dominated and a lower clayey limestone succession, both of Chattian age. Encountered hydrocarbons are associated prevalently with the sandstone succession. The adopted interdisciplinary approach allowed to ascertain a set of geological hazards that may influence the projected engineering undertakings and environmental impact assessment for the FCC's final layout and subsequent technical design phase. The findings stipulate a robust predictive approach for large-scale subsurface construction and lithotyping, aimed at establishing a knowledge base for potential application scenarios of excavated material and engineering rock classifications. Moreover, future studies should also involve the careful investigation of rock mechanics data to derive geotechnical design calculations for the FCC's tunnel infrastructure.

Acknowledgements
The authors would like to thank the *Swiss Federal Office of Topography (Swisstopo)*, namely Dr. Peter Hayoz, for the permission of inspecting the core material at the Swiss core facility in Hochdorf (Switzerland). Company *TOTALEnergies* and its associated core facility service *STC (Carothèque)* represented by Gilles Graffin are kindly thanked for providing the well cores and enabling us to perform the rock core inspections under very welcoming conditions in Boussens (France). The *Services Industriels de Genève (SIG)* is sincerely thanked for the provision of geophysical well-logs for boreholes Geo-01 and Geo-02. Pieter Mattelaer and Jérémy Voiron are thanked for their administrative permissions to investigate the well cores stored at *CERN's HL-LHC Point 1* site. Anticipated gratitude is indebted to Dr. Michael Benedikt (CERN) for granting financial support on behalf of the FCC study to travel to respective core facilities. Finally, the first author would like to thank Ross Crain, PEng. for his valuable input. The results presented herein are part of the first author's PhD thesis conducted within the scope of the FCC study at CERN, Montanuniversität Leoben, ETH Zurich and the University of Geneva.

Authors' contributions
MH set up the concept together with AM, performed the data digitisation, rock core inspections and descriptions in the field, all laboratory analyses, corresponding data analysis (except for XRD and QEMSCAN raw data analysis) and full data interpretation, modelling, petrophysical calculations, all visualizations (except for the redrawn stratigraphic log of well Gex-CD-01), writing of the original draft as well as reviewing and editing of the manuscript. DC drew the stratigraphic log of Gex-CD-01. DV supervised the first author in editing the manuscript. MP performed the XRD raw data analysis, supervised the first author in the laboratory analyses performed at ETH Zurich (XRD, CEC, Enslin-Neff, ICP-OES), as well as reviewed and validated the manuscript. ADH performed the QEMSCAN raw data analysis, supervised the first author in QEMSCAN interpretation and validated the manuscript. AM set up the concept together with MH, supervised during the stratigraphical, sedimentological and porosity-permeability interpretation as well as validated the manuscript.

Funding
This study has received funding from the European Union's Horizon 2020 research and innovation programme under grant agreement No. 951754.

Availability of data and materials
The datasets generated and/or analysed during the current study are available in the supplementary material. Geophysical well-log data are available from the corresponding author upon request, but certain third-party restrictions apply (SIG, GESDEC, CERN, UNIGE). The resulting Techlog (Schlumberger software) file used for well-log analysis is also available upon request of the corresponding author. The data have been partly published on the ZENODO platform (www.zenodo.org) under DOI's https://doi.org/10.5281/zenodo.4725585, https://doi.org/10.5281/zenodo.4725517 and https://doi.org/10.5281/zenodo.4725558.

Declarations

Ethics approval and consent to participate
Not applicable. No inclusion of human participants, human data or human tissue.

Consent for publication
The manuscript does not contain any individual person's data in any form.

Competing interests
The authors declare that they have no competing interests.

Author details
[1]European Organization for Nuclear Research (CERN), Espl. Des Particules 1, 1211 Geneva, Switzerland. [2]Subsurface Engineering, Montanuniversität Leoben, Erzherzog-Johann-Strasse 3, 8700 Leoben, Austria. [3]Geo-Energy Reservoir Geology and Sedimentary Basin Analysis, Université de Genève, Rue des Maraîchers 13, 1205 Geneva, Switzerland. [4]Institute for Geotechnical Engineering (ClayLab), ETH Zurich, Stefano-Franscini-Platz 3, 8093 Zurich, Switzerland.

Received: 27 October 2021 Accepted: 19 January 2022
Published online: 03 May 2022

References

Abada, A., Abbrescia, M., AbdusSalam, S. S., Abdyukhanov, I., et al. (2019). FCC-ee: The lepton collider. *The European Physical Journal Special Topics, 228*, 261–623. https://doi.org/10.1140/epjst/e2019-900045-4

Abreu, V., & Anderson, J. (1998). Glacial eustasy during the Cenozoic: Sequence stratigraphic implications. *American Association of Petroleum Geologists Bulletin, 82*, 1385–1400. https://doi.org/10.1306/1D9BCA89-172D-11D7-8645000102C1865D

Alija, S., Torrijo, F. J., & Quinta-Ferreira, M. (2013). Geological engineering problems associated with tunnel construction in karst rock masses: The case of Gavarres tunnel (Spain). *Engineering Geology, 157*, 103–111. https://doi.org/10.1016/j.enggeo.2013.02.010

Allen, P. A., Crampton, S. L., & Sinclair, H. D. (1991). The inception and early evolution of the North Alpine Foreland Basin, Switzerland. *Basin Research., 3*, 143–163. https://doi.org/10.1111/j.1365-2117.1991.tb00124.x

Alonso, E., Olivella, S. (2008). Modelling tunnel performance in expansive gypsum claystone. In: The 12th international conference of international association for computer methods and advances in geomechanics, 2.

Amir, K., Philippe, S., Philippe-Hervé, L., Vincenzo, S., Bastien, H., Albert, G., Jean-Loup, R., & Bernard, P. (2020). Changes in hydrodynamic process dominance (wave, tide or river) in foreland sequences: The subalpine Miocene Molasse revisited (France). *Sedimentology, 67*, 2455–2501. https://doi.org/10.1111/sed.12708

Anagnostou, G. (1993). A model for swelling rock in tunnelling. *Rock Mechanics and Rock Engineering, 26*, 307–331. https://doi.org/10.1007/BF01027115

Anagnostou, G. (2007). Design uncertainties in tunnelling through anhydritic swelling rocks. *Felsbau, 25*, 48–54.

Anagnostou, G., Pimentel, E., & Serafeimidis, K. (2010). Swelling of sulphatic claystones—some fundamental questions and their practical relevance /. Quellen von sulfatführenden Tonsteinen—Themen der Grundlagenforschung und ihre praktische Bedeutung. *Geomech. Tunn., 3*, 567–572. https://doi.org/10.1002/geot.201000033

Arn, R. (1984). Contribution à l'étude stratigraphique du Pléistocène de la région lémanique. University of Lausanne.

Asquith, G., Krygowski, D., Henderson, S., & Hurley, N. (2004). Basic well log analysis. *American Association of Petroleum Geologists*. https://doi.org/10.1306/Mth16823

Bachmann, G.H., Müller, M. (1991). The Molasse Basin, Germany: evolution of a classic petroliferous foreland basin. In: Spencer (AM) (Ed.). University Press, Oxford, pp. 263–276

Bachmann, G. H., & Müller, M. (1992). Sedimentary and structural evolution of the German Molasse Basin. *Eclogae Geologicae Helvetiae, 85*, 519–530.

Bachmann, G. H., Dohr, G., & Muller, M. (1982). Exploration in a classic thrust belt and its foreland: Bavarian Alps, Germany. *American association of Petroleum Geologists Bulletin., 66*, 2529–2542. https://doi.org/10.1306/03b5ac69-16d1-11d7-8645000102c1865d

Bartenstein, H. (1978). Erdolvorkommen im Molassebecken. Erdol und Kohle—Erdgas Petrochemie Ver. mit Brennstoff-Chemie.

Becker, A. (2000). The Jura Mountains—an active foreland fold-and-thrust belt? *Tectonophysics*. https://doi.org/10.1016/S0040-1951(00)00089-5

Benedikt, M., Blondel, A., Janot, P., Mangano, M., & Zimmermann, F. (2020). Future Circular Colliders succeeding the LHC. *Nature Physics, 16*, 402–407. https://doi.org/10.1038/s41567-020-0856-2

Berdugo, I., Alonso, E., Romero, E., & Gens, A. (2009). Tunnelling and swelling in Triassic sulphate-bearing rocks. Part II-case studies from Jura Mountains. *Épsilon, 12*, 39–53.

Berger, J.-P. (1996). Cartes paléogéographiques-palinspastiques du bassin molassique suisse (Oligocène inférieur–Miocène moyen). *Neues Jahrbuch Fuer Geologie Und Palaeontologie, Abhandlungen, 202*, 1–44.

Blondel, T. (1984). Étude téctonique de la partie septentrionale de la montagne du Vuache (Haute-Savoie, France).

Brenchley, P.J. (1992). A geologic time scale 1989, Geological Journal. John Wiley & Sons Ltd. Doi: https://doi.org/10.1002/gj.3350270220

Brentini, M., 2018. Impact d'une donnee geologique heterogene dans la gestion des geo-ressources: analyse integree et valorisation de la stratigraphie a travers le bassin genevois (Suisse, France). Université de Genève. https://doi.org/10.13097/archive-ouverte/unige:103409

Brindley, G. W., & Brown, G. (1980). *Crystal structures of clay minerals and their X-ray identification*. Mineralogical Society of Great Britain and Ireland. https://doi.org/10.1180/mono-5.

Brink, H. J., Burri, P., Lunde, A., & Winhard, H. (1992). Hydrocarbon habitat and potential of Swiss and German Molasse Basin: a comparison. *Eclogae Geologicae Helvetiae, 85*(3), 715–732.

Burdin, J., Monin, N., Thalmann, C. (2017). L'utilisation des matériaux extraits des ouvrages souterrains, Entreprend. ed. DOSSIER—MATEX.

Burkhard, M. (1990). Aspects of the large-scale Miocene deformation in the most external part of the Swiss Alps (Subalpine Molasse to Jura fold belt). *Eclogae Geol* (pp. 559–583). Helv. Birkhäuser Verlag.

Burkhard, M., & Sommaruga, A. (1998). Evolution of the western Swiss Molasse basin: structural relations with the Alps and the Jura belt. *Geological Society, London, Special Publications, 134*(1), 279–298. https://doi.org/10.1144/GSL.SP.1998.134.01.13

Burri, M. (1981). Les terrasses lémaniques: Géologie. *Arch. Sui. Anthr. Gén., 45*, 107–115.

Butscher, C., Huggenberger, P., & Zechner, E. (2011). Impact of tunneling on regional groundwater flow and implications for swelling of clay–sulfate rocks. *Engineering Geology., 117*, 198–206. https://doi.org/10.1016/j.enggeo.2010.10.018

Buxtorf, A. (1916). Prognosen und Befunde beim Hauensteinbasis- und Grenchenbergtunnel und die Bedeutung der Letzteren für die Geologie des Juragebirges. *Verhandlungen. Naturforschende Gesellschaft (basel), 27*, 185–254.

Cederbom, C., Sinclair, H. D., Schlunegger, F., & Rahn, M. K. (2004). Climate-induced rebound and exhumation of the European Alpls. *Geology, 32*, 709–712.

Cederbom, C., Schlunegger, F., Sinclair, H.D., van der Beek, P. (2008). Late Neogene climatic, tectonic and geodynamic(?) forcing on the European Alps recorded by the erosion history of the North Alpine Foreland Basin. Geophys. Res. Abstr. 10, EGU2008-A-01147.

Chablais, J., Moscariello, A. (2012). Coretest Systems Inc., AP-608 Automated Permeameter-Porosimeter, Operator's Quick Manual. GE-RGBA Report 2012001. University of Geneva.

Chablais, J., Rusillon, E. (2018). Fiche Forage—GEo-01.

Chablais, J., Savoy, L. (2019). GEo-02 (SIG)—Litholog de forage—Litholog (LLR).

Charollais, J., Weidmann, M., Berger, J.-P., Engesser, B., Hotellier, J.-F., Gorin, G., Reichenbacher, B., & Schäfer, P. (2007). La Molasse du bassin franco-genevois et son substratum. *Archives Des Sciences., 60*, 59–174.

Charollais, J., Wernli, R., Mastrangelo, B., Metzger, J., Busnardo, R., Clavel, B., Conrad, M., Davaud, E., Granier, B., Martin, M. S., & Weipmann, M. (2013). Présentation d'une nouvelle carte géologique du Vuache et du Mont de Musièges (Haute-Savoie, France) stratigraphie et tectonique. *Archives Des Sciences., 66*, 1–63.

Chelle-Michou, C., Do Couto, D., Moscariello, A., Renard, P., & Rusillon, E. (2017). Geothermal state of the deep Western Alpine Molasse Basin, France-Switzerland. *Geothermics, 67*, 48–65. https://doi.org/10.1016/j.geothermics.2017.01.004

Clerc, N., & Moscariello, A. (2020). A revised structural framework for the Geneva Basin and the neighboring France region as revealed from 2D seismic data: implications for geothermal exploration. *Swiss Bull. Appl. Geol., 25*, 109–131.

Clerc, N., Rusillon, E., Moscariello, A., Renard, P., Paolacci, S., & Meyer, M. (2015). Detailed Structural and reservoir rock typing characterisation of the greater Geneva Basin, Switzerland, for Geothermal Resource Assessment, World Geothermal Congress 2015. *Melbourne, Australia*. https://doi.org/10.1002/2017EF000724

Cohen, K., Finney, S., Gibbard, P., & Fan, J. (2013). The ICS International Chronostratigraphic Chart. *Episodes, 36*, 199–204. https://doi.org/10.18814/epiiugs/2013/v36i3/002

Conrad, M.-A., Ducloz, C. (1977). Nouvelles observations sur l'Urgonien et le Sidérolithique du Salève. Eclogae Geol. Helv. 70.

Courboulex, F., Deichmann, N., & Gariel, J. C. (1999). Rupture complexity of a moderate intraplate earthquake in the Alps: The 1996 M5 Epagny-Annecy earthquake. *Geophysical Journal International*. https://doi.org/10.1046/j.1365-246X.1999.00931.x

Coretest Systems Inc. (2008). Coretest Systems Inc., Grain volume measurement system, operator's manual, supplement to operator's manual for AP-608 automated permeameter-porosimeter.

Coretest Systems Inc. (2011). AP-608 Automated Permeameter-Porosimeter, Operator's Manual, V6g1.

Crain, E.R. (2021). Crain's Petrophysical Handbook [WWW Document]. URL https://spec2000.net/ (accessed 5.26.21).

Darling, T. (2005). Well logging and formation evaluation. *First Edit. Ed. Gulf Professional Publishing*. https://doi.org/10.1016/B978-0-7506-7883-4.X5000-1

Deutsches Institut für Normung (DIN) (2012). Soil, testing procedures and testing equipment—Determination of water absorption—DIN 18132.

Deville, E., Blanc, E., Tardy, M., Beck, C., Cousin, M., & Ménard, G. (1994). Thrust propagation and syntectonic sedimentation in the Savoy Tertiary Molasse Basin (Alpine foreland). In Hydrocarbon and petroleum geology of France (pp. 269-280). Doi: https://doi.org/10.1007/978-3-642-78849-9_19

Diem, B. (1986). Die Untere Meeresmolasse zwischen der Saane (Westschweiz) und der Ammer (Oberbayern). Universität Bern.

Do Couto, D., Garel, S., Moscariello, A., Bou Daher, S., Littke, R., & Weniger, P. (2021). Origins of hydrocarbons in the Geneva Basin: Insights from oil, gas and source rock organic geochemistry. *Swiss Journal of Geosciences*. https://doi.org/10.1186/s00015-021-00388-4

Doebelin, N., & Kleeberg, R. (2015). Profex: A graphical user interface for the Rietveld refinement program BGMN. *Journal of Applied Crystallography, 48*, 1573–1580. https://doi.org/10.1107/S1600576715014685

Donzeau, M., Wernli, R., Charollais, J., Monjuvent, G. (1997). Saint-Julien-en-Genevois Carte géologique de la France au 1:50 000, feuille 653 et notice explicative. BRGM, Orléans.

Doppler, G. (1989). Zur Stratigraphie der nördlichen Vorlandmolasse in Bayrisch-Schwaben. *Geol. Bavarica, 94*, 83–133.

Doumer, P., British Petrol (France) (1983a). Societé Française des Pétroles BP - Rapport 16.1219 de fin de sondages: Gex-CD-07 (géologie).

Doumer, P., British Petrol (France) (1983b). Societé Française des Pétroles BP - Rapport 16.1216 de fin de sondages: Gex-CD-04 (géologie).
Doumer, P., British Petrol (France) (1983c). Societé Française des Pétroles BP—Rapport 16.1214 de fin de sondages: Gex-CD-02 (géologie).
Doumer, P., British Petrol (France) (1983d). Societé Française des Pétroles BP—Rapport 16.1217 de fin de sondages: Gex-CD-05 (géologie).
Doumer, P., British Petrol (France) (1983e). Societé Française des Pétroles BP—Rapport 16.1218 de fin de sondages: Gex-CD-06 (géologie).
Doumer, P., British Petrol (France) (1983f). Societé Française des Pétroles BP—Rapport 16.1215 de fin de sondages: Gex-CD-03 (géologie).
Doumer, P., (France), B.P., 1983. Societé Française des Pétroles BP - Rapport 16.1213 de fin de sondages: Gex-CD-01 (géologie).
Dunkl, I., & Demény, A. (1997). Exhumation of the Rechnitz Window at the border of the Eastern Alps and the Pannonian basin during Neogene extension. *Tectonophysics, 272*, 197–211.
Dupuis, D. (2009). Etude des sediments quaternaires, de la Molasse et sa tectonique, dans le Grand Lac (Leman) a partir de donnees sismiques 2D et 3D. Université de Genève.
Ehrbar, H. (2008). Gotthard-Base-Tunnel—Experiences with different tunnelling methods, in: 2° Congresso Brasileiro de Túneis e Estruturas Subterrâneas Seminário Internacional "South American Tunnelling"—2008Estruturas Subterrâneas Seminário Internacional "South American Tunnelling"—2008.
Einfalt, H.-C., Fecker, E., Götz, H.-P. (1979). Das Dreiphasensystem Ton, Anhydrit, Gips und dessen zeitabhängiges Verhalten bei Zugabe von wässrigen Lösungen, in: 4. Internationaler Felsmechanik-Kongress, Montreux.
Einstein, H. H. (1996). Tunnelling in difficult ground - Swelling behaviour and identification of swelling rocks. *Rock Mechanics and Rock Engineering, 29*, 113–124. https://doi.org/10.1007/BF01032649
Ellis, D. V., & Singer, J. M. (2007). *Well logging for earth scientists* (2nd ed.). Springer. https://doi.org/10.1007/978-1-4020-4602-5
Erdős, Z., Huismans, R. S., & van der Beek, P. (2019). Control of increased sedimentation on orogenic fold-and-thrust belt structure – insights into the evolution of the Western Alps. *Solid Earth*, *10*, 391–404. https://doi.org/10.5194/se-10-391-2019.
European Norm (EN) (2003). Non-destructive testing - X-ray diffraction from polycristalline and amorphous material—Part 2: Procedures; German version EN 13925-2:2003
Fachgruppe für Untertagebau (FGU) (2016). Bewirtschaftung und Wiederverwertung von Ausbruchmaterial—Inventar Schweizer Großprojekte. Fachgruppe für Untertagebau, Esslingen.
Fern, E. J., Di Murro, V., Soga, K., Li, Z., Scibile, L., & Osborne, J. A. (2018). Geotechnical characterisation of a weak sedimentary rock mass at CERN, Geneva. *Tunnelling and Underground Space Technology., 77*, 249–260. https://doi.org/10.1016/J.TUST.2018.04.003
Fiore, J. (2007). Quaternary subglacial processes in Switzerland: Geomorphology of the Plateau and seismic stratigraphy of Western Lake Geneva. University of Geneva.
Fiore, J., Pugin, A., & Beres, M. (2002). Sedimentological and GPR studies of subglacial deposits in the Joux Valley (Vaud, Switzerland): backset accretion in an esker followed by an erosive jökulhlaup. *Géographie Physique Et Quaternaire., 56*, 19. https://doi.org/10.7202/008602ar
Forchheimer, P. (1901). Wasserbewegung durch Boden. *Zeitschrift Des Vereins Dtsch. Ingenieure, 45*, 1731.
Frisch, W., Kuhlemann, J., Dunkl, I., & Brügel, A. (1998). Palinspastic reconstruction and topographic evolution of the Eastern Alps during late Tertiary tectonic extrusion. *Tectonophysics*. https://doi.org/10.1016/S0040-1951(98)00160-7
Füchtbauer, H. (1959). Die Schüttungen im Chatt und Aquitan der deutschen Alpenvorlandsmolasse. *Eclogae Geologicae Helvetiae, 73*, 173–203.
Fuller, C. W., Willett, S. D., & Brandon, M. T. (2006). Formation of forearc basins and their influence on subduction zone earthquakes. *Geology*. https://doi.org/10.1130/G21828.1
Géotechnique Appliquée Dériaz & SA (GADZ) (1981a). Obturation des forages L133, L134, L134 BIS.
Géotechnique Appliquée Dériaz & SA (GADZ) (1981b). Sondage SPM1; Sondage SPM2 (includes SPM3 et SPM4); Sondages SPL 2.1 et 2.2; Sondage SPM5.
Géotechnique Appliquée Dériaz & SA (GADZ) (1982b). Sondage SPL7.2; Sondage SPL8.1; Sondage SPL8.2; Sondage SPL8.7; Sondages SPL8.5 et 8.8, Sondages SPL8.9 et 8.13; Sondages SPL 8.10 et 8.12; Sondages SPL 8.14 et 8.15; Sondage SPM11; Sondage SPM15; Sondage SPM16.
Géotechnique Appliquée Dériaz & SA (GADZ) (1982a). Sondage L135.
Géotechnique Appliquée Dériaz & SA (GADZ) (1992). Sondage de reconnaisance SPL1.02.
Géotechnique Appliquée Dériaz & SA (GADZ) (1993a). Projet LHC—Synthèse géologique et géotechnique—Rapport CERN-division-ST 3545/5. Geneva.
Géotechnique Appliquée Dériaz & SA (GADZ) (1993b). Projet LHC (SLHC12).
Géotechnique Appliquée Dériaz & SA (GADZ) (1996a). Projet LHC—LOT 1 (SLHC 20, SLHC 21, SLHC 22, SLHC 23, SLHC 24, SLHC 25).
Géotechnique Appliquée Dériaz & SA (GADZ) (1996b). Projet LHC—LOT 3 (SLHC10, SLHC11, SLHC 42, SLHC 43, SLHC 44, SLHC 49, SLHC 50).
Géotechnique Appliquée Dériaz & SA (GADZ) (1997). Statistique molasse (globale)—marnes standards, marnes alterées, marnes gruméleuses, marnes gréseuses, grès tendres, grés durs, grès très durs et marno-calcaires—synthése LHC 1995–1997 (annexe 4g).
Géotechnique Appliquée Dériaz & SA (GADZ) (2015a). High Luminosity LHC Point 1 - Sondage C2, 7222.102.
Géotechnique Appliquée Dériaz & SA (GADZ) (2015b). High Luminosity LHC Point 1 - Sondage C4, 7222.104.
Géotechnique Appliquée Dériaz & SA (GADZ) (2015c). High Luminosity LHC Point 1—Sondage C1, 7222.101.
Géotechnique Appliquée Dériaz & SA (GADZ) (2015d). High Luminosity LHC Point 1—Sondage C3, 7222.103.
Géotechnique Appliquée Dériaz & SA (GADZ) (2016a). High Luminosity LHC Point 1—Sondage C6, 7222.106.
Géotechnique Appliquée Dériaz & SA (GADZ) (2016b). High Luminosity LHC Point 1—Sondage C7, 7222.107.
Géotechnique Appliquée Dériaz & SA (GADZ) (2016c). High Luminosity LHC Point 1—Sondage C5, 7222.105.
Etat de Genève (1994). Forage géothermique de Thônex—Rapport final, Géoproduction Consultants—Département des travaux publics et de l'énergie.
Gervaise, J. (1972). *Études géologiques et géotechniques éffectuées sur le site du synchrotron européen de 300 GeV—CERN/MC/61/Rev*.
Gorin, G., Signer, C., & Amberger, G. (1993). Structural configuration of the western Swiss Molasse Basin as defined by reflection seismic data. *Eclogae Geologicae Helvetiae, 86*, 693–716.
Gorin, G., Morend, D., & Pugin, A. (2003). Bedrock, Quaternary sediment and recent fault activity in central Lake Neuchâtel, as derived from high-resolution reflection seismics. *Eclogae Geologicae Helvetiae*. https://doi.org/10.1007/978-3-0348-7992-7_2
Gottlieb, P., Wilkie, G., Sutherland, D., Suthers, S., Perera, K., Jenkins, B., Spencer, S., Butcher, A., & Rayner, J. (2000). Using quantitative electron microscopy for process mineralogy applications. *J. Miner. Met. Mater. Soc., 52*, 24–25. https://doi.org/10.1007/s11837-000-0126-9
Graf, H. R., & Burkhalter, R. (2016). Quaternary deposits: Concept for a stratigraphic classification and nomenclature—an example from northern Switzerland. *Swiss Journal of Geosciences, 109*, 137–147. https://doi.org/10.1007/s00015-016-0222-7
Gross, D., Sachsenhofer, R. F., Bechtel, A., Gratzer, R., Grundtner, M. L., Linzer, H. G., Misch, D., Pytlak, L., & Scheucher, L. (2018). Petroleum systems in the Austrian sector of the north alpine foreland basin: an overview. *Journal of Petroleum Geology*. https://doi.org/10.1111/jpg.12704
Gusterhuber, J., Hinsch, R., Sachsenhofer, R.F. (2014). Evaluation of hydrocarbon generation and migration in the Molasse fold and thrust belt (Central Eastern Alps, Austria) using structural and thermal basin models. American Association of Petroleum Geologists Bulletin. Doi: https://doi.org/10.1306/06061312206
Haas, M., De Haller, A., Moscariello, A., Scibile, L., Benedikt, M., Gegenhuber, N., Galler, R. (2020a). A mineralogical re-use classification model of molasse rock mass in the Geneva Basin. In: ISRM international symposium—EUROCK2020, June 14–19, 2020, Physical Event Not Held. Trondheim.
Haas, M., Galler, R., Scibile, L., & Benedikt, M. (2020b). Waste or valuable resource – a critical European review on re-using and managing tunnel excavation material. *Resources, Conservation and Recycling, 162*, 105048. https://doi.org/10.1016/j.resconrec.2020.105048
Haas, M., Mongeard, L., Ulrici, L., D'Aloïa, L., Cherrey, A., Galler, R., & Benedikt, M. (2021). Applicability of excavated rock material: A European technical review implying opportunities for future tunnelling projects. *Journal of*

Cleaner Production, 315, 128049. https://doi.org/10.1016/j.jclepro.2021.128049
Haq, B. U. (2014). Cretaceous eustasy revisited. *Global and Planetery Change, 113*, 44–58.
Haq, B. U., Hardenbol, J., & Vail, P. R. (1987). Chronology of Fluctuating Sea Levels Since the Triassic. *Science (80-)., 235*, 1156–1167.
Hasegawa, M., Usui, M., & Gotoh, K. (1993). Geological prognosis ahead of a tunnel face. *Engineering Geology., 35*, 229–235. https://doi.org/10.1016/0013-7952(93)90011-Z
Hefny, M., Zappone, A., de Makhloufi, Y., Haller, A., & Moscariello, A. (2020). A laboratory approach for the calibration of seismic data in the western part of the Swiss Molasse Basin: the case history of well Humilly-2 (France) in the Geneva area. *Swiss J Geosci*, *113*, 11. https://doi.org/10.1186/s00015-020-00364-4.
Herb, R. (1988). Eocaene Paläogeographie und Paläotektonik des Helvetikums. *Eclogae Geologicae Helvetiae, 81*, 611–657.
Hinsch, R. (2013). Laterally varying structure and kinematics of the Molasse fold and thrust belt of the Central Eastern Alps: Implications for exploration. *American Association of Petroleum Geologists Bulletin*. https://doi.org/10.1306/04081312129
Homewood, P., Allen, P.A., Williams, G.D. (1986). Dynamics of the molasse basin of Western Switzerland. Forel. Basins, Wiley Online Books (pp. 199–217). Doi: https://doi.org/10.1002/9781444303810.ch10
Huang, L., Bohne, R. A., Bruland, A., Jakobsen, P. D., & Lohne, J. (2015). Environmental impact of drill and blast tunnelling: life cycle assessment. *Journal of Cleaner Production., 86*, 110–117. https://doi.org/10.1016/j.jclepro.2014.08.083
Ibele, T., 2011. Tectonics of the western Swiss Molasse Basin during Cenozoic times. GeoFocus.
Jaquet, J.-M. (1966). Etude géologique de la région du Reculet. Diplôme thesis, Université de Genève.
Jasmund, K., Lagaly, G. (1993). Tonminerale und Tone—Struktur, Eigenschaften, Anwendung und Einsatz in Industrie und Umwelt. Steinkopff Verlag, Darmstadt. https://doi.org/10.1007/978-3-642-72488-6
Jenny, J., Burri, J.-P., Muralt, R., Pugin, A., Schegg, R., Ungemach, P., Vuataz, F.-D., & Wernli, R. (1995). Le forage géothermique de Thônex (Canton de Genève): Aspects stratigraphiques, tectoniques, diagénétiques, géophysiques et hydrogéologiques. *Eclogae Geologicae Helvetiae, 88*, 365–396.
Kaelin, D. (1997). Litho-und Biostratigraphie der mittel-bis obermiozänen Bois de Raube-Formation (Nordwestschweiz). *Eclogae Geologicae Helvetiae, 90*(1), 97–114.
Kaelin, D., & Kempf, O. (2009). High-resolution stratigraphy from the continental record of the Middle Miocene Northern Alpine Foreland Basin of Switzerland. *Neues Jahrbuch Für Geologie Und Paläontologie - Abhandlungen, 254*, 177–235. https://doi.org/10.1127/0077-7749/2009/0010
Kaelin, D., Rybach, L., Kempter, E. H. K., Kaelin, B., Rybach, L., & Kempter, E. H. K. (1992). Rates of deposition, uplift and erosion in the Swiss Molasse basin, estimated from sonic- and density-logs. *Bulletin Der Vereinigung Schweizerischer Petroleum-Geologen Und-Ingenieure, 58*, 9–22.
Kafkafi, U., Xu, G., Imas, P., Magen, H., Tarchitzky, J., Johnston, A. (2001). Potassium and chloride in crops and soils: the role of potassium chloride fertilizer in crop nutrition. In: International Potash Institute. International Potash Institute, Basel, Switzerland, p. 220.
Karner, G. D., & Watts, A. B. (1983). Gravity anomalies and flexure of the lithosphere at mountain ranges. *Journal of Geophysical Research: Solid Earth, 88*, 10449–10477. https://doi.org/10.1029/JB088iB12p10449
Keller, B. (1989). *Fazies und Stratigraphie der Oberen Meeresmolasse (unteres Miozän) zwischen Napf und Bodensee*. Universität Bern.
Keller, B. (1992). Hydrogeology of the Swiss Molasse Basin: A review of current knowledge and considerations for the future. *Eclogae Geologicae Helvetiae, 85*, 611–651.
Kempf, O., & Matter, A. (1999). Magnetostratigraphy and depositional history of the Upper Freshwater Molasse (OSM) of eastern Switzerland. *Eclogae Geologicae Helvetiae, 92*, 97–103.
Kempf, O., & Pross, J. (2005). The lower marine to lower freshwater Molasse transition in the northern Alpine foreland basin (Oligocene; central Switzerland-south Germany): Age and geodynamic implications. *International Journal of Earth Sciences, 94*, 160–171. https://doi.org/10.1007/s00531-004-0437-0
Kempf, O., Bolliger, T., Kaelin, D., Engesser, B., Matter, A. (1997). New magnetostratigraphic calibration of early to middle Miocene mammal biozones of the North Alpine foreland basin. Me´m Trav EPHE Inst Montpellier (pp. 547–561).
Kissling, D. (1974). L'Oligocène de l'extrémité occidentale du bassin molassique suisse: stratigraphie et aperçu sedimentologique. Université de Genève.
Klinkenberg, L.J. (1941). The permeability of Porous media to liquids and gases. In: API drilling and productions practicesdrilling and productions practices. New York (pp. 200–213).
Kovári, K., Vogelhuber, M. (2014) Empirical basis for the design of tunnel linings in swelling rock containing Anhydrite. In: Proceedings of the World Tunnel Congress 2014—Tunnels for a Better Life. Foz do Iguaçu, Brazil (pp. 1–9).
Kovári, K., Amstad, C., Anagnostou, G. (1987). Tunnelbau in quellfähigem Gebirge.pdf. In: Mitteilungen Der Schweizerischen Gesellschaft Für Boden- Und Felsmechanik, Frühjahrstagung 7. Mai, Biel (pp. 1–8).
Kovári, K., Amberg, F., Ehrbar, H. (2002). Mastering of squeezing rock in the gotthard base. World Tunn (pp 234–238).
Kuhlemann, J. (2000). Post-collisional sediment budget of circum-Alpine basins (Central Europe). *Mem Sci Geol Padova, 52*, 1–91.
Kuhlemann, J., & Kempf, O. (2002). Post-Eocene evolution of the North Alpine Foreland Basin and its response to Alpine tectonics. *Sedimentary Geology, 152*, 45–78. https://doi.org/10.1016/S0037-0738(01)00285-8
Kuhlemann, J., Frisch, W., Székely, B., Dunkl, I., Kázmér, M., & Kazmer, M. (2002). Post-collisional sediment budget history of the Alps: Tectonic versus climatic control. *International Journal of Earth Sciences, 91*, 818–837. https://doi.org/10.1007/s00531-002-0266-y
Lanterno, E., Kunzle, A., Gervaise, J., Bruderlein, J. (1981). Projet LEP—Sondages de reconnaissance: CERN SPS-SU-81-2.
Laubscher, H. (1961). Die Fernschubhypothese derJurafaltung. *Eclogae Geologicae Helvetiae, 54*, 221–281.
Lemcke, K. (1967). Zwölf Jahre Öl- und Gasförderung im süddeutschen Alpenvorland: Ein Überblick. Bull. der Vereinigung Schweiz. *Pet. Und -Ingenieure, 33*, 23–31.
Lemcke, K. (1984). Geologische Vorgänge in den Alpen ab Obereozän im Spiegel vor allem der deutschen Molasse. *Geologische Rundschau, 73*, 371–397. https://doi.org/10.1007/BF01820376
Lemcke, K. (1988). Geologie von Bayern.—I. Teil: Das bayerische Alpenvorland vor der Eiszeit. Stuttgart.
Lemcke, K., Engelhardt, W. V., & Füchtbauer, H. (1953). Geologische und sedimentpetrographische Untersuchungen im Westteil der ungefalteten Molasse des deutschen Alpenvorlandes. *Beih. Geol. Jahrb., 11*, 1–182.
Li, J., Hong, A., Yuan, D., Jiang, Y., Deng, S., Cao, C., & Liu, J. (2020). A new distributed karst-tunnel hydrological model and tunnel hydrological effect simulations. *Journal of Hydrology*. https://doi.org/10.1016/j.jhydrol.2020.125639
Lv, Y., Jiang, Y., Hu, W., Cao, M., & Mao, Y. (2020). A review of the effects of tunnel excavation on the hydrology, ecology, and environment in karst areas: Current status, challenges, and perspectives. *Journal of Hydrology*. https://doi.org/10.1016/j.jhydrol.2020.124891
Madritsch, H., Preusser, F., Fabbri, O., Bichet, V., Schlunegger, F., & Schmid, S. M. (2010). Late Quaternary folding in the Jura Mountains: Evidence from syn-erosional deformation of fluvial meanders. *Terra Nova*. https://doi.org/10.1111/j.1365-3121.2010.00928.x
Makhloufi, Y., Rusillon, E., Brentini, M., Moscariello, A., Meyer, M., & Samankassou, E. (2018). Dolomitization of the Upper Jurassic carbonate rocks in the Geneva Basin, Switzerland and France. *Swiss Journal of Geosciences, 111*, 475–500. https://doi.org/10.1007/s00015-018-0311-x
Mastrangelo, B., & Charollais, J. (2018). Nouvelle conception de la structure du Salève. *Archives Des Sciences, 70*, 43–50.
Matter, A., 1980. Flysch and Molasse of Western and Central Switzerland., in: Homewood, P., Trümpy, R. (Eds.), Geology of Switzerland: A Guide Book. Part B Geological Excursions. Wepf & Co., Basel, pp. 261–293.
Mazurek, M., Hurford, A. J., & Leu, W. (2006). Unravelling the multi-stage burial history of the Swiss Molasse Basin: Integration of apatite fission track, vitrinite reflectance and biomarker isomerisation analysis. *Basin Research, 18*, 27–50. https://doi.org/10.1111/j.1365-2117.2006.00286.x
Meier, L. P., & Kahr, G. (1999). Determination of the cation exchange capacity (CEC) of clay minerals using the complexes of copper(II) ion with triethylenetetramine and tetraethylenepentamine. *Clays and Clay Minerals, 47*, 386–388. https://doi.org/10.1346/CCMN.1999.0470315

Mock, S., & Herwegh, M. (2017). Tectonics of the central Swiss Molasse Basin: Post-Miocene transition to incipient thick-skinned tectonics? *Tectonics, 36*, 1699–1723. https://doi.org/10.1002/2017TC004584

Mock, S., Von Hagke, C., Schlunegger, F., Dunkl, I., & Herwegh, M. (2020). Long-wavelength late-Miocene thrusting in the north Alpine foreland: Implications for late orogenic processes. Solid Earth. https://doi.org/10.5194/se-11-1823-2020

Mosar, J. (1999). Present-day and future tectonic underplating in the western Swiss Alps: Reconciliation of basement/wrench-faulting and decollement folding of the Jura and Molasse basin in the Alpine foreland. *Earth and Planetary Science Letters, 173*, 143–155. https://doi.org/10.1016/S0012-821X(99)00238-1

Moscariello, A. (1996). Quaternary geology of the Geneva Bay: sedimentary record, palaeoclimatic and palaeoenvironmental reconstruction since the Last Glacial Cycle. University of Geneva.

Moscariello, A. (2019). Exploring for geo-energy resources in the Geneva Basin (Western Switzerland): opportunities and challenges. *Swiss Bulletin for Applied Geology., 24*, 105–124.

Moscariello, A. (2021). The Geomorphological Landscapes in the Geneva Basin. In E. Reynard (Ed.), *Landscapes and Landforms of Switzerland. World Geomorphological Landscapes*. Cham: Springer. https://doi.org/10.1007/978-3-030-43203-4_6.

Moscariello, A., Pugin, A., Wildi, W., Beck, C., Chapron, E., De Batist, M., Girardclos, S., Ivy Ochs, S., Rachoud-Schneider, A., Signer, C., & Van Clauwenberghe, T. (1998). Déglaciation würmienne dans des conditions lacustres à la terminaison occidentale du bassin lémanique (Suisse occidentale et France). *Eclogae Geologicae Helvetiae, 91*, 185–201.

Moscariello, A., Gorin, G., Rusillon, E., Charollais, J. (2014) Geology of Western Switzerland and nearby France in a geo-energy perspective—field trip B1 Guide Book. In: 19th international sedimentological congress Geneva, 18–22 August. p. 27.

Moscariello, A., Guglielmetti, L., Omodeo-Salé, S., De Haller, A., Eruteya, O.E., Lo, H.L., Clerc, N., Makloufhi, Y., Do Couto, D., Ferreira De Oliveira, G., Perozzi, L., DeOliveira, F., Hollmuller, P., Quiquerez, L., Nawratil De Bono, C., Martin, F., Meyer, M. (2020). Heat production and storage in Western Switzerland: advances and challenges of intense multidisciplinary geothermal exploration activities, an 8 years progress report. In: Proceedings world geothermal congress 2020, April 26–May 2. Reykjavik.

Neff, H.K. (2005). Der Wasseraufnahmeversuch nach Enslin-Neff in der erd- und grundbautechnischen Praxis. In: 5. Österreichische Geotechniktagung. 21.02. & 22.02.2005, Vienna (p. 27).

Ortner, H., Aichholzer, S., Zerlauth, M., Pilser, R., & Fügenschuh, B. (2015). Geometry, amount, and sequence of thrusting in the Subalpine Molasse of western Austria and southern Germany, European Alps. *Tectonics*. https://doi.org/10.1002/2014TC003550

Oxburgh, E.R. (1981). R. Trümpy geology of Switzerland: A guide-book. Part A: An outline of the geology of Switzerland. Basel and New York (Wepf & Co.), 1980. 104 pp., 46 figs., 1 coloured pl. Price Sfr. 35.00. - Part B: Geological Excursions. Ibid., 230 pp., 204 figs. Pri. Mineral. Mag. 44, 366. Doi: https://doi.org/10.1180/minmag.1981.044.335.28

Paolacci, S. (2012). Seismic facies and structural configuration of the Western Alpine Molasse basin and its substratum (France and Switzerland). Université de Genève.

Pfiffner, O.-A. (1986). Evolution of the North Alpine Foreland Basin in the Central Alps. Forel. Basins, Wiley Online Books. Doi: https://doi.org/10.1002/9781444303810.ch11

Pfiffner, O.-A. (2021). The geology of Switzerland (pp. 7–30). Doi: https://doi.org/10.1007/978-3-030-43203-4_2

Pierdona, L. (2018). Chemical stratigraphy and petrography of the Molasse in the Geneva Basin (Master thesis). Université de Genève.

Pirrie, D., Butcher, A.R., Power, M.R., Gottlieb, P., Miller, G.L. (2004). Rapid quantitative mineral and phase analysis using automated scanning electron microscopy (QemSCAN); potential applications in forensic geoscience. Geol. Soc. London, Spec. Publ. 232, 123 LP – 136. Doi: https://doi.org/10.1144/GSL.SP.2004.232.01.12

Potter, P. E., Maynard, J. B., & Depetris, P. J. (2005). *Mud and Mudstones: Introduction and Overview*. Berlin: Springer.

Rehbock-Sander, M., & Jesel, T. (2018). Fault induced rock bursts and microtremors—Experiences from the Gotthard Base Tunnel. *Tunneling and Underground Space Technology., 81*, 358–366. https://doi.org/10.1016/j.tust.2018.07.003

Reichenbacher, B., Uhlig, U., Kowalke, T., Bassler, B., Matzke-Karasz, R., & Schenk, B. (2004). Biota, palaeoenvironments and biostratigraphy of continental Oligocene deposits from the south German Molasse basin (Penzberg Syncline). *Palaeontol, 47*, 639–677.

Rusillon, E. (2018). Characterisation and rock typing of deep geothermal reservoirs in the Greater Geneva Basin (Switzerland & France). Université de Genève. Doi: https://doi.org/10.13097/archive-ouverte/unige:105286

Sachsenhofer, R.F., Leitner, B., Linzer, H.G., Bechtel, A., Ćorić, S., Gratzer, R., Reischenbacher, D., Soliman, A., 2010. Deposition, erosion and hydrocarbon source potential of the Oligocene Eggerding Formation (Molasse Basin, Austria). Austrian Journal of Earth Science.

Schegg, R. (1993). Thermal maturity and history of sediments in the North Alpine Foreland Basin (Switzerland, France). Publ. du Département Géologie Paléontologie. Université de Genève. Doi: https://doi.org/10.13097/archive-ouverte/unige:110443

Schlunegger, F. (1999). Controls of surface erosion on the evolution of the Alps: Constraints from the stratigraphies of the adjacent foreland basins. *International Journal of Earth Sciences*. https://doi.org/10.1007/s005310050265

Schlunegger, F., & Castelltort, S. (2016). Immediate and delayed signal of slab breakoff in Oligo/Miocene Molasse deposits from the European Alps. *Science and Reports*. https://doi.org/10.1038/srep31010

Schlunegger, F., & Hinderer, M. (2001). Crustal uplift in the Alps: Why the drainage pattern matters. *Terra Nov., 13*, 425–432. https://doi.org/10.1046/j.1365-3121.2001.00374.x

Schlunegger, F., & Kissling, E. (2015). Slab rollback orogeny in the Alps and evolution of the Swiss Molasse basin. *Nature Communications, 6*, 8605. https://doi.org/10.1038/ncomms9605

Schlunegger, F., & Mosar, J. (2011). The last erosional stage of the Molasse Basin and the Alps. *International Journal of Earth Sciences, 100*, 1147–1162. https://doi.org/10.1007/s00531-010-0607-1

Schlunegger, F., Burbank, D., Matter, A., Engesser, B., & Mödden, C. (1996). Magnetostratigraphic calibration of the Oligocence to Middle Miocene (30–15 Ma) mammal biozones and depositional sequences of the Swiss Molasse Basin. *Eclogae Geologicae Helvetiae, 89*, 753–788.

Schlunegger, F., Matter, A., Burbank, D. W., & Klaper, E. M. (1997). Magnetostratigraphic constraints on relationships between evolution of the central Swiss Molasse basin and Alpine orogenic events. *Bulletin Geological Society of America*. https://doi.org/10.1130/0016-7606(1997)109%3c0225:MCORBE%3e2.3.CO;2

Schlunegger, F., Melzer, J., & Tucker, G. (2001). Climate, exposed source-rock lithologies, crustal uplift and surface erosion: A theoretical analysis calibrated with data from the Alps/North Alpine Foreland Basin system. *International Journal of Earth Sciences, 90*, 484–499. https://doi.org/10.1007/s005310100174

Schmid, S. M., Pfiffner, O.-A., Froitzheim, N., Schönborn, G., & Kissling, E. (1996). Geophysical-geological transect and tectonic evolution of the Swiss-Italian Alp. *Tectonics, 15*, 1036–1064. https://doi.org/10.1029/96TC00433

Schön, J. H. (2015). *Physical properties of rocks—fundamentals and principles of petrophysics* (2nd ed.). Elsevier B.V.

Schulz, H. M., Sachsenhofer, R. F., Bechtel, A., Polesny, H., & Wagner, L. (2002). The origin of hydrocarbon source rocks in the Austrian Mollasse Basin (Eocene-Oligocene transition). *Marine and Petroleum Geology, 19*, 683–709. https://doi.org/10.1016/S0264-8172(02)00054-5

Services Industriels de Genève (SIG), 2019. Projet Géothermie 2020—Sondage de Satigny—GEo-1-DAS. Well Rep. GEo-01-DAS.

Sinclair, H. D., & Allen, P. A. (1992). Vertical versus horizontal motions in the Alpine orogenic wedge: Stratigraphic response in the foreland basin. *Basin Research, 4*, 215–232. https://doi.org/10.1111/j.1365-2117.1992.tb00046.x

Sinclair, H. D., Coakley, B. J., Allen, P. A., & Watts, A. B. (1991). Simulation of Foreland Basin Stratigraphy using a diffusion model of mountain belt uplift and erosion: An example from the central Alps, Switzerland. *Tectonics, 10*, 599–620. https://doi.org/10.1029/90TC02507

Sommaruga, A. (1997). *Geology of the Central Jura and the Molasse Basin: New insight into an evaporite-based foreland fold and thrust belt*. Mem. la société Neuchatel. des Sci. Nat. Université de Neuchâtel.

Sommaruga, A. (1999). Décollement tectonics in the Jura foreland fold-and-thrust belt. *Marine and Petroleum Geology*. https://doi.org/10.1016/S0264-8172(98)00068-3

Sommaruga, A. (2011). From the central Jura Mountains to the Molasse Basin (France and Switzerland). *Bulletin Für Angewandte Geologie, 16*, 63–75. https://doi.org/10.5169/seals-327746
Sommaruga, A., Eichenberger, U., Marillier, F. (2012). Seismic Atlas of the Molasse Basin. Beiträge zur Geol. der Schweiz—Geophys. 64 pp. PNR61
Sommaruga, A., Mosar, J., Schori, M., Gruber, M. (2017). The role of the triassic evaporites underneath the North Alpine Foreland. In: Permo-Triassic Salt Provinces of Europe, North Africa and the Atlantic Margins. Doi: https://doi.org/10.1016/b978-0-12-809417-4.00021-5
Spiegel, C., Kuhlemann, J., Dunkl, I., & Frisch, W. (2001). Paleogeography and catchment evolution in a mobile orogenic belt: The Central Alps in Oligo-Miocene times. *Tectonophysics*. https://doi.org/10.1016/S0040-1951(01)00187-1
Stauble, M., & Pfiffner, O.-A. (1991). Processing, interpretation and modeling of seismic reflection data in the Molasse Basin of eastern Switzerland. *Eclogae Geologicae Helvetiae*. https://doi.org/10.5169/seals-166767
Steiner, W. (1993). Swelling rock in tunnels: Rock characterization, effect of horizontal stresses and construction procedures. *International Journal of Rock Mechanics and Mining Sciences, 30*, 361–380. https://doi.org/10.1016/0148-9062(93)91720-4
Strasser, A., Charollais, J., Conrad, M. A., Clavel, B., Pictet, A., & Mastrangelo, B. (2016). The Cretaceous of the Swiss Jura Mountains: An improved lithostratigraphic scheme. *Swiss Journal of Geosciences, 109*, 201–220. https://doi.org/10.1007/s00015-016-0215-6
Strunck, P., & Matter, A. (2002). Depositional evolution of the western Swiss molasse. *Eclogae Geologicae Helvetiae, 95*, 197–222.
Su, M., Liu, Y., Xue, Y., Cheng, K., Ning, Z., Li, G., & Zhang, K. (2021). Detection method of karst features around tunnel construction by multi-resistivity data-fusion pseudo-3D-imaging based on the PCA approach. *Engineering Geology*. https://doi.org/10.1016/j.enggeo.2021.106127
Tanikawa, W., & Shimamoto, T. (2006). Klinkenberg effect for gas permeability and its comparison to water permeability for porous sedimentary rocks. *Hydrology and Earth System Sciences Discussions, 3*, 1315–1338. https://doi.org/10.5194/hessd-3-1315-2006
Thalmann, C. (1996). Beurteilung und Möglichkeiten der Wiederverwertung von Ausbruchmaterial aus dem maschinellen Tunnelvortrieb zu Betonzuschlagstoffen. PhD thesis, Eidgenössische Technische Hochschule (ETH), Zurich.
Thouvenot, F., Frechet, J., Tapponnier, P., Thomas, J. C., Le Brun, B., Menard, G., Lacassin, R., Jenatton, L., Grasso, J. R., Coutant, O., Paul, A., & Hatzfled, D. (1998). The M(L) 5.3 Epagny (French Alps) earthquake of 1996 July 15: A long-awaited event on the Vuache Fault. *Geophysical Journal International, 135*(3), 876–892. https://doi.org/10.1046/j.1365-246X.1998.00662.x
Trümpy, R. (1973). The timing of erogenic events in the Central Alps. In K. A. DeJong & R. Scholten (Eds.), *Gravity and tectonics* (pp. 229–251). Wiley.
Uhlig, U., Reichenbacher, B., & Bassler, B. (2000). Säugetiere, Fisch- Otolithen und Charophyten aus den Unteren Cyrenen-Schichten (Oligozän) der bayerischen Faltenmolasse (Murnauer Mulde). Eclogae geol Helv 93:503–516. *Eclogae Geologicae Helvetiae, 93*, 503–516.
Van der Vegt, P., Janszen, A., & Moscariello, A. (2012). Tunnel valleys: current knowledge and future perspectives. In M. Huuse, J. Redfern, D. P. Le Heron, R. J. Dixon, A. Moscariello, & J. Craig (Eds.), *Glaciogenic reservoirs and hydrocarbon systems* (pp. 75–97). Geological Society Special Publications.
Voiron, J., Haas, M., Amiot, J.-B. (2020). CERN HL-LHC POINT 1, Gestion des matériaux d'excavation potentiellement pollués aux hydrocarbures. AFTES Congr. Paris 2020, Sept. 6–8, 2021.
Voit, K. (2013). Einsatz und Optimierung von Tunnelausbruchmaterial des Brenner Basistunnels, PhD thesis, Application and optimization of tunnel excavation material of the Brenner Base Tunnel. Verlag Guthmann-Peterson.
Voit, K., Zeman, O., Murr, R., Bergmeister, K., & Arnold, R. (2015). Aufbereitung und Wiederverwertung von Tunnelausbruchmaterial beim Brenner Basistunnel. *Beton- Und Stahlbetonbau, 110*, 832–844. https://doi.org/10.1002/best.201500023
Von Hagke, C., Cederbom, C. E., Oncken, O., Stckli, D. F., Rahn, M. K., & Schlunegger, F. (2012). Linking the northern Alps with their foreland: The latest exhumation history resolved by low-temperature thermochronology. *Tectonics*. https://doi.org/10.1029/2011TC003078
Vrakas, A., & Anagnostou, G. (2016). Ground response to tunnel re-profiling under heavily squeezing conditions. *Rock Mechanics and Rock Engineering, 49*, 2753–2762. https://doi.org/10.1007/s00603-016-0931-2
Wanninger-Huber, T. (2019). Experimental investigations for the modelling of anhydritic swelling claystones. *ETH Zurich*. https://doi.org/10.3929/ethz-b-000369625
Wegmüller, S., Amberger, G., & Vernet, J.-P. (1995). La formation de Montfleury près de Genève: Etude palynologique et sédimentologique d'une séquence du Pleistocène moyen. *Eclogae Geologicae Helvetiae, 88*, 595–614. https://doi.org/10.5169/seals-167689
Wehner, H., Hufnagel, H., Kuckelkorn, K., Schoell, M., Teschner, M. (1983). On the genesis of hydrocarbons in the German Alpine foreland.
Wetzel, A., Allenbach, R., & Allia, V. (2003). Reactivated basement structures affecting the sedimentary facies in a tectonically "quiescent" epicontinental basin: An example from NW Switzerland. *Sedimentary Geology*. https://doi.org/10.1016/S0037-0738(02)00230-0
Whitney, D. L., & Evans, B. W. (2010). Abbreviations for names of rock-forming minerals. *American Mineralogist, 95*, 185–187. https://doi.org/10.2138/am.2010.3371
Wildi, W., Corboud, P., Gorin, G., 2017. Guide : géologie et archéologie de Genève Guidebook : geology and archaeology of Geneva. Société Phys. d'histoire Nat. Genève 93.
Willett, S. D., & Schlunegger, F. (2010). The last phase of deposition in the Swiss Molasse Basin: From foredeep to negative-alpha basin. *Basin Research, 22*, 623–639. https://doi.org/10.1111/j.1365-2117.2009.00435.x
Winkler-Hermaden, A. (1958). Geologisches Kräftespiel und Landformung. *GFF*. https://doi.org/10.1080/11035895809447260
Wyllie, M. R. J., Gregory, A. R., & Gardner, L. W. (1956). Elastic wave velocities in heterogeneous and porous media. *Geophysics, 21*, 41–70. https://doi.org/10.1190/1.1438217
Yilmaz, I. (2001). Gypsum/anhydrite: Some engineering problems. *Bulletin of Engineering Geology and the Environment, 60*, 227–230. https://doi.org/10.1007/s100640000071
Zhang, G., Germaine, J. T., Martin, R. T., & Whittle, A. J. (2003). A simple sample-mounting method for random powder X-ray diffraction. *Clays and Clay Minerals, 51*, 218–225. https://doi.org/10.1346/CCMN.2003.0510212
Ziegler, P.A. (1990). Geological Atlas of Western and Central Europe, Geological Atlas of Western and Central Europe. Shell Internationale Petroleum Maatschappij B.V.
Ziegler, H.-J., Isler, A. (2013). Zusammenfassender geologischer Schlussbericht Lötschberg-Basistunnel. Landesgeologie (Bundesamt für Landestopografie swisstopo), Wabern, Switzerland.
Ziegler, P., & Fraefel, M. (2009). Response of drainage systems to Neogene evolution of the Jura fold-thrust belt and Upper Rhine Graben. *Swiss Journal of Geosciences*. https://doi.org/10.1007/s00015-009-1306-4
Zweigel, J., Aigner, T., Luterbacher, H. (1998) Eustatic versus tectonic controls on Alpine foreland basin fill: sequence stratigraphy and subsidence analysis in the SE German Molasse. Geological Society London Special Publications. 134, 299 LP – 323. Doi: https://doi.org/10.1144/GSL.SP.1998.134.01.14

Publisher's Note